


3-23-2017

# Simulation Studies on ECG Vector Dipole Extraction in Liquid Medium

Pratheek Michael

*University of South Florida*, [pratheekmichael@gmail.com](mailto:pratheekmichael@gmail.com)

Follow this and additional works at: <http://scholarcommons.usf.edu/etd>

 Part of the [Biomedical Engineering and Bioengineering Commons](#), and the [Electrical and Computer Engineering Commons](#)

---

## Scholar Commons Citation

Michael, Pratheek, "Simulation Studies on ECG Vector Dipole Extraction in Liquid Medium" (2017). *Graduate Theses and Dissertations*.

<http://scholarcommons.usf.edu/etd/6625>

This Thesis is brought to you for free and open access by the Graduate School at Scholar Commons. It has been accepted for inclusion in Graduate Theses and Dissertations by an authorized administrator of Scholar Commons. For more information, please contact [scholarcommons@usf.edu](mailto:scholarcommons@usf.edu).

Simulation Studies on ECG Vector Dipole Extraction in Liquid Medium

by

Pratheek Michael

A thesis submitted in partial fulfillment  
of the requirements for the degree of  
Master of Science in Electrical Engineering  
Department of Electrical Engineering  
College of Engineering  
University of South Florida

Major Professor: V. K. Jain, Ph.D.  
Richard. D. Gitlin, Sc.D.  
Selçuk Köse, Ph.D.

Date of Approval:  
March 10, 2017

Keywords: Immersion Electrocardiogram, Ellipsoidal Phantoms, Sensing System, COMSOL-  
3D-simulation

Copyright © 2017, Pratheek Michael

## **DEDICATION**

This thesis is dedicated to 7154

## **ACKNOWLEDGEMENTS**

Primarily, I want to thank my major professor, Dr. Vijay K. Jain for his useful comments, remarks, encouragement and assistance which has been continuously provided through the learning process of this master thesis.

Besides my advisor, I would like to thank the thesis committee members: Dr. Richard. D. Gitlin, and Dr. Selçuk Köse for their encouraging and insightful feedback.

I would also like to acknowledge the Department of Electrical Engineering at USF for its support and encouragement.

I would like to thank the DOM, Government of Karnataka, India for their support and financial assistance.

Foremost I would like to thank my parents, especially my mother for her constant support and spiritual insight. They are always encouraging me with their best wishes.

## TABLE OF CONTENTS

LIST OF TABLES	iii
LIST OF FIGURES	iv
ABSTRACT	ix
CHAPTER 1: INTRODUCTION	1
CHAPTER 2: LITERATURE REVIEW AND BACKGROUND	3
2.1. A Note on Heart and ECG	4
2.2. Bioelectric Sources and their Analysis	4
2.2.1. Primary Assumptions	4
2.2.2. Monopole Analysis	5
2.2.3. Dipole Analysis	6
2.2.4. Source Analysis of a Medium with Different Conducting Regions	9
2.2.5. Resultant Dipole Moment	12
2.2.6. Reciprocity Theorem	13
CHAPTER 3: ECG DIPOLE VECTOR EXTRACTION IN LIQUID MEDIUM	14
3.1. Dipole Potential Distribution in 1-Dimension and 2-Dimension	14
3.2. Block Diagram Representation of System Setup	16
3.3. Basis Signal Formulation and Extraction (Section 1)	17
3.4. Simulation of Bathtub-Ellipsoid Model in Water Medium (Section 2)	20
3.4.1. 3-Dimensional Current Dipole	22
3.4.2. Analysis of Single Ellipsoidal Phantom in Water Medium	23
3.4.3. Analysis of Double Ellipsoidal Phantom in Water Medium	27
3.5. Extraction of Sensing Matrix (Section 3)	28
3.5.1. Case Study for Single Ellipsoidal Phantom in Water Medium	30
3.5.2. Case Study for Double Ellipsoidal Phantom in Water Medium	32
3.6. Reconstruction of Basis Signals using Sensing Matrix (Section 4)	34
CHAPTER 4: CONCLUSIONS	36
4.1. Conclusions	36
4.2. Future Work	36
REFERENCES	38
APPENDIX A: BACKGROUND AND LITERATURE REVIEW	44

A.1. Heart and ECG	44
A.1.1. Electrical Activity in the Heart	45
A.1.2. Path for Electrical Conduction in the Heart	46
A.1.3. A Note on Sinoatrial (SA) Node	47
A.1.4. A Note on Vector Representation of the Heart	48
A.1.5. ECG Terminology	49
A.1.6. Ventricular Depolarization for Generation of QRS Complex	52
A.2. Current Dipole Moments in Literature	53
<b>APPENDIX B: DIPOLE EXPERIMENTS IN COMSOL</b>	<b>54</b>
B.1. Model for Verifying Theoretical Concept in COMSOL	54
B.2. Different Types of Dipole Configuration	55
B.2.1. Horizontal Dipole Model	55
B.2.2. Vertical Dipole Model	57
B.2.3. Effect of Medium Size on the Potential Distribution Pattern	58
B.3. Dipole Model Using Small Copper Plates	61
B.4. Potential Distributions for Bathtub Ellipsoid Models	63
B.5. Effect of the Torso Geometry on the Potential Distribution in a Medium	66
B.5.1. Cuboidal Medium with Eccentric Dipoles in Varying Torso Shapes	66
B.5.2. Rectangular Medium with Dipoles in Varying Torso Shapes	67
B.6. COMSOL Procedural Steps in the Context of this Research	69
B.6.1. Research Problem	70
B.7. Proposed Experimental Setup Assembly	79
B.7.1. Structure for Creating 3-Dimensional Dipole (3D-D)	80
<b>APPENDIX C: PRELIMINARY EXPERIMENTS ON 3D-MONOPOLE</b>	<b>81</b>
C.1. System Setup	81
C.1.1. Noise and Bias Effects Reduction	81
C.2. Transferring an fECG or mECG File to BK Function Generator	83
C.3. Singular Excitation of Current Monopoles to Create a Balanced Effect	83

## LIST OF TABLES

Table 3.1.	NRMSE for reconstruction of different type of signals applied to the 3D-CD in COMSOL	34
Table A.1.	Details of intrinsic frequencies of different heart locations	46
Table A.2.	Dipole moments (P) from literature	53
Table B.1.	Effect of monopole size on the potential distribution around the medium	63
Table B.2.	Effect of dipole located at the center inside different torso shapes in a cuboidal medium	67
Table B.3.	Effect of dipole located at an eccentric point inside different torso shapes in a cuboidal medium	67
Table B.4.	Effect of dipole at the center inside different torso shapes in a rectangular medium	68
Table B.5.	Effect of dipole located at an eccentric point inside different torso shapes in a rectangular medium	69

## LIST OF FIGURES

Figure 2.1.	Representation of positive monopole in a spherical medium	5
Figure 2.2.	Representation of a current dipole in 2D inside an infinite conductive medium	6
Figure 2.3.	Representation of current dipole in 3D in an infinite volume homogeneous medium	8
Figure 2.4.	Representation of reciprocity theorem	13
Figure 3.1.	Results for current dipole potential distribution equation plotted for 1D case from theory and verified using COMSOL	15
Figure 3.2.	Current dipole equation plotted for 2D case in MATLAB	15
Figure 3.3.	Block diagram of the overall flow of the research	16
Figure 3.4.	Representing the basis signals for the 3D-CD extracted from mECG	17
Figure 3.5.	Representing the original ECG signals and the reconstructed perfectly overlapping signals for mECG (through SVD approach)	19
Figure 3.6.	Representing basis signals for the 3D-CD extracted from fECG	20
Figure 3.7.	Original fECG and reconstructed fECG signals (through SVD approach)	21
Figure 3.8.	Showing the locations of the electrodes in the bathtub; #1, #2 are on the front surface; #3, #6 are on the side surface; #4, #5 are on the back surface; #7, #8 are on the bottom surface.	21
Figure 3.9.	3D-current dipole	22
Figure 3.10.	Signals recorded from the bathtub sensing electrodes for 3D-CD responding to fECG basis signals	23
Figure 3.11.	Showing a single ellipsoid placed in the bathtub (front face of the bathtub removed for image)	24



Figure 3.12.	Electrode signals recorded from the bathtub for mECG basis signals exciting the 3D-CD inside the single ellipsoid model	24
Figure 3.13.	Non-overlapping synthetic signals exciting the 3D-CD	25
Figure 3.14.	Potential distribution recorded by the sensing probes on the inner surface of the bathtub for non-overlapping synthetic signals exciting the 3D-CD	26
Figure 3.15.	Overlapping synthetic signals exciting the 3D-CD	26
Figure 3.16.	Potential distribution recorded by the sensing probes on the inner surface of the bathtub for overlapping synthetic signals exciting the 3D-CD	27
Figure 3.17.	Showing the two ellipsoids (pregnant subject and the fetus) placed in the bathtub	28
Figure 3.18.	Potential distribution plot observed at the bathtub probes for the activity of two 3D-CD in the two ellipsoidal phantoms	29
Figure 3.19.	Non-overlapping synthetic signals acting as input to 3D-CD in one ellipsoid model and $8 \times 3$ sensing matrix extracted is shown on the right	30
Figure 3.20.	Overlapping synthetic signals acting as inputs to 3D-CD in one ellipsoid model and $8 \times 3$ sensing matrix extracted is shown on the right	31
Figure 3.21.	mECG basis signals acting as input to 3D-CD in one ellipsoid model and $8 \times 3$ sensing matrix extracted is shown on the right	31
Figure 3.22.	fECG basis signals acting as input to 3D-CD in one ellipsoid model and $8 \times 3$ sensing matrix extracted is shown on the right	32
Figure 3.23.	Two different types of synthetic signals exciting the two 3D-CDs inside two ellipsoids and $8 \times 6$ sensing matrix extracted is shown on the right	33
Figure 3.24.	Basis signals from fECG and mIECG (derived from mECG) exciting the two 3D-CDs inside two ellipsoids and $8 \times 6$ sensing matrix extracted is shown on the right	33
Figure 3.25.	Highly overlapping original basis signals and reconstructed basis signals; magnified sections are shown on the right	35
Figure A.1.	Block diagram of systemic circulation	44
Figure A.2.	Representation of the conduction system of the heart	45

Figure A.3.	Representation of the flow of impulse in the heart	47
Figure A.4.	ECG waveform having details of various wave periods	49
Figure A.5.	Standard leads or limb leads	51
Figure A.6.	QRS complex during ventricular depolarization	52
Figure B.1.	Simple rectangular medium for validation of results from COMSOL	54
Figure B.2.	COMSOL analysis of 10 x 1 x 1 cm rectangular medium	55
Figure B.3.	Horizontal dipole configuration	56
Figure B.4.	Potential plot of horizontal dipole simulated in COMSOL	57
Figure B.5.	Vertical dipole configuration	57
Figure B.6.	Potential distribution due to the activity of vertically oriented dipole	58
Figure B.7.	The potential distribution pattern (XZ) noticed for a dipole oriented in X-direction (horizontally) along the length of the medium (where $L > B > H$ )	59
Figure B.8.	The potential distribution pattern (XY) noticed for a dipole oriented in X-direction (horizontally) along the length of the medium (where $L > B > H$ )	60
Figure B.9.	The potential distribution pattern (XY) noticed for a dipole oriented in Z-direction (vertically) along the height of the medium (where $H < B < L$ )	60
Figure B.10.	The potential distribution pattern (XZ) noticed for a dipole oriented in Z-direction (vertically) along the height of the medium (where $H < B < L$ )	61
Figure B.11.	Dipole created using tiny copper plates	62
Figure B.12.	2D potential map of dipole created using copper plates	62
Figure B.13.	Potential distributions caused by the activity of 3D-CD in a bathtub containing tap water; XY view	63
Figure B.14.	Potential distributions caused by the activity 3D-CD in a bathtub containing tap water; XZ view	64
Figure B.15.	Potential distribution caused by the activity of 3D-CD inside single ellipsoidal phantom placed in a bathtub containing water; XY view	64

Figure B.16.	Potential distribution caused by the activity of 3D-CD inside single ellipsoidal phantom placed in a bathtub containing water; XZ view	65
Figure B.17.	Potential distribution caused by two 3D-CDs inside a double ellipsoidal phantom laying in the bathtub filled with tap water; XY view	65
Figure B.18.	Potential distribution caused by two 3D-CDs inside a double ellipsoidal phantom laying in the bathtub filled with tap water; XZ view	66
Figure B.19.	Cuboidal medium containing different torso shapes	66
Figure B.20.	Rectangular medium with dipole at different locations inside different torso shapes	68
Figure B.21.	Selection of dimension of workspace	69
Figure B.22.	Selection of the appropriate physics	69
Figure B.23.	Selection of study type	70
Figure B.24.	Icon for starting a new simulation	70
Figure B.25.	Workspace selection	71
Figure B.26.	Selection of physics for solving the problem	71
Figure B.27.	Selection of study type	71
Figure B.28.	Option for selection of an ellipsoid	71
Figure B.29.	Ellipsoid dimensions on the left and the model built is shown on the right	72
Figure B.30.	Details on explicitly selecting the ellipsoid	72
Figure B.31.	Rotation setting and the built model	73
Figure B.32.	Representation of double ellipsoids	73
Figure B.33.	Inputs for the eccentric points in the medium	74
Figure B.34.	Representation of double ellipsoidal phantom with eccentrically located points	74
Figure B.35.	Details of creating a trapezoidal medium	75

Figure B.36.	Details depicting how to rotate the model built	75
Figure B.37.	Bathtub ellipsoid model	76
Figure B.38.	Options for selection of materials	76
Figure B.39.	Importing a basis signal from external file	77
Figure B.40.	Interpolation	77
Figure B.41.	Option to create a point electric dipole	77
Figure B.42.	Specification of the two vector dipoles located eccentrically inside each ellipsoid	78
Figure B.43.	Details on adding probes to the medium	78
Figure B.44.	Details to choose the type of study	79
Figure B.45.	Assembly of the ellipsoid and 3D-CD in the plastic container model	79
Figure B.46.	Mounting structure for the 3D-D built using 6 copper plates in orthogonal directions	80
Figure C.1.	System setup	82
Figure C.2.	Block diagram of fECG or mECG file transfer from PC to BK	83
Figure C.3.	Experiment of 3D-M using singular excitations	85
Figure C.4.	Inputs to the 3-axis monopoles	86
Figure C.5.	Potential distribution recorded at the probes with mean subtracted when X-axis monopole is active	86
Figure C.6.	Potential distribution recorded at the probes with mean subtracted when Y-axis monopole is active	87
Figure C.7.	Potential distribution recorded at the probes with mean subtracted when Z-axis monopole is active	87

## ABSTRACT

To circumvent some inherent problems in the conventional ECG, this research reinvestigates an ‘unassisted’ approach which enables ECG measurement without the placement of leads on the body. Employed in this research is a widely accepted assumption that the electrical activity of the heart may be represented, largely, by a 3-D time-varying current dipole (3D-CD). From the PhysioBank database, mECG and fECG data were obtained, and Singular Value Decomposition (SVD) was performed to estimate the time varying Vector ECG dipole. To determine the sensing matrix responsible for transforming the activity of the 3D-CD into the potential distribution on the surface of the medium, the ECG vector dipole signals are used to excite a 3D-CD in water medium of specific shape-containing-ellipsoid model(s) in COMSOL tool. The sensing matrix thereby estimated is then utilized to reconstruct the 3D-CD signals from the signals measured by the probes on the surface of the medium. Fairly low NRMSEs (Normalized Root-Mean-Squared Errors) are attained. The approach is also successfully extended to the case of two ellipsoids, one inside the other, representing a pregnant female subject. Low NRMSEs (Normalized Root-Mean-Squared Errors) are again observed.

## CHAPTER 1: INTRODUCTION

ECG measurements record the projections of the electrical activity of the heart vs. time. Bioelectric sources can emulate that activity. Therefore, this research focuses on a technique to extract the signals of origin based upon the recorded ECG waveforms which can represent the activity of the heart. Researchers profess that the electrical properties of the heart can reflect a current dipole. Therefore, the concept of SVD decomposition was applied to extract these basis signals (source signals) and excite a COMSOL model of a 3-dimensional current dipole (3D-CD) which best represents the electrical activity of the bioelectric source present in the heart. The aim is to make this research helpful and get proper applications. Therefore, we reinvestigate ECG measurements using liquid media and incorporate the research of ECG vector dipole to extract a “sensing matrix” which is responsible for transforming the electrical activity of the vector dipole into potential distribution in the surrounding media. The adoption of telehealth monitoring has been on the rise, where individuals can monitor their body vitals at the comfort of their home and a physician telephonically can interpret the results. This research can be used to test ECG telehealth monitoring systems to improve their accuracy and precision.

Chapter 2 gives an overview of the bioelectric sources and their analysis from literature, and some insight on sources embedded inside inhomogeneous media which can be quantified to just two regions to provide more focus on this research. Chapter 3, explains the main idea of using the source signals to extract sensing matrix using 3D-CD inside a liquid medium to facilitate the process. The thesis further stresses on the fact that with the help of the potential distribution on the

outer surface of the medium and the sensing matrix, reconstruction of the original basis signals and the original ECG signals are possible. Chapter 4 focuses on relevant conclusions which can be inferred from this research and the future research possibilities built on the research problem presented in this thesis.

Related useful information is provided in the appendices. Appendix A provides background and literature review about the Heart and ECG-related terminologies. Appendices B.1 to B.5 covers most significant results from the COMSOL experiments. A handy exposition on the procedural steps is provided in Appendix B.6. Appendix C embarks on the topic of 3D monopoles. The analysis of a pair of monopole by unequal excitation and its result is detailed in this section.

## CHAPTER 2: LITERATURE REVIEW AND BACKGROUND

Recent ECG research has encompassed areas ranging from cardiac activation locations [1], electrode sensitivity variations [2], conductive fabric for sensing bio-potentials [3], Noise reduction techniques [4], wearable electronics [5], sleep apnea detection [6], Carbon black PDMS electrodes [7], Ubiquitous-ECG [8], non-contact electrodes [9]-[10], arrhythmia detections, and biometric recognition through ECG [11]. To understand the nature of cardiovascular health one requires a correct approach for measuring the bioelectrical and bio-magnetic data through invasive and non-invasive techniques.

These methods record the electrical activity of the heart and require human subjects for precision and accuracy of experimental results. An alternative is the inverse problem of ECG, which is adopted by many researchers sharing a similar view to model a bioelectric source. These include heart surface activation imaging [12]-[14], a moving dipole model [15], epicardial potential mapping [16]. Heart models are being used to solve the inverse problems in 3D which includes computational [17]-[18] and experimental results [19]. These are aided by heart models [17], [20], [21]. Telehealth monitoring involves the technological assistance in monitoring the patients, while the patient conducts the measurements themselves under no supervision [22]. These remote monitoring systems are seeing an increase in adoption rates as the reduced costs favor the users [23], [24]. However, the telehealth monitoring systems suffer from the decreased signal quality due to some factors ranging from non-expert users to single lead measurements which result in a distorted signal amplitude with noise infested waveforms.



## **2.1. A Note on Heart and ECG**

The heart has specialized pacemaker cells which generate electrical impulses which result in the pumping of blood for systemic circulation. These impulses are responsible for the body surface potential distribution. Frank [30] suggested the use of Limb leads for recording the ECG potentials. More on the Heart and ECG is detailed in Appendix A.

For almost five decades there have been researchers who have tried to model the electrical activity of the heart with the help of bioelectric sources. The most accepted and professed bioelectric source is the current dipole. In this section, emphasis is given to topics like bioelectric current monopole, dipole and its use in the present research.

## **2.2. Bioelectric Sources and their Analysis**

### **2.2.1. Primary Assumptions**

For this research, we take into account a list of assumptions taken from the literature for supporting our results and stating our theory. The assumptions are as follows,

- 1) Helmholtz [31] introduced the reciprocity theorem. He pointed out that the principle of superposition could be the best bet to be applied to any bioelectric problem. The principle states that “The electric field arising from several sources is the sum of the fields that would be present for each source acting separately.”
- 2) Schwan and Kay [32] suggested that the current density in regions beyond the site of an action potential is linearly related to the Electric field intensity.
- 3) Schwan and Kay [33] suggested that the capacitive component of the impedance is negligible at frequencies below several kiloHertz, these sub kiloHertz frequencies are of interest in ECG.
- 4) Geselowitz [34], has suggested that the electromagnetic wave effect can be neglected.

- 5) The pulse rise times of the order of a microsecond suffer only minor distortion through the thorax

### 2.2.2. Monopole Analysis

When a point current source is present inside a uniform volume conductor, it will give rise to voltage gradients around it in the medium [35]. The monopole is considered to be point source whose effect can be analyzed as follows,

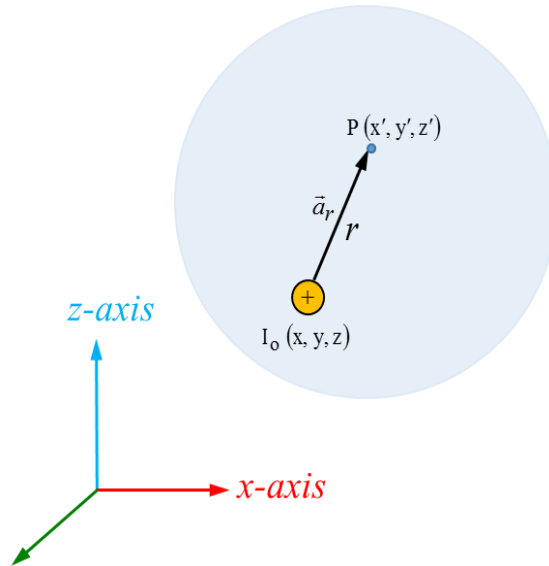


Figure 2.1: Representation of a positive monopole in a spherical medium

Consider that a point source of electric current is embedded in a uniform conducting medium of conductivity  $\sigma$  Siemens/m. Let the monopole be at the position  $(x, y, z)$  the currents are radial as the medium assumed is uniform. The current density for the monopole source is

$$\vec{J} = \frac{I_0}{4\pi r^2} \vec{a}_r \quad (2.1)$$

$$r^2 = (x - x')^2 + (y - y')^2 + (z - z')^2 \quad (2.2)$$

where  $J$  is the current density, and  $a_r$  is the unit vector which is directed radially outward. The potential at any point inside the medium is  $\Phi_{Pm}$  given by

$$\phi_{\text{Pm}} = \frac{I_o}{4\pi\sigma r} \quad (2.3)$$

Using equation (2.3) the potential at any point within the medium containing the monopole can be evaluated. Mathematically a monopole can be considered and modeled as a singularity. It is very rare that natural sources of bioelectricity involve monopoles (because of the need to conserve charges) since sources arising from sensitive tissues consist of differentially spaced source and sink combinations [35] Therefore, it is considered in this research that the dipole is the primary bioelectric source.

### 2.2.3. Dipole Analysis

A dipole can be considered as a pair of current monopoles of equal magnitude but opposite polarity separated by a small distance in an infinite medium of conductivity  $\sigma$  Siemens/m. The electric potential due to the dipole can be derived using (2.3), and it is given by

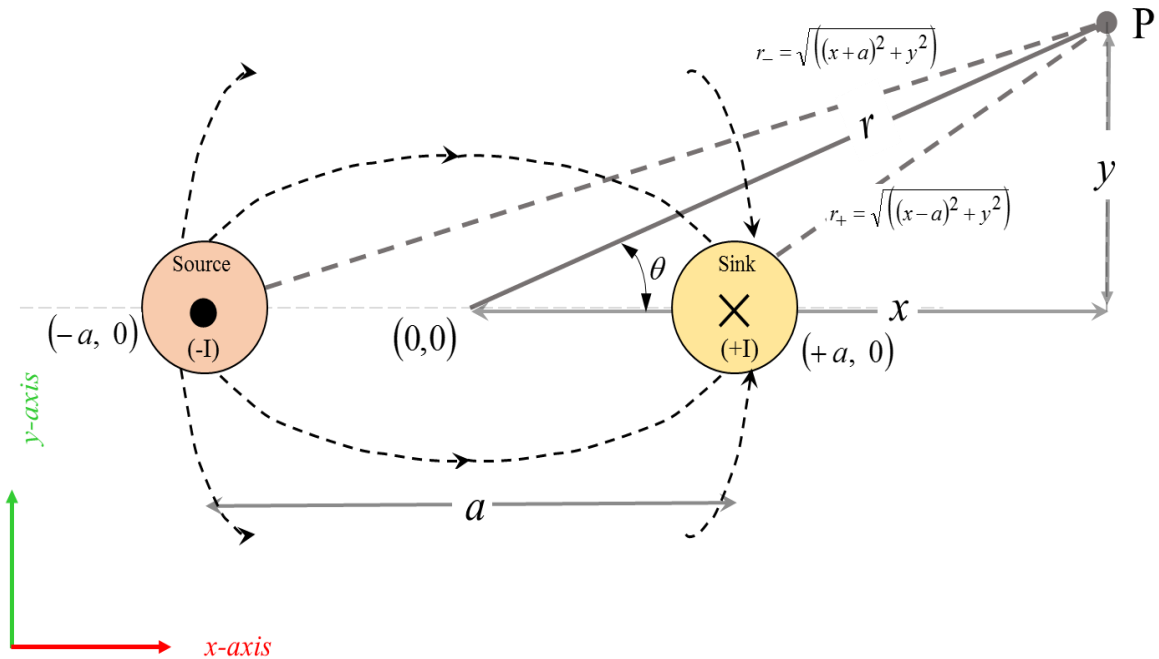


Figure 2.2: Representation of current dipole in 2D inside an infinite conductive medium

$$\frac{\phi_{Pd}}{d} = \frac{\partial}{\partial d} \left( \frac{I_o}{4\pi\sigma r} \right) \quad (2.4a)$$

$$\phi_{Pd} = \frac{I_o}{4\pi\sigma} \frac{\partial \left( \frac{1}{r} \right)}{\partial d} * d \quad (2.4b)$$

wkt,

$$\frac{\partial}{\partial d} \left( \frac{1}{r} \right) = \nabla \left( \frac{1}{r} \right) \cdot \vec{a}_d \quad (2.5)$$

$$\phi_{Pd} = \frac{I_o}{4\pi\sigma} \nabla \left( \frac{1}{r} \right) \cdot \vec{a}_d d \quad (2.6a)$$

$$\phi_{Pd} = \frac{1}{4\pi\sigma} \nabla \left( \frac{1}{r} \right) \cdot \vec{p} \quad (2.6b)$$

wkt,

$$\nabla \left( \frac{1}{r} \right) = \frac{\vec{a}_r}{r^2} \quad (2.6c)$$

$$\phi_{Pd} = \frac{1}{4\pi\sigma} \frac{p \cos \theta}{r^2} \quad \text{for } \vec{r} \gg d \quad (2.7)$$

where,  $|\vec{p}| = |I_o * d|$

To find the potential distribution in between the two monopoles or at distances less than the separation distance between the dipoles we use,

$$\phi_{Pd} = \frac{I}{4\pi\sigma} \left( \frac{1}{r_+} - \frac{1}{r_-} \right) \quad \text{for } \vec{r} \ll d \quad (2.8)$$

where 'p' is the dipole moment vector, r, r+, r- are the vectors from (a) the dipole center, (b) the source and (c) the sink,  $\theta$  is the angle between the vectors p and r as shown in Fig.2.2.

The single dipole model of the heart's electrical activity can be simplified and explained based on a dipole shown in Fig. 2.3 in an infinite volume homogeneous conductor. Then the potential generated at any location inside the volume conductor of conductivity  $\sigma$  Siemens per meter is given by

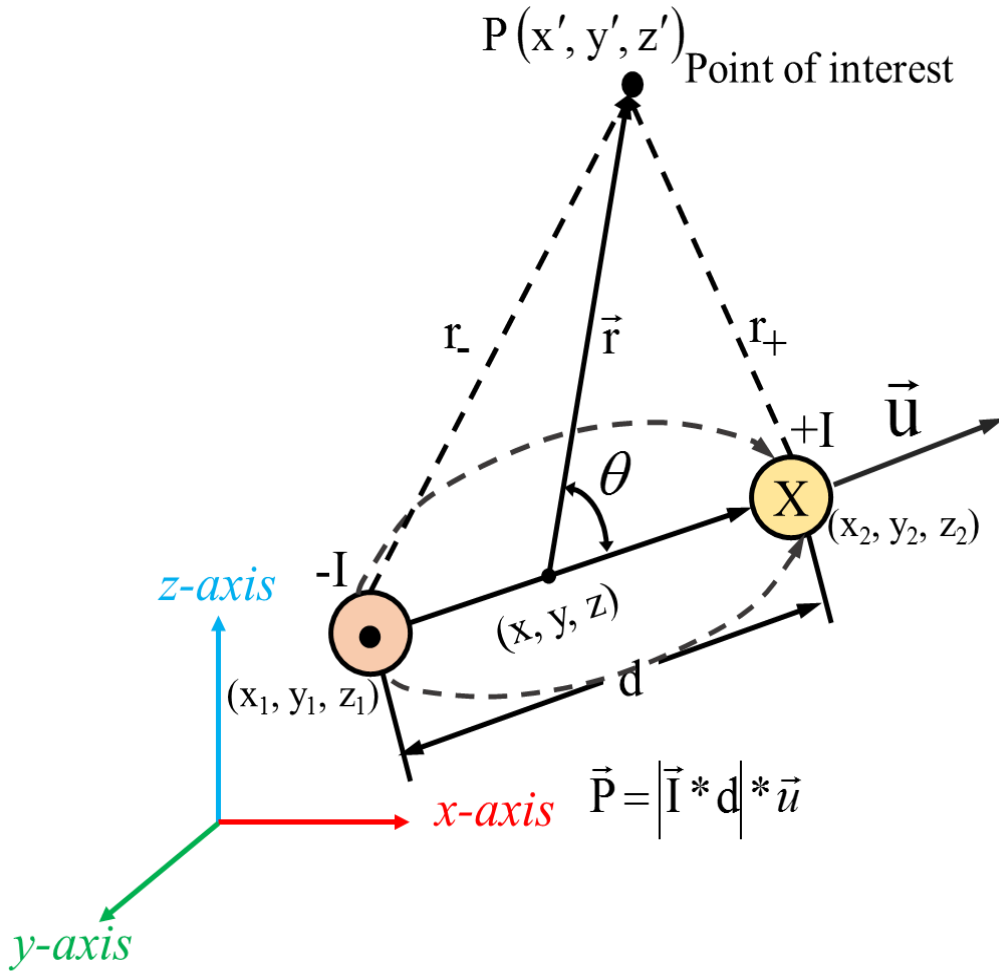


Figure 2.3: Representation of current dipole in 3D in an infinite volume homogeneous medium

$$\begin{aligned}
 V_{\vec{r}}(t) &= \frac{\vec{p}(t) \cdot \vec{r}}{4\pi \sigma |\vec{r}|^3} \\
 &= \frac{1}{4\pi \sigma} \left[ \frac{r_x}{|\vec{r}|^3} p_x(t) + \frac{r_y}{|\vec{r}|^3} p_y(t) + \frac{r_z}{|\vec{r}|^3} p_z(t) \right] \quad (2.9)
 \end{aligned}$$

$$= \frac{1}{b 4\pi\sigma} \left[ r_x p_x(t) + r_y p_y(t) + r_z p_z(t) \right] \quad (2.10)$$

where,

$$b = |\vec{r}|^3$$

$$\vec{r}^2 = (x - x')^2 + (y - y')^2 + (z - z')^2$$

#### 2.2.4. Source Analysis of a Medium with Different Conducting Regions

The discussion in this subsection attempts to prove a simpler method for the analysis of current dipole inside a medium separated by two boundaries [36]. Consider a current dipole inside a medium of conductivity  $\sigma$  that can be represented by an impressed current density, by a current dipole moment per unit volume. The medium including a source can be written as

$$J = \sigma E + J^i \quad (2.11)$$

Using assumption no.4, it can be said that Electric field can be obtained by the gradient of the electric scalar potential,  $V$ .

$$E = -\nabla V \quad (2.12)$$

Using assumption no.3, it is stated that as sources vary, charges quickly gets redistributed on the boundaries without any delay.

$$\nabla \cdot J = 0 \quad (2.13)$$

Using (2.13), equation (2.11) can be modified as,

$$\nabla \cdot J^i = -\nabla \cdot \sigma E \quad (2.14a)$$

$$\nabla \cdot \sigma \nabla V = \nabla \cdot J^i \quad (2.14b)$$

Consider a surface  $S_j$  is separating regions of conductivity  $\sigma'$  and  $\sigma''$  and let  $dS_j$  be the differential element of area of this surface. Considering that  $dS_j$  is directed from primed to double primed region. The currents must be continuous across each boundary, therefore,

$$\sigma' \nabla V' dS_j = \sigma'' \nabla V'' dS_j \quad (2.15)$$

The potential across the boundary has to be continuous as well,

$$V'(S_j) = V''(S_j) \quad (2.16)$$

The solution to the source activity at the boundary of the second layer is given by using greens theorem on an element  $dv$  in a homogeneous region,  $v$ , with two functions  $\psi$  and  $\Phi$ , well behaved in each region,

$$\sum_j \int_{S_j} [\sigma' (\psi' \nabla \phi' - \phi' \nabla \psi') - \sigma'' (\psi'' \nabla \phi'' - \phi'' \nabla \psi'')] dS_j = \sum_v \int_v [\psi \nabla \cdot \sigma \nabla \phi - \phi \nabla \cdot \sigma \nabla \psi] dv \quad (2.17)$$

Using the boundary conditions (2.15) and (2.16) with the knowledge of the impressed current density one can find the potential on the boundary of the outer region. By appropriately identifying  $\psi$  and  $\Phi$  in the region. Choosing  $\psi=1/r$  and  $\Phi=V$  and derive the equation for the potential at the outer surface of a region

$$4\pi\sigma V = \int_v J^i \cdot \nabla \left( \frac{1}{r} \right) dv - \sum_j \int_{S_j} V (\sigma' - \sigma'') \nabla \left( \frac{1}{r} \right) \cdot dS_j - \int_{s_o} V \sigma \nabla \left( \frac{1}{r} \right) dS_o \quad (2.18)$$

The term in the tail end is separated and written as the outer surface after the double primed region has zero conductivity, and the summation only applies across the internal surface discontinuities. The inverse of the above-said problem is stated as “Knowing the potential distribution on the outer surface of a region the source activity can be evaluated” using (2.18).

By reapplying greens theorem, a relationship can be established between the surface measurements and the source distribution of an equivalent generator. Using equation (2.17) and letting  $\nabla^2 \psi = 0$  where  $\psi$  and its first derivatives are continuous everywhere in the volume conductor.

The result in (2.18) can be changed to

$$\int_v J^i \cdot \nabla \psi dv = \sum_j \int_{S_j} V(\sigma' - \sigma'') \nabla \psi \cdot dS_j + \int_{S_o} V \sigma \nabla \psi dS_o \quad (2.19)$$

If P is a fictitious volume distribution of sources in a homogeneous conductor of conductivity  $\sigma_o$  chosen such that potential on the Surface  $S_o$  remains unchanged then,

$$\int_{S_o} V \sigma_o \nabla \psi dS_o = \int P \cdot \nabla \psi dv \quad (2.20)$$

The above equation can reflect this change as follows,

$$\int_{S_o} V \sigma_o \nabla \psi dS_o = \int P \cdot \nabla \psi dv = \int_v J^i \cdot \nabla \psi dv - \sum_j \int_{S_j} V(\sigma' - \sigma'') \nabla \psi dS_j \quad (2.21)$$

To evaluate the integral on the left of (2.21), the knowledge of the potential across the outer surface boundary of the region is required. The multipole expansion [37] gives a canonical description of P in terms of singularities at a single point.

The various terms can be obtained using (2.22)

$$\psi_{nm} = (2 - \delta_m^o) \frac{(n-m)!}{(n+m)!} r^n P_n^m(\cos\theta) e^{im\phi} \quad (2.22)$$

Using the spherical coordinate system  $r, \Theta, \Phi$  are the coordinates of a point in space relative to origin at the location of the multipoles, P is the associated Legendre polynomial, and  $\delta$  is kronecker delta which is unity for  $m=0$  and zero otherwise, both  $n$  and  $m$  are nonnegative integers, and  $m$  is less than or equal to  $n$ . Note that  $\nabla^2 \psi_{nm} = 0$ . The multipole components,  $a_{nm}$  and  $b_{nm}$  are given by (2.23). This equation can be expanded using the term (2.21)

$$a_{nm} + ib_{nm} = \int_s P \cdot \nabla \psi_{nm} dv \quad (2.23)$$

$$a_{nm} + ib_{nm} = \int_{S_o} \sigma_o V \nabla \psi_{nm} dS_o = \int_v J^i \cdot \nabla \psi_{nm} dv - \sum_j \int_{S_j} V(\sigma' - \sigma'') \nabla \psi_{nm} dS_j \quad (2.24)$$



Thus one can say the multipole components can be evaluated from the knowledge of the surface potential distribution and can be related to the actual source distribution.

When  $n=1$ , dipole term is prominent for which

$$\psi_{10} = r \cos \theta = z \quad (2.25a)$$

$$\psi_{11} = r \sin \theta e^{im\phi} = x + iy \quad (2.25b)$$

If the dipole moment,  $p$  is defined as,

$$p = ia_{11} + jb_{11} + ka_{10} \quad (2.26)$$

then

$$p = \int_{s_o} \sigma_o V dS_o = \int_v J^i dv - \sum_j \int_{S_j} V(\sigma' - \sigma'') dS_j = \int P dv \quad (2.27)$$

Thus with the knowledge of potential distribution on the outer potential distribution, the information of the source activity of the source inside any inhomogeneous region of different conductivity can be known.

### 2.2.5. Resultant Dipole Moment

D. Gabor et al. [38] assert that the potential mapping could be recorded from a single dipole source located in a non-specified geometry conductor with small error compared to mapping the actual potential distribution in a human torso. If  $P$  represents the dipole moment,  $\sigma$  is the conductivity of the volume conductor containing sources and  $V$  accounts for the Potential on the body of the volume conductor, then the resultant moment is given by

$$P = \sigma \int_s V dS \quad (2.28)$$

The theory was verified in electrolytic tank model made in the shape of the human thorax. In 2D, the model was based on a full-size cross section of the human thorax; consideration was taken of the different resistivity. A dipole was introduced near the heart region of this model and

the orientation of the heart vector which was found from practical experimentation and known calculated values the direction of the dipole calculated was within 1°, and the calculated locations were correct within 0.5 cm. The magnitude of the current dipole from literature survey is tabulated and given in the Appendix A.2 these results are the dipole moments in human subjects. In this research, a dipole moment of 10 mA-cm will be employed for simulation models.

### 2.2.6. Reciprocity Theorem

Herman Von Helmholtz [31] introduced reciprocity theorem in the late 1800's, and it acts as a common property for all linear systems. The reciprocity theorem states that a current entering and current sink of equal magnitude leaving a volume conductor at two separate locations will give rise to fields everywhere and in particular to a potential difference measured between two locations on the surface of the conductor. The inverse of this experiment being that a current injected on the surface produces a potential difference at the locations inside the volume conductor is true as well. A summary of the reciprocity theorem can be as seen in Fig. 2.4.

$$-V_{34} * I' = V'_{12} * I \quad (2.29)$$

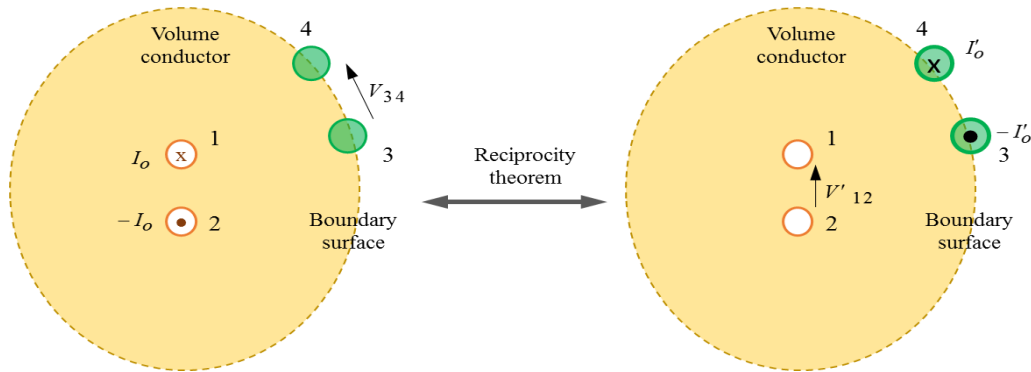


Figure 2.4: Representation of reciprocity theorem

## CHAPTER 3: ECG DIPOLE VECTOR EXTRACTION IN LIQUID MEDIUM

To interlink the topics of research on bioelectric sources, ECG measurements, and the present research described in this thesis, many software were used for simulating realistic 3D models. This chapter details the research idea of the thesis through COMSOL models, and the results are analyzed using MATLAB. Although all of the simulations performed during the investigation cannot be included here in detail, a few relevant results and their influence on this research are detailed in Appendix B.

### 3.1. Dipole Potential Distribution in 1-Dimension and 2-Dimension

This subsection provides results of the potential distribution of a current dipole with respect to a realistic model of current dipole set up in COMSOL and its theoretical analysis. For convenience, the dipole potential distribution equation given in chapter 2 is repeated

$$\phi_{\text{Pd}} = \frac{1}{4\pi\sigma} \frac{p \cos\theta}{r^2} \quad \text{for } \vec{r} \gg d \quad (2.7)$$

$$\phi_{\text{Pd}} = \frac{I}{4\pi\sigma} \left( \frac{1}{r_+} - \frac{1}{r_-} \right) \quad \text{for } \vec{r} \ll d \quad (2.8)$$

For 1D and 2D cases (2.7) and (2.8) were used to theoretically evaluate the potential distribution of a current dipole. A COMSOL model of a current dipole was created using 0.025 x 0.025 cm copper plates where dipole separation was maintained to be 2 mm in a homogeneous medium of conductivity 0.05 S/m and dimensions 10 x 5 x 5 cm. The distributions were mapped at distances incrementing on one axis only as shown in Fig. 3.1.

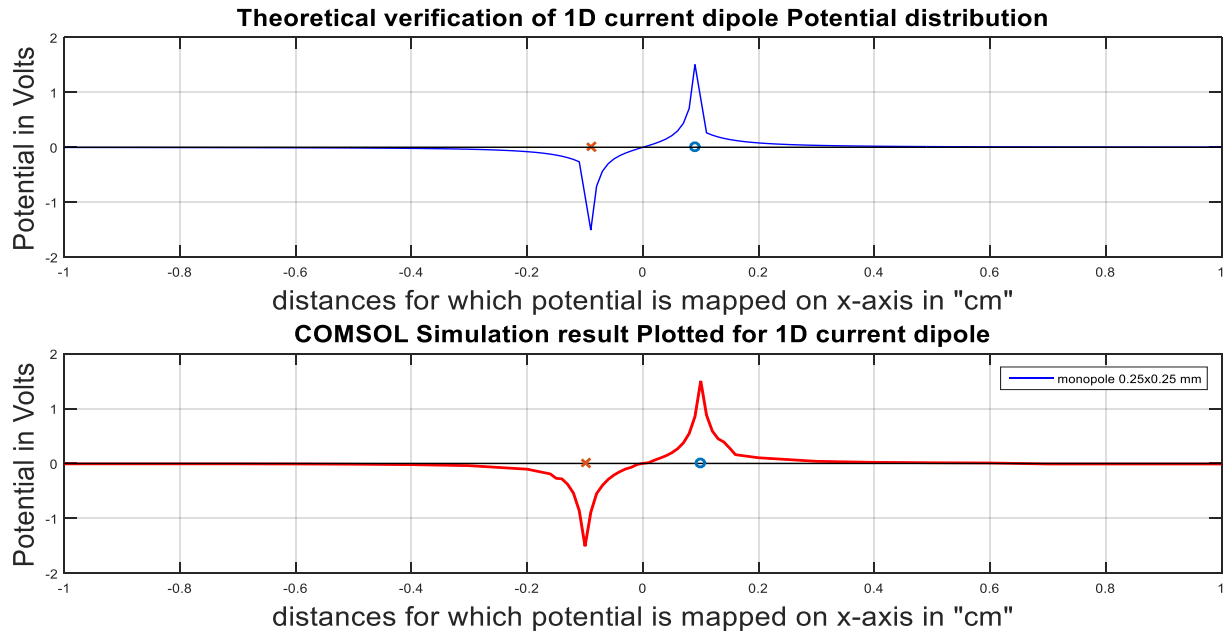


Figure 3.1: Results for current dipole potential distribution equation plotted for 1D case from theory and verified using COMSOL

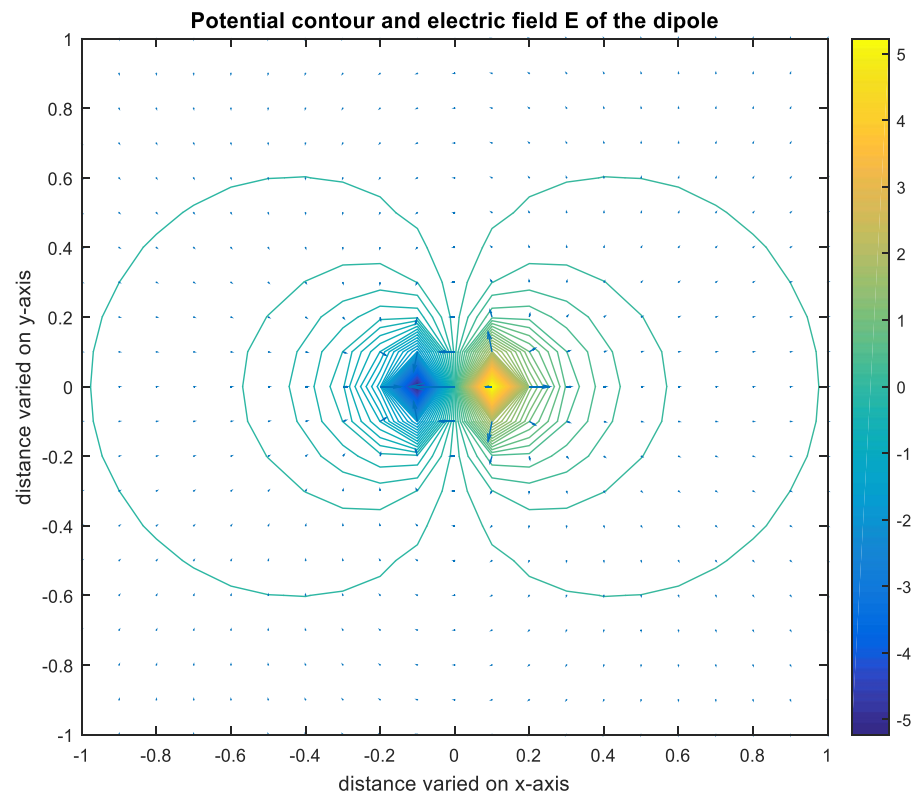


Figure 3.2: Current dipole equation plotted for 2D case in MATLAB

The peaks of the resulting potential distributions of current dipole in both the theoretical analysis and COMSOL based simulation are almost the same as shown in Fig. 3.1. Using the equation for potential distribution of a current dipole, the potential distribution of any point varying with respect to the dipole on both x and y-axis can be found, and it is plotted as shown in Fig. 3.2.

### 3.2. Block Diagram Representation of System Setup

A representation of the overall process which is detailed in the succeeding pages of this chapter is represented by a block diagram in Fig. 3.3

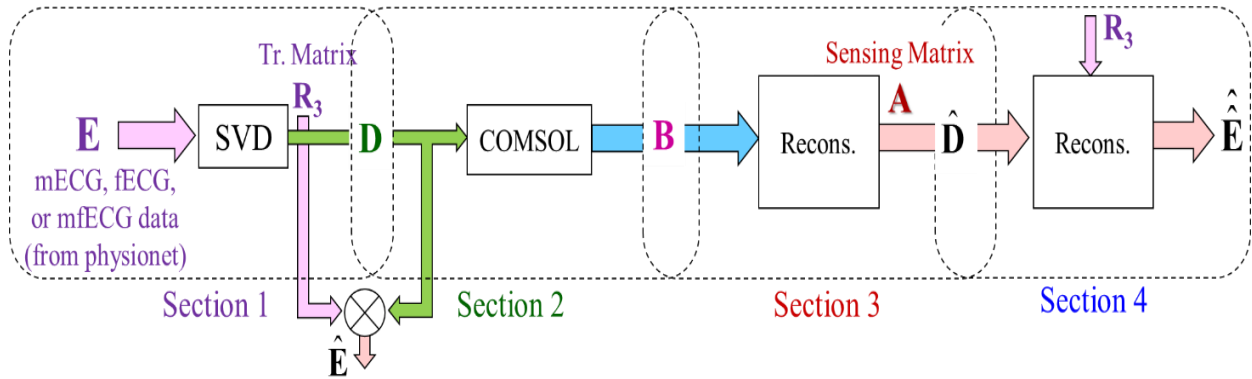


Figure 3.3: Block diagram of the overall flow of the research

First, upon publicly available ECG data from physionet [39], Singular Value Decomposition is applied to find the dominant singular values and, correspondingly, the 3-D time-varying Current Dipole (3D-CD) signals (compacted into a matrix  $D$ ), which are responsible for the potential distribution inside a medium. These signals excite a COMSOL model of 3D-CD located inside a box shaped medium-ellipsoid model. The simulation outputs (compacted into a matrix  $B$ ) are in turn used to extract the sensing matrix ( $A$ ) which is used to reconstruct the 3D-CD signals which can, in turn, be used to reconstruct the basis signals ( $\hat{D}$ ) and the original ECG data ( $\hat{E}$ ). This block diagram of Fig. 3.3 will be explained in detail in the following subsections.

### 3.3. Basis Signal Formulation and Extraction (Section 1)

PhysioBank [39] is an extensive collection of digital recordings of physiological signals and related data which can be used for biomedical research. That database includes multi-parameter cardiopulmonary, neural, and other biomedical signals from healthy subjects and diseased subjects with chronic disorders. Our main focus was on the ECG database, as it contains data recorded and artificially created for healthy, pregnant, and diseased subjects. This research utilizes the mECG and fECG signals of 10 seconds record length from the Synthetic database in PhysioBank.

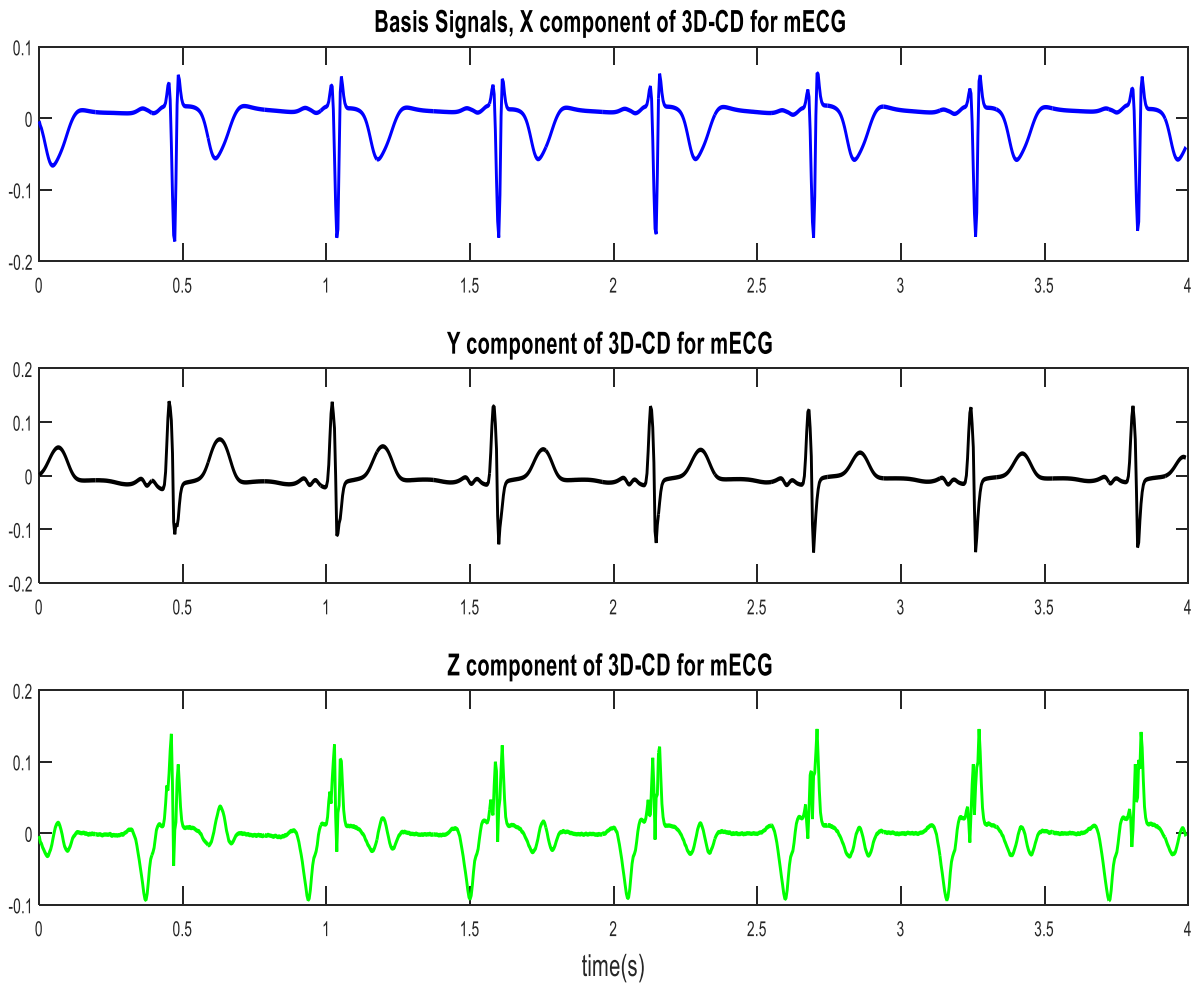


Figure 3.4: Representing the basis signals for the 3D-CD extracted from mECG

As every cardiac researcher has professed the bioelectric activity of the heart can be represented by a current dipole, this research mainly focuses on the concept of finding the Vector characteristics of the 3D-CD and will aid us in the reinvestigation of Bathtub approach for ECG recording [29]. The Singular Value Decomposition (SVD) approach is used to extract the dominant three singular values which we term as the basis signals from the ECG, fECG (fetal ECG), and mECG (mothers ECG) all from Physionet [39]. The approach for the extraction of singular values are as follows, If that data is of dimension ‘ $m \times N$ ’ where  $N \gg m$ , then through SVD,

$$[E]_{m \times N} = [U]_{m \times m} \times [S]_{m \times N} \times [V]^T_{N \times N} \quad (3.1)$$

where ‘E’ is the original ‘ $m \times N$ ’ ECG data which is decomposed into three different matrices U, S, and V. Here ‘U’ is an orthogonal  $m \times m$  matrix, ‘S’ is a  $m \times N$  matrix – where the lead  $m \times m$  matrix is diagonal, and ‘V’ is an orthogonal  $N \times N$  matrix. A more compacted form of (3.1) can be written as follows,

$$[E]_{m \times N} = [R]_{m \times N} \times [V]^T_{N \times N} \quad (3.2)$$

Here ‘R’ represents the transmission matrix obtained through SVD analysis. The Singular value matrix is represented as ‘V’, and 3 dominant singular values are selected whose effect is profoundly noticed in E. These three singular values are named as ‘D’. Quantitatively we can say that 0.022 Normalized Root Mean Squared Error (NRMSE) for the reconstruction of mECG and 0.086 NRMSE for the reconstruction of fECG was obtained from this approach of separating the dominant singular values. The basis signals from mECG and fECG extracted from the SVD process is shown in Fig. 3.4 and Fig. 3.6. The Reconstructed fECG and mECG signals using SVD approach are shown in Fig.3.5 and Fig.3.7. In a similar fashion, we represent the first three columns of the original transmission matrix ‘R’ and rename it as ‘ $R_3$ ’.

$$[D] \triangleq [V]^T_{3 \times N} \quad (3.3)$$

$$[R_3] = [R]_{m \times 3} \quad (3.4)$$

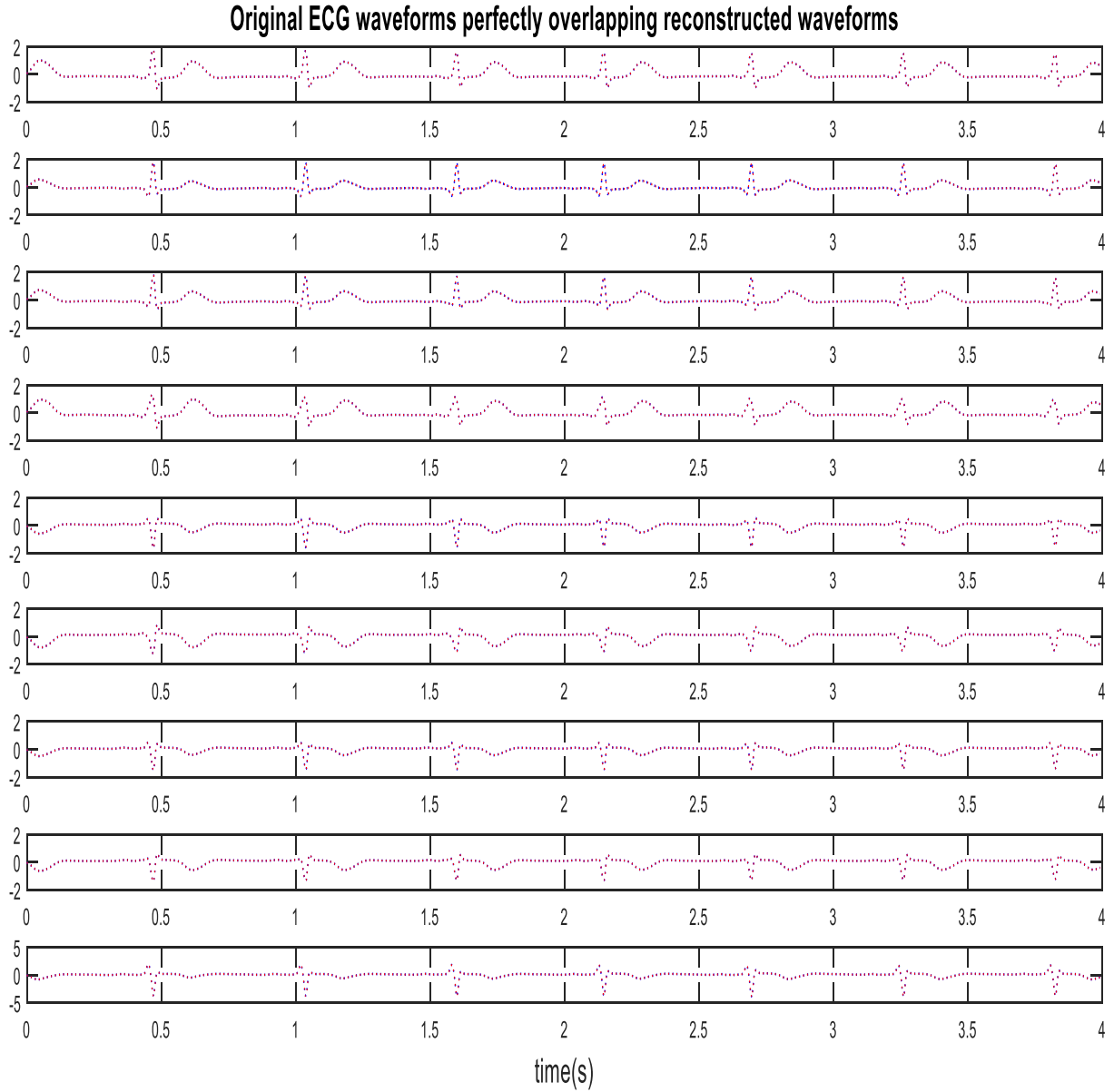


Figure 3.5: Representing the original ECG signals and the reconstructed perfectly overlapping signals for mECG (through SVD approach)

The basis signals ‘D’, thus obtained are used for further analysis through COMSOL on the 3D-CD model inside the ellipsoid which will be explained in detail in the following subsection.



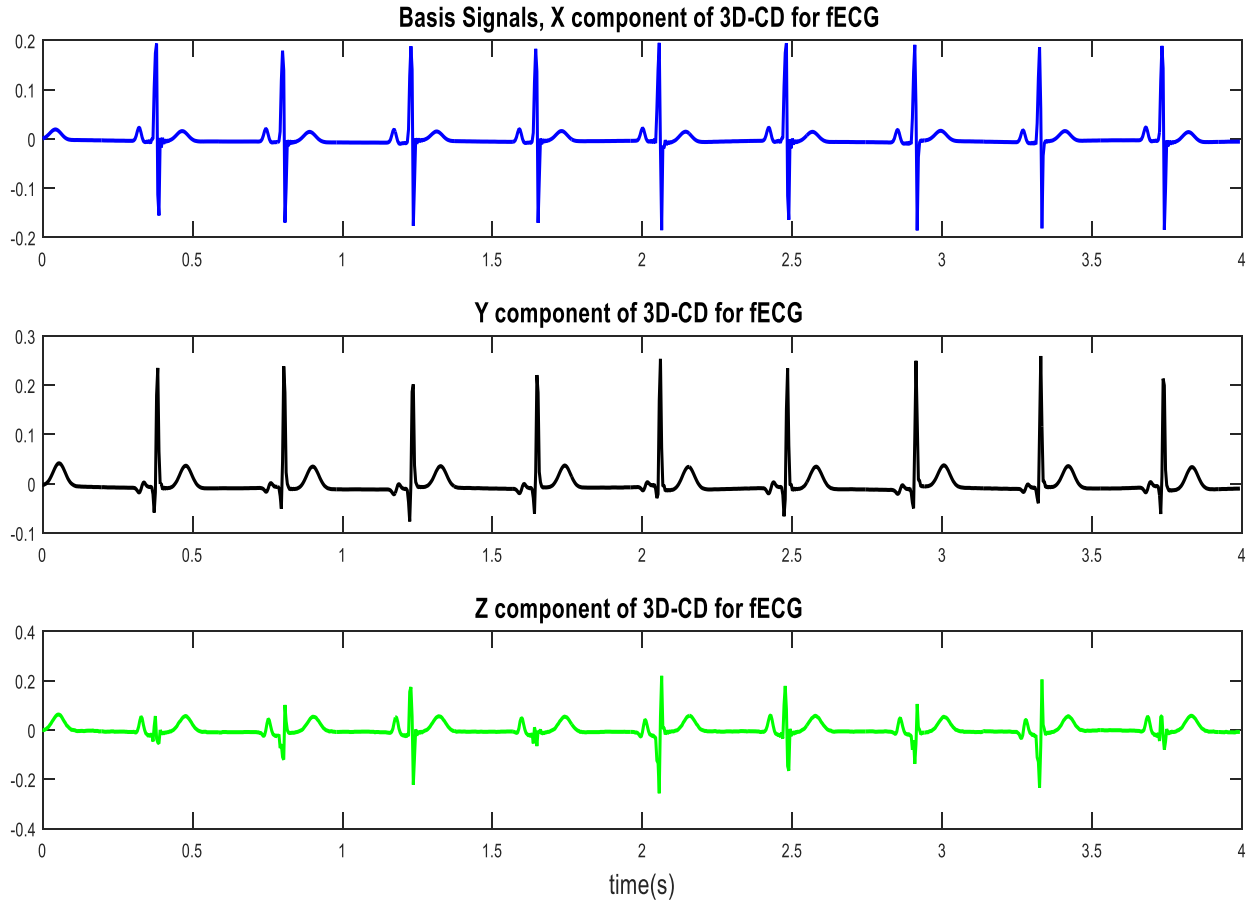


Figure 3.6: Representing basis signals for the 3D-CD extracted from fECG

### 3.4. Simulation of Bathtub-Ellipsoid Model in Water Medium (Section 2)

This research reinvestigates an innovative approach [29] which utilized an unassisted bathtub approach of ECG recording using water as the conducting medium. The subject whose ECG was to be monitored has to lay in a Bathtub filled with tap water and passive sensing probes attached to the inner surface of the bathtub will record the ECG from the subject. The present research employs a 3-dimensional current dipole (3D-CD) simulation model for representing the activity of a human heart. In this research, COMSOL tool is employed for simulating a realistic bathtub and a 3D-CD for analyzing the potential distribution sensed by the passive sensing probes attached on different faces of the bathtub as shown in Fig. 3.8.

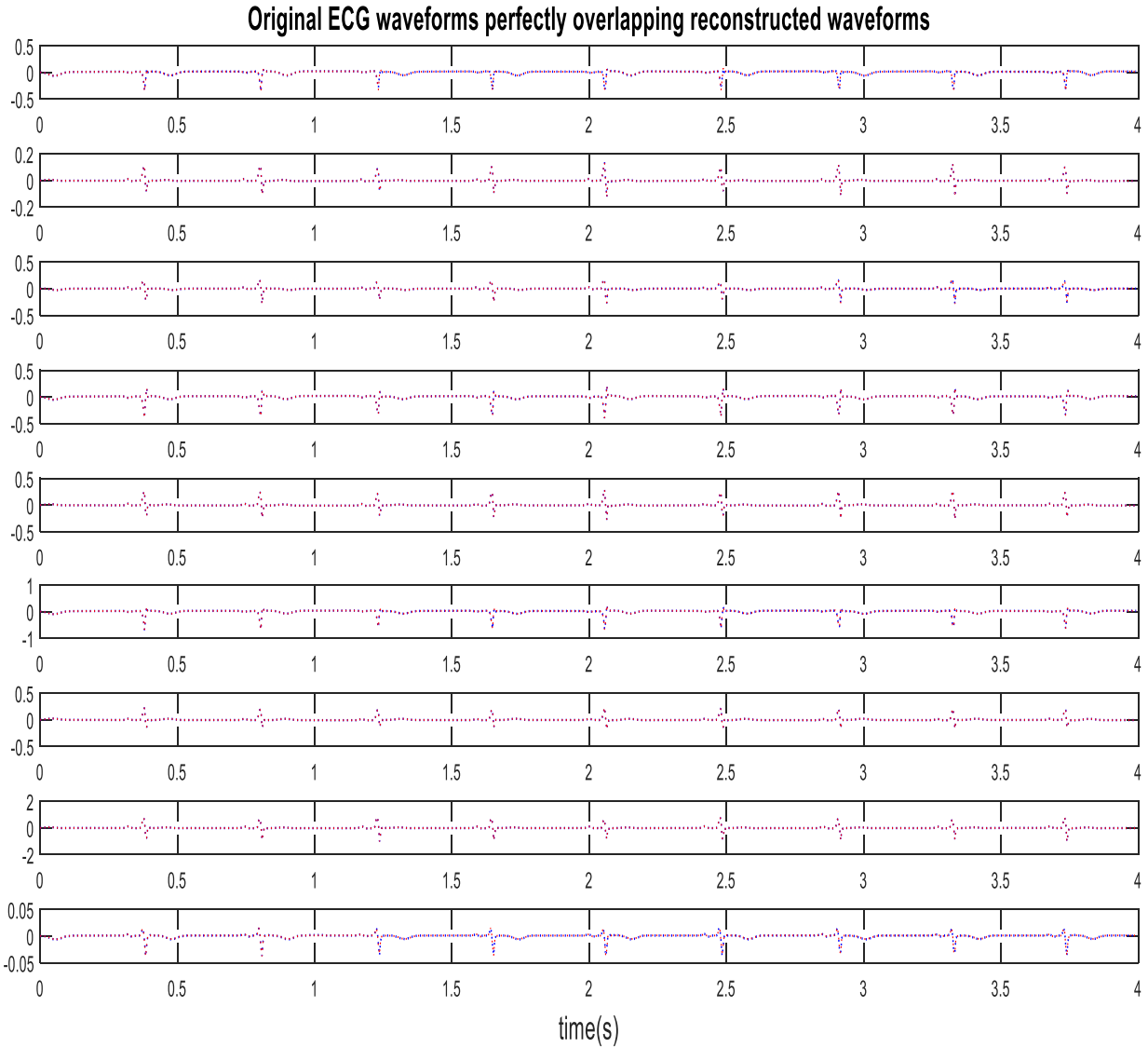


Figure 3.7: Original fECG and reconstructed fECG signals (through SVD approach)

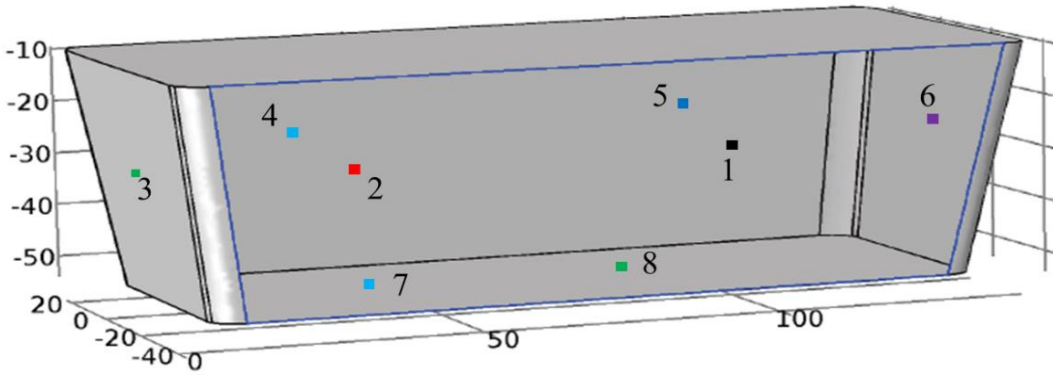


Figure 3.8: Showing the locations of the electrodes in the bathtub; #1, #2 are on the front surface; #3, #6 are on the side surface; #4, #5 are on the back surface; #7, #8 are on the bottom surface.

### 3.4.1. 3-Dimensional Current Dipole

This research utilizes the concept of a current dipole and represents the vector dipole as 3-dimensional-current-dipole (3D-CD). The dipoles on all the three axes act simultaneously for mimicking the electrical behavior of the heart. The 3D CD can be visualized as shown in Fig. 3.9.

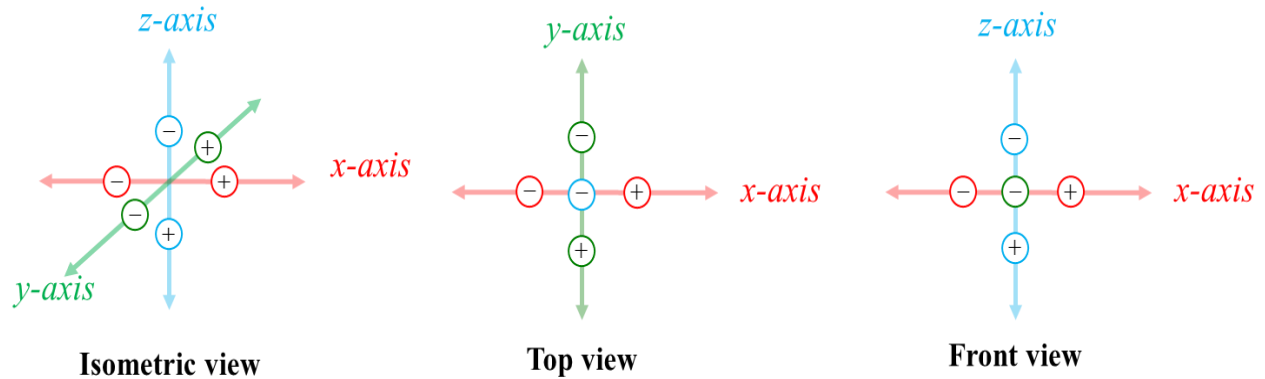


Figure 3.9: 3D-current dipole

The activities of the 3D-CD can be recorded and analyzed using any analysis software. The 3D-CD was used on a model of the bathtub (created using Solid Works) and was analyzed using basis signals extracted from SVD as well as artificially generated signals for recording the potential distribution of the 3D-CD on the inner surface of the bathtub using passive sensing probes.

The details of the inner dimensions of the bathtub created using Solid Works are 142.5 cm x 67.05 cm x 45 cm. Probes added via COMSOL for recording the time-dependent activity of the 3D-CD and is shown in Fig. 3.8.

The output response which is recorded by applying a basis signal on the 3D-CD inside the bathtub is shown in Fig. 3.10. The Potential distribution on the surface of the bathtub for a stationary analysis is given in Appendix B this potential distribution pattern enabled the placement of probes for efficient signal capture.

### 8 Electrode signals recorded form Bathtub

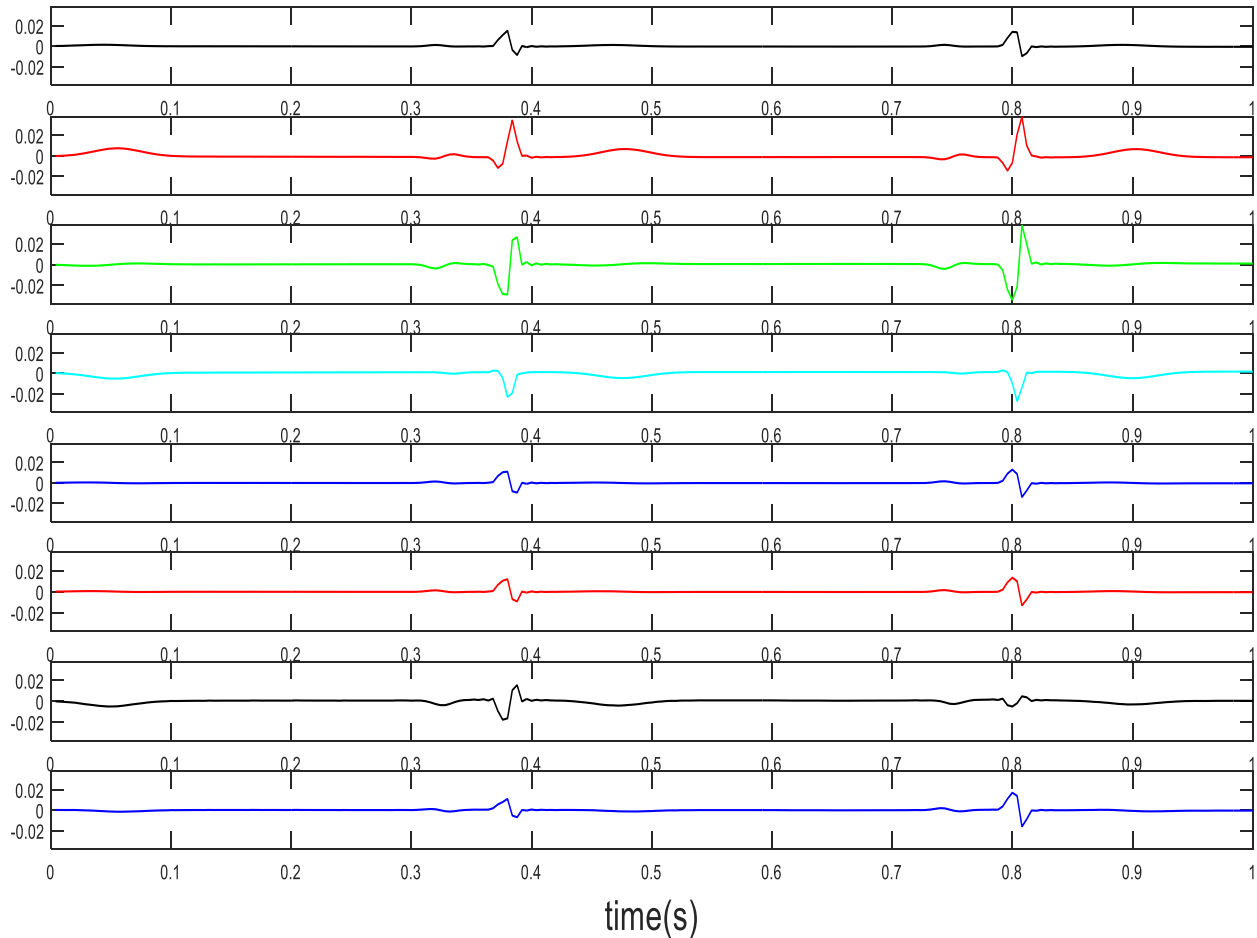


Figure 3.10: Signals recorded from the bathtub sensing electrodes for 3D-CD responding to fECG basis signals

#### 3.4.2. Analysis of Single Ellipsoidal Phantom in Water Medium

An ellipsoidal phantom is used to represent the human torso (it is proved using simulation models that with considerable accuracy the human torso shape can be approximated to the simplest of shapes, proof and details are given in Appendix B). The dimensions of the ellipsoid are 70 cm×52 cm×30 cm which is almost equal to a human torso. The overall conductivity inside the ellipsoid is taken to be 0.21 S/m. The model is placed inside the bathtub containing tap water of conductivity 0.05 S/m. This represents an adult laying inside a bathtub equipped with sensing electrodes on its inner surface and filled with tap water.

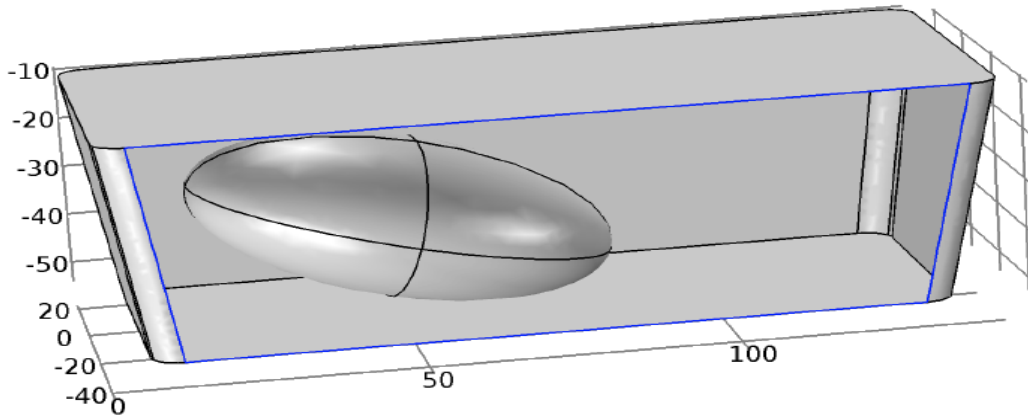


Figure 3.11: Showing a single ellipsoid placed in the bathtub (front face of bathtub removed for image)

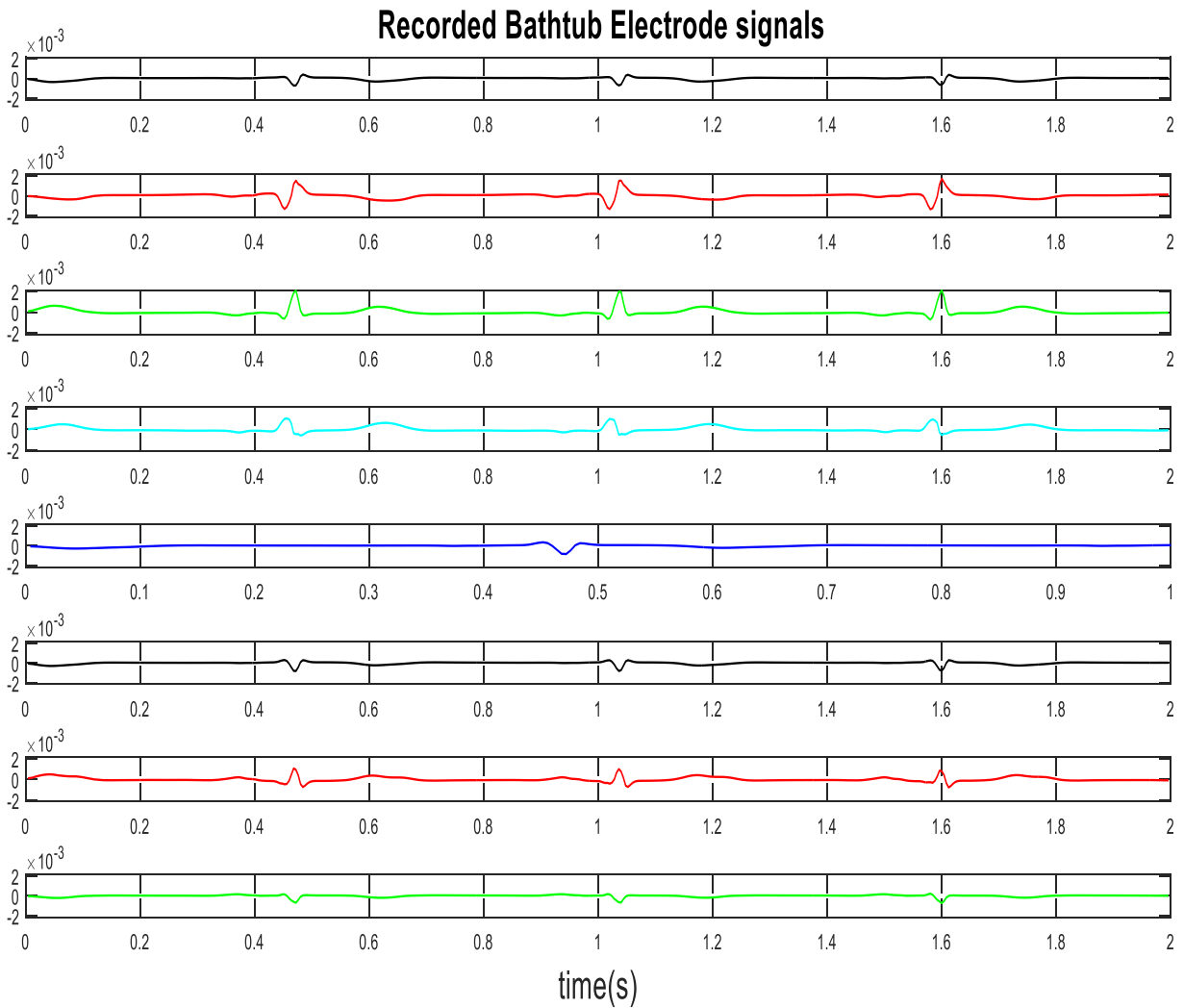


Figure 3.12: Electrode signals recorded from the bathtub for mECG basis signals exciting the 3D-CD inside the single ellipsoid model

To represent the heart's electrical activity, a 3D-CD is added at an off-centered location inside the ellipsoid. The strength of the 3D-CD is 10 mA-cm which is chosen after a thorough examination of literature (Refer to Table A.1 in Appendix A.2). The bathtub is tapped with probes at a finite number of points, particularly passive probes. Recorded bathtub potential distribution plots are shown in Fig. 3.11 and can be analyzed further with the help of MATLAB. Single ellipsoid model inside a bathtub can be visualized as seen in Fig. 3.12. The result of the potential distribution due to the activities of the 3D-CD on the single ellipsoidal phantom resting inside the bathtub are given in the following figures. Synthetic signals (Fig. 3.13 and Fig. 3.15) were applied as inputs to excite the 3D-CD, and the observed potential distribution which was recorded are displayed in Fig. 3.14 and Fig. 3.16 these distributions will be used in the computation of the sensing matrix.

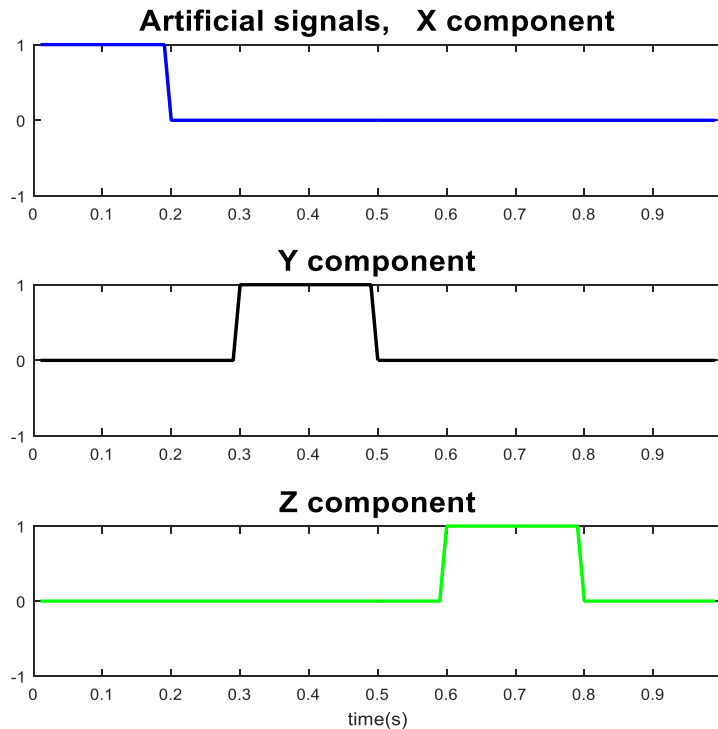


Figure 3.13: Non-overlapping synthetic signals exciting the 3D-CD

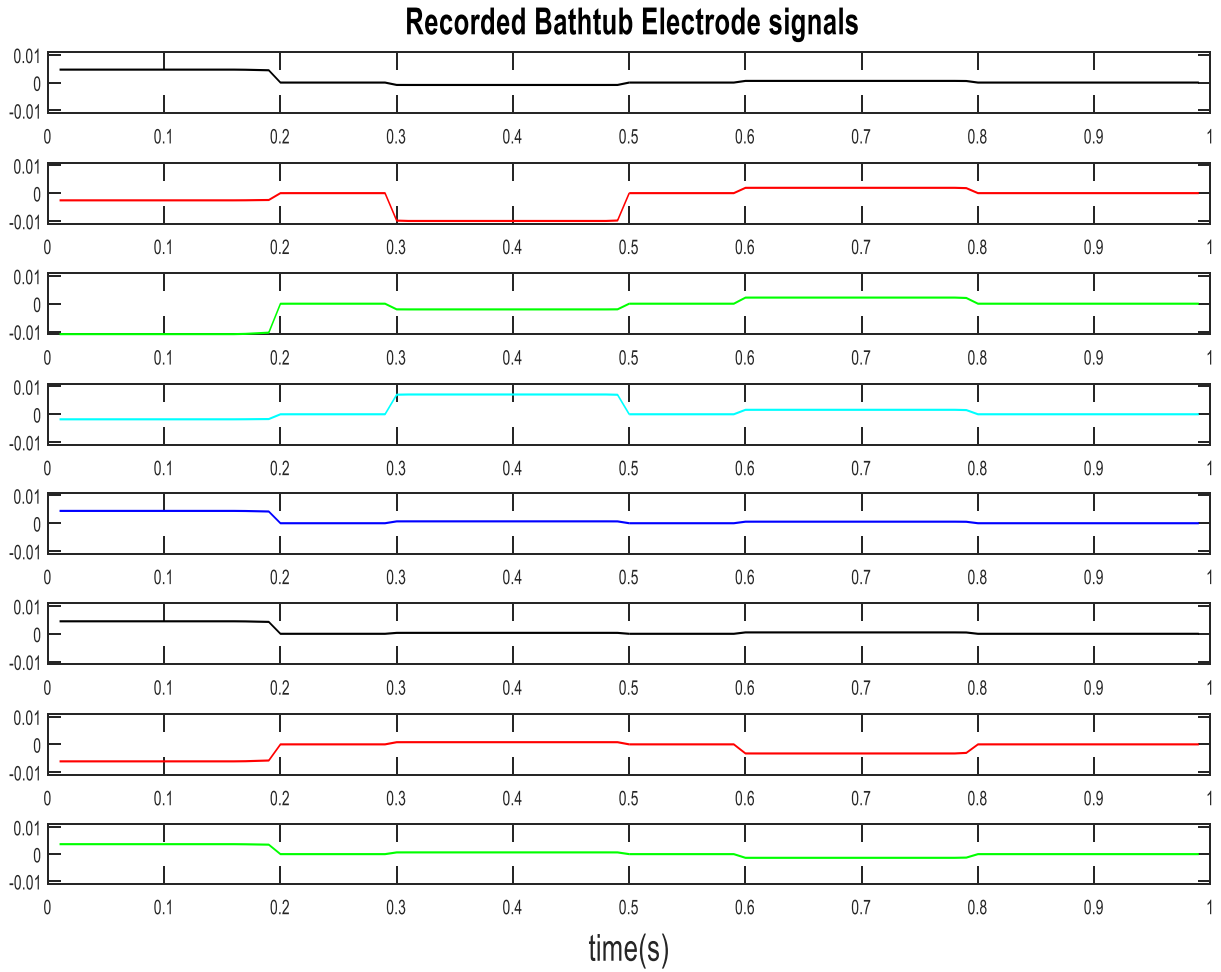


Figure 3.14: Potential distribution recorded by the sensing probes on the inner surface of the bathtub for non-overlapping synthetic signals exciting the 3D-CD

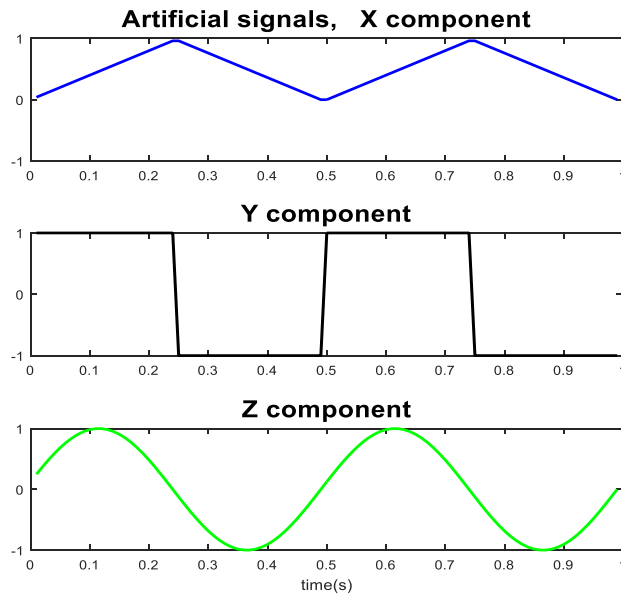


Figure 3.15: Overlapping synthetic signals exciting the 3D-CD

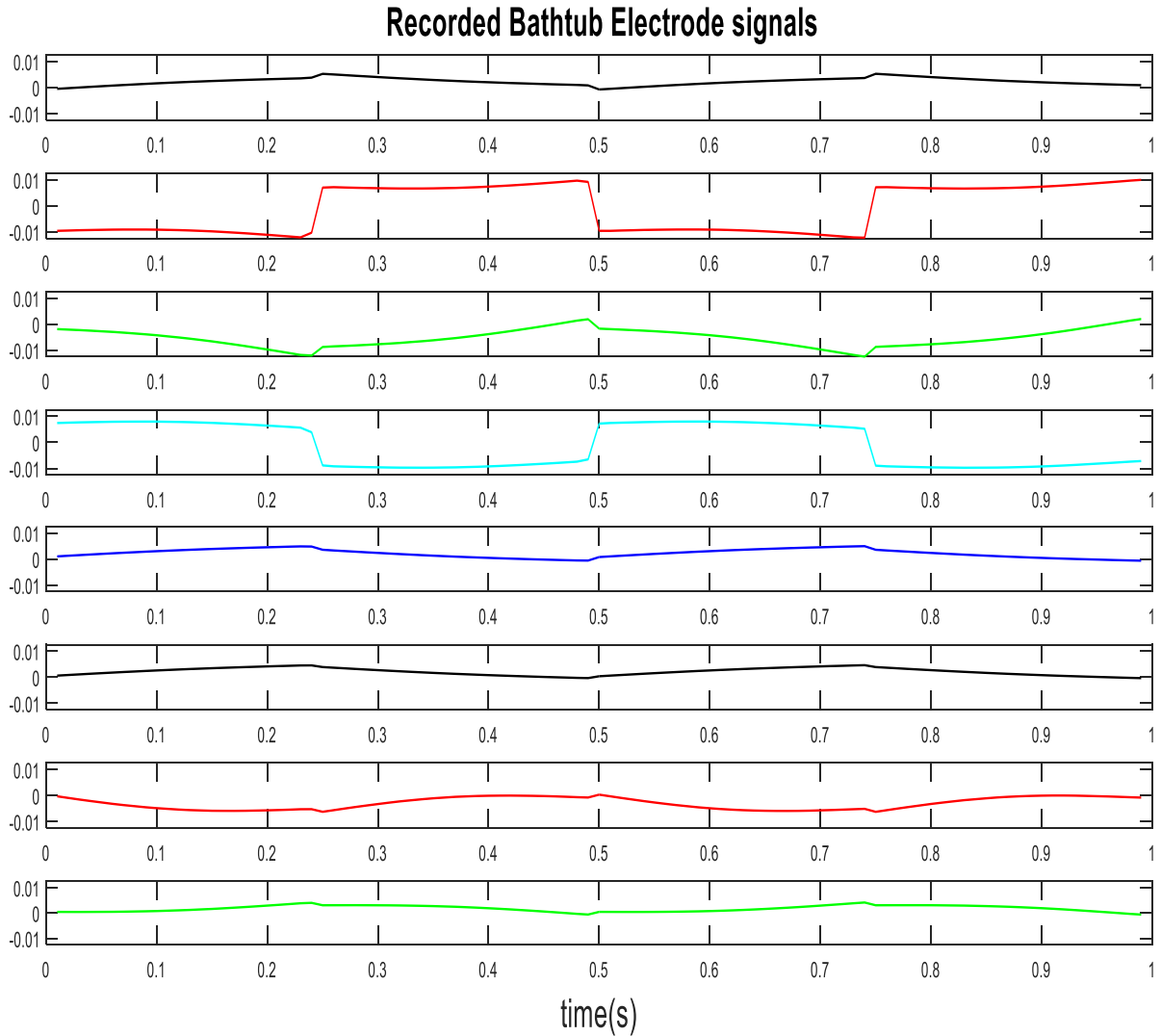


Figure 3.16: Potential distribution recorded by the sensing probes on the inner surface of the bathtub for overlapping synthetic signals exciting the 3D-CD

### 3.4.3. Analysis of Double Ellipsoidal Phantom in Water Medium

As an extended topic of this research, double ellipsoidal phantoms were employed (in approximately the dimensions of the torso of a pregnant subject) with the second smaller ellipsoid representing the fetus (or baby) both containing their own 3D-CD's for the representation of the heart. The conductivity of the smaller ellipsoid is assumed to be 0.18 S/m, and the bigger ellipsoid is assumed to be 0.21 S/m and the dipole moment of the 3D-CD inside the smaller ellipsoid is 2 mA-cm, and the bigger ellipsoid has a 3D-CD having a dipole moment of 10 mA-cm. The setup



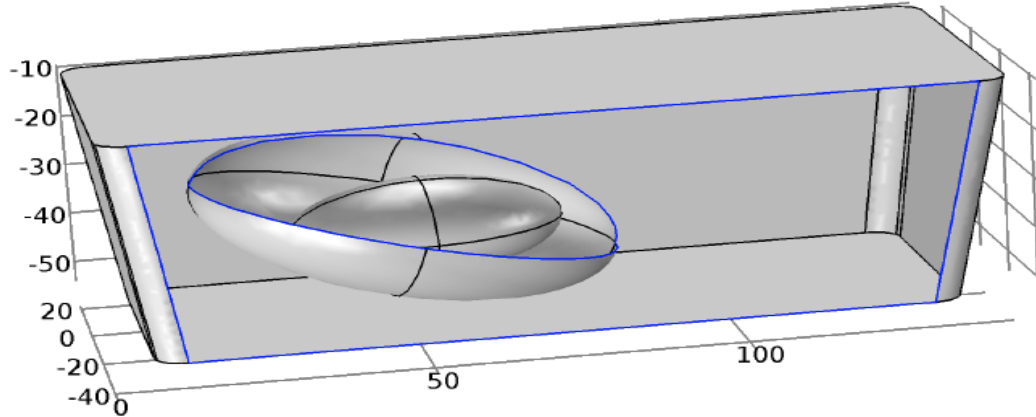


Figure 3.17: Showing the two ellipsoids (pregnant subject and the fetus) placed in the bathtub.

of these two ellipsoids inside the bathtub is shown in Fig. 3.17. In this case, the potential distribution due to the activity of the 3D-CDs is captured at a finite number of points, specifically at the passive probes on the inner surface of the bathtub, which act as sensing system. The plot in Fig 3.18 represents the activity of two 3D-CDs in the bathtub ellipsoid model. The simulation is performed for a total span of 4 seconds; the sampling interval is 4 ms, which results in 1000 points of ECG data; note the sampling frequency is 250Hz. The results which are obtained through the COMSOL simulation for the three cases, (a) 3D-CD inside a bathtub, (b) one 3D-CD inside an Ellipsoidal phantom laying inside the bathtub, and (c) two 3D-CD's inside two ellipsoidal phantoms laying inside the bathtub can be used in the next section to extract the Sensing matrix for representing the characteristics of the 3D-CD.

### 3.5. Extraction of Sensing Matrix (Section 3)

The potential distribution observed around the bathtub as seen through one of the three cases mentioned in the previous subsection is the result of the transformation of the basis signals and can be represented by the following equation.

$$[ B ] = [ A ] \times [ D ] \quad (3.5)$$

where the matrix  $\mathbf{B}$  denotes the potential distribution on the inner surface of the bathtub at the electrode locations,  $\mathbf{D}$  is the basis signals, and  $\mathbf{A}$  is the sensing matrix.

The sensing matrix can be back extracted using

$$[\mathbf{A}] = [\mathbf{B}] \times [\mathbf{D}]^T \times ([\mathbf{D}] \times [\mathbf{D}]^T)^{-1} \quad (3.6)$$

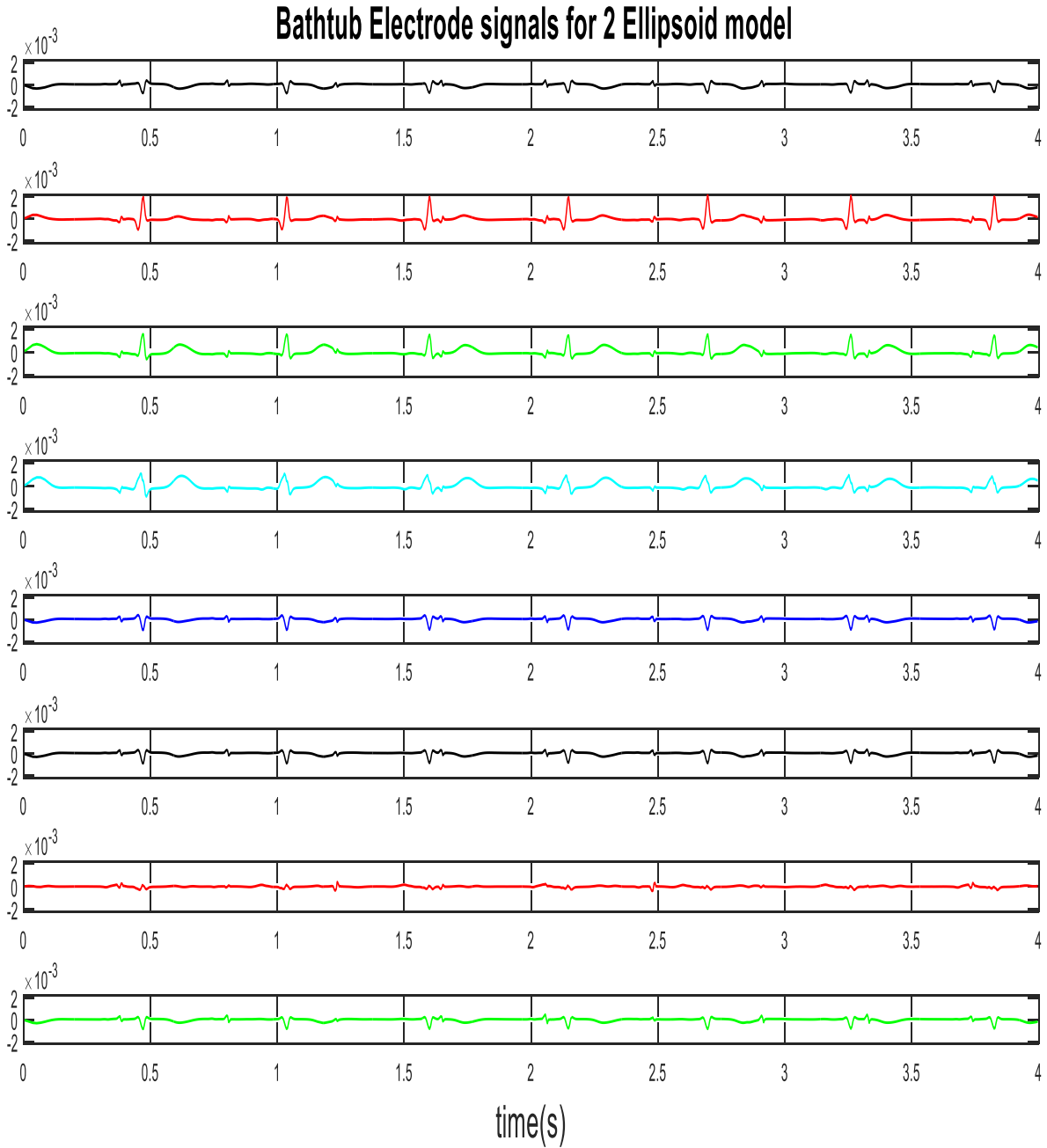


Figure 3.18: Potential distribution plot observed at the bathtub probes for the activity of two 3D-CD in the two ellipsoidal phantoms

For the purpose of verifying the sensing matrix found, basis signals and synthetic overlapping signals were used to excite the 3D-CD in the COMSOL models. The results from two cases are discussed in 3.5.1 and 3.5.2.

### 3.5.1. Case Study for Single Ellipsoidal Phantom in Water Medium

Two forms of synthetic signals, fECG and mECG basis signals were used to excite the 3D-CD in single ellipsoid model in the bathtub and it was noticed that the dominant dipole amongst the 3 orthogonal-dipoles was found to be the dipole oriented in the X-direction, the second highest dominance was from the Y-direction dipole and the least contribution was from the dipole oriented in the Z-direction. (Details on how dimensions of medium affect the potential distributions due to a dipole is given in Appendix B)

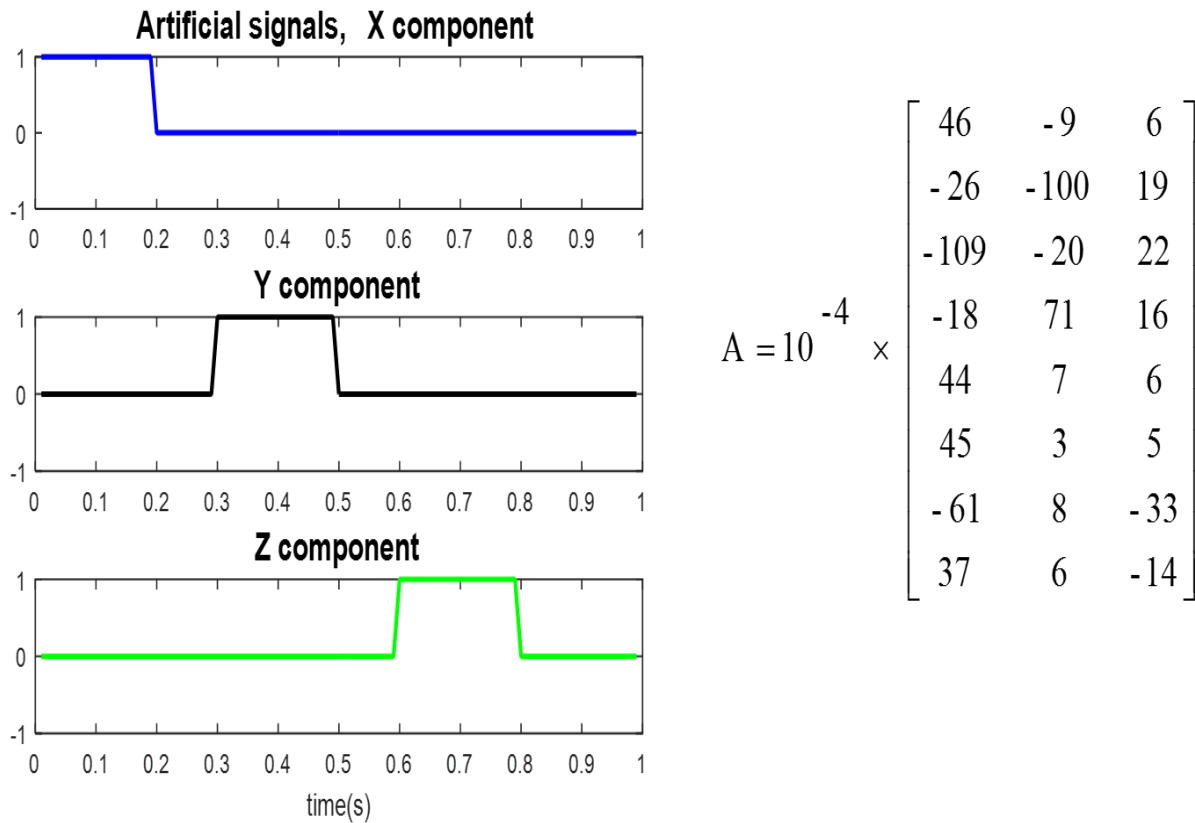


Figure 3.19: Non-overlapping synthetic signals acting as input to 3D-CD in one ellipsoid model and 8×3 sensing matrix extracted is shown on the right.

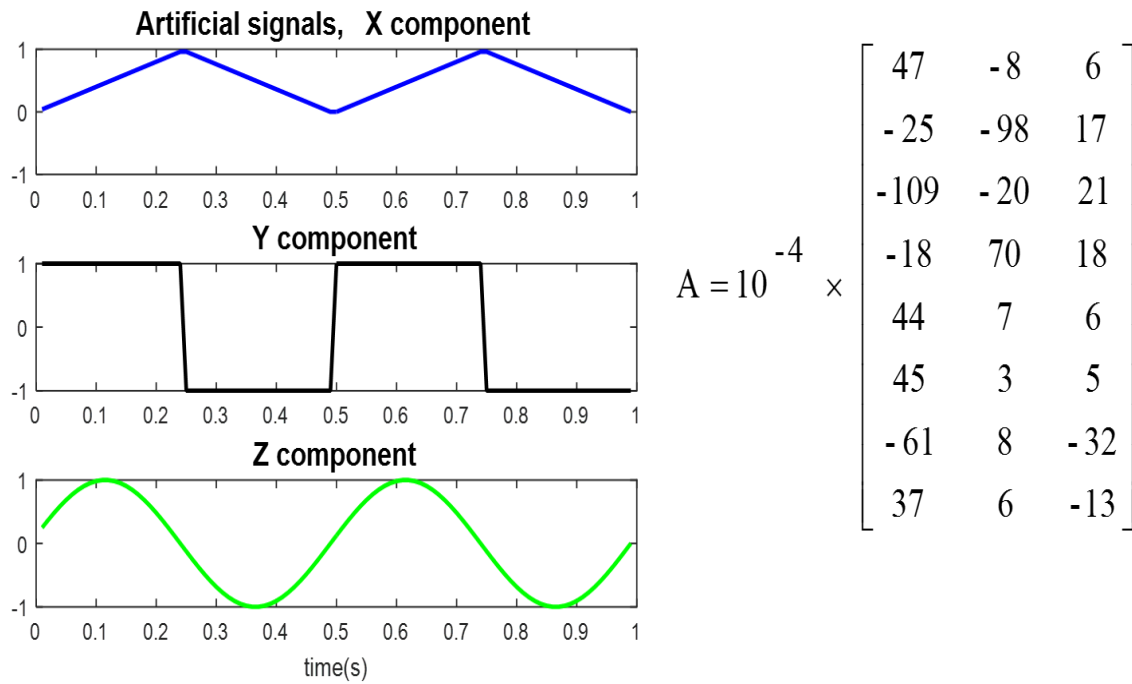


Figure 3.20: Overlapping synthetic signals acting as input to 3D-CD in one ellipsoid model and  $8 \times 3$  sensing matrix extracted is shown on the right.

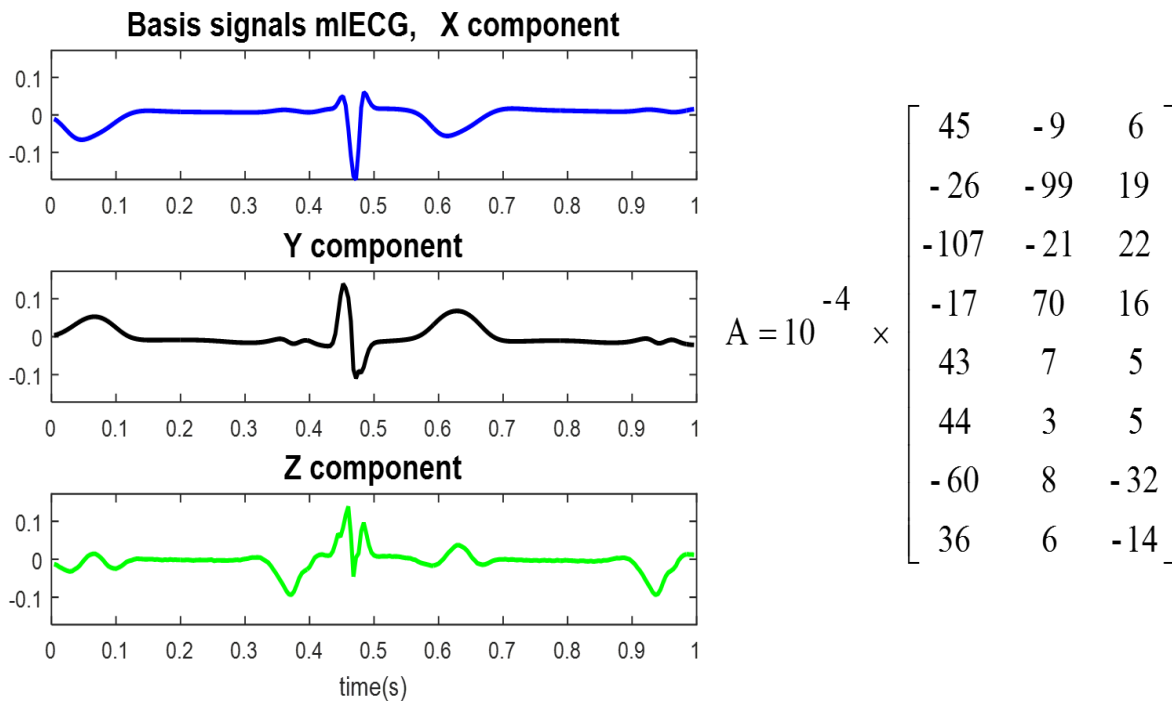


Figure 3.21: mIECG basis signals acting as input to 3D-CD in one ellipsoid model and  $8 \times 3$  sensing matrix extracted is shown on the right.

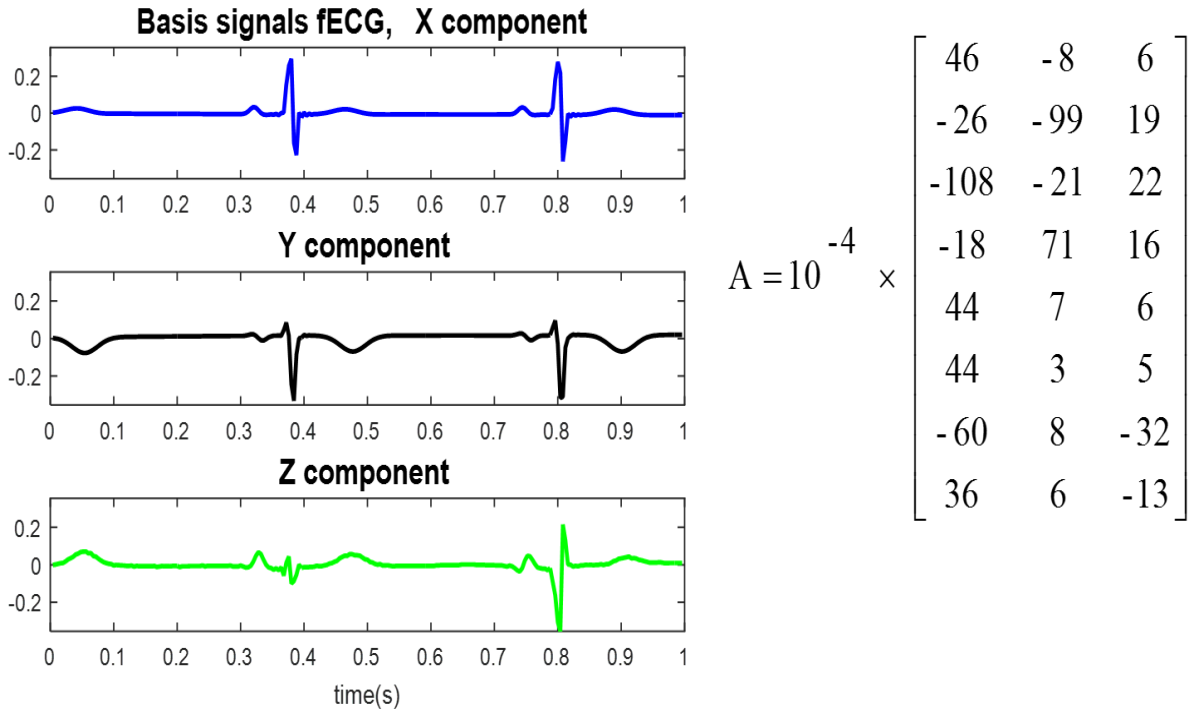


Figure 3.22: fECG basis signals acting as input to 3D-CD in one ellipsoid model and 8×3 sensing matrix extracted is shown on the right.

A comment can be made on the Sensing matrix which is obtained, the sensing matrix is of 8 x 3 dimension as the number of rows represents the number of passive sensing probes attached on the surface of the bathtub and the number of columns represents the 3D-CD basis signals. It can be inferred that the sensing matrix ‘A’ which is extracted with the help of bathtub electrode probes are almost the same when four different types of signals are exciting the 3D-CD. The maximum Normalized Root-Mean-Squared Difference (NRMSD) amongst the comparison of sensing matrix obtained from the four cases is found to be 0.026.

### 3.5.2. Case Study for Double Ellipsoidal Phantom in Water Medium

For this particular case, a smaller ellipsoid inside a bigger ellipsoid is present to represent the two ellipsoidal phantom model. Two different types of signals are used to excite 3D-CD inside each ellipsoid. The result for the case of synthetic signals and basis signals exciting the 3D-CD is

discussed below. A note almost similar to the case I is applicable here, the dominance of X-direction oriented dipoles are more than dipoles oriented in any other direction. Fig. 3.23 and Fig.

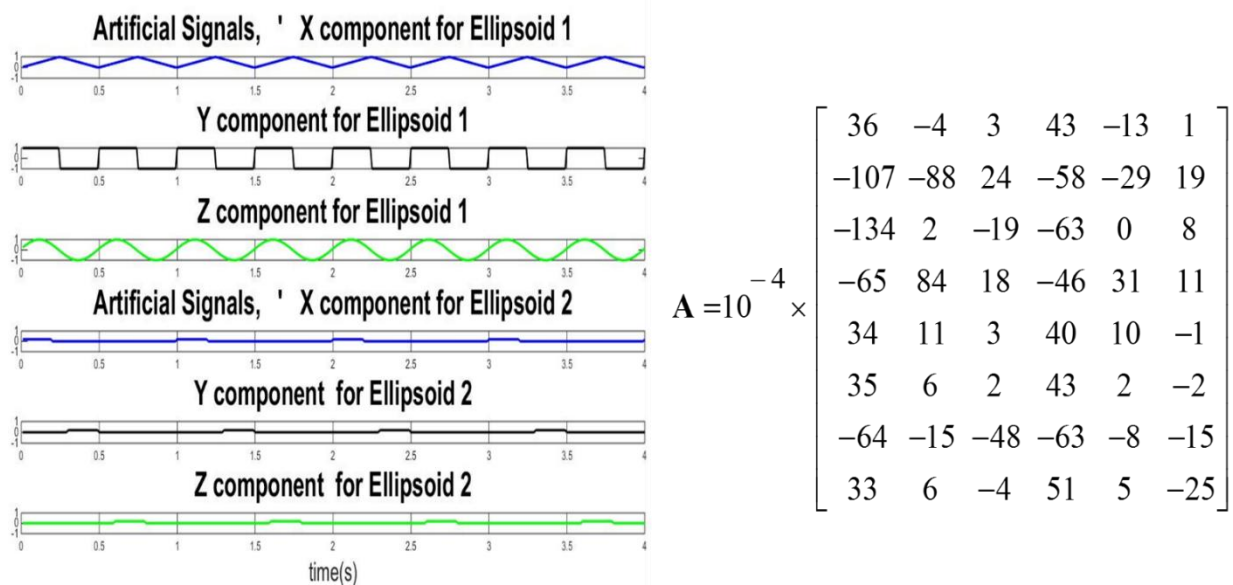


Figure 3.23: Two different types of synthetic signals exciting the two 3D-CDs inside two ellipsoids and  $8 \times 6$  sensing matrix extracted is shown on the right.

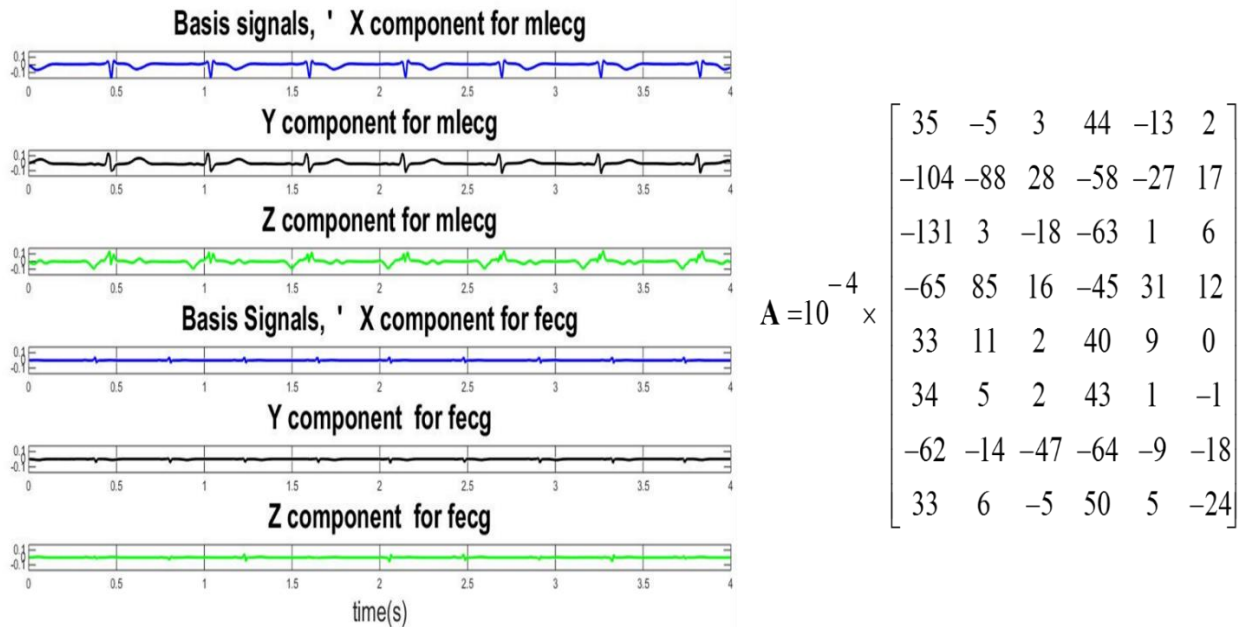


Figure 3.24: Basis signals from fIECG and mIECG (derived from mIECG) exciting the two 3D-CDs inside two ellipsoids and  $8 \times 6$  sensing matrix extracted is shown on the right.

3.24 give details on the type of signals used to excite each ellipsoidal phantom and the sensing matrix which was extracted from each case.

The NRMSE between the sensing matrices obtained is 0.032. From the two case studies which were discussed, it can be inferred that the concept of sensing matrix is valid.

### 3.6. Reconstruction of Basis Signals using Sensing Matrix (Section 4)

The sensing matrix which was extracted with the help of the bathtub signals can be reused to reconstruct the information about the 3D-CD signals using,

$$[\hat{D}] = ([A]^T \times [A])^{-1} \times [A]^T \times [B] \quad (3.7)$$

where ‘B’ is the potential distribution signals mapped by the sensing probes located at the inner surface of the bathtub, ‘A’ is the sensing matrix, and ‘D’ is the basis signals which is reconstructed. The Table (3.1) shows the NRMSE observed for reconstruction of different type of test signals which are used to excite the 3D-CD in the COMSOL model. A plot of reconstructed basis signal overlapping the original basis signal extracted is shown in Fig. 3.25

The original ECG signals ‘E’ can also be reconstructed as the intermediary transmission matrix R3 is known.

Table 3.1: NRMSE for reconstruction of different type of signals applied to the 3D-CD in COMSOL

	Type of Signal being reconstructed	Number of ellipsoids	NRMSE for D-hat
1	Overlapping synthetic	1	0.016
2	3-D basis extracted from mECG	1	0.045
3	3-D Basis extracted from fECG	1	0.024
4	Two synthetic 3-D signals applied on two 3D-CD	2	0.024
5	Two 3-D basis signals applied on two 3D-CD	2	0.035

$$[\hat{E}]_{m \times N} = [R_3]_{m \times 3} \times [D]_{3 \times N} \quad (3.8a)$$

$$[\hat{\hat{E}}]_{m \times N} = [R_3]_{m \times 3} \times [\hat{D}]_{3 \times N} \quad (3.8b)$$

The NRMSE observed in reconstructing the actual ECG data given in (3.8a) is found to be 0.039. Thus as a concluding remark on this chapter, can be said that extraction of the sensing matrix is possible, using which we can reconstruct the source signals of the 3D-CD.

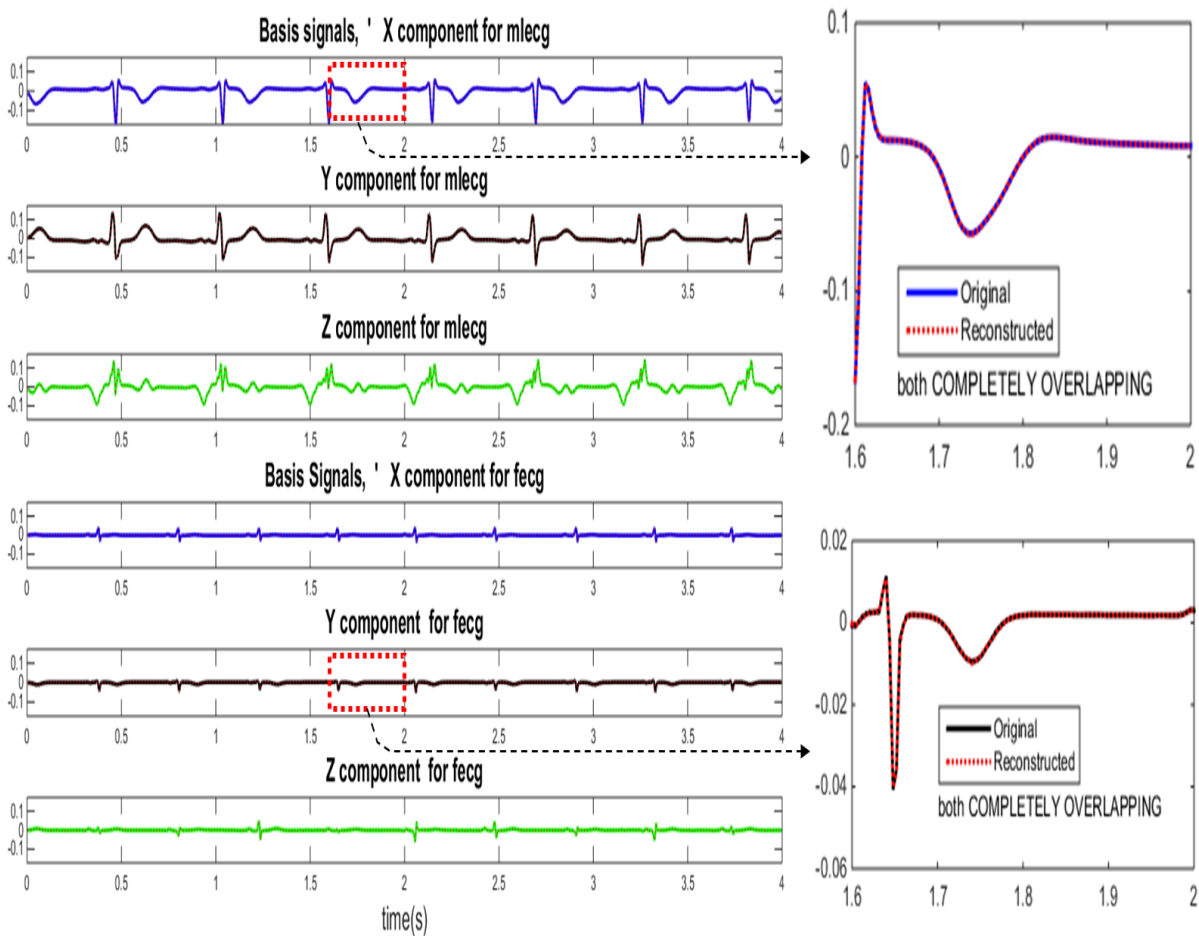


Figure 3.25: Highly overlapping original basis signals and reconstructed basis signals; magnified sections are shown on the right.

A joint paper by the author and his major professor (Dr. V. K. Jain) is in preparation which largely subsumes the concepts discussed in this chapter.



## CHAPTER 4: CONCLUSIONS

### 4.1. Conclusions

With emphasis on inversion and accurate reconstruction, this thesis has employed SVD decomposition and to estimate the time varying vector ECG dipoles and also reinvestigated, via simulation, an important method for unassisted ECG measurement in liquid media. On the surface of the container of that liquid are placed the sensing electrodes. Two case studies where single 3D-current dipole and double 3D-current dipoles inside a single and double ellipsoidal phantom of dimensions resembling an adult torso and pregnant subject with fetus, respectively, were used to successfully extract the sensing matrix which is responsible for transforming the electrical activity of the heart into the potential distribution on the surface of the container. Using advanced simulation, this thesis has demonstrated that the 3D-CD signals could be successfully reconstructed using the sensing matrix and the outputs at the container leads from the simulation, and in turn using this information the original ECG data was reconstructed with low Normalized Root Mean Squared Error.

### 4.2. Future Work

The areas in which further investigation should be performed in the future are the following:

- Experimental verification
- Separation of mECG and fECG signals from the potential distribution recorded on the surface of the medium using Independent Component Analysis [57]-[59] or JadeR [60]

- Theoretical investigation to estimate the potential distribution on the surface of the medium by a bioelectric source inside three conducting sub-regions.

## REFERENCES

- [1] Giffard-Roisin, S., Jackson, T., Fovargue, L., Lee, J., Delingette, H., Razavi, R., & Sermesant, M. (2016). Non-Invasive Personalisation of a Cardiac Electrophysiology Model from Body Surface Potential Mapping. *IEEE Transactions on Biomedical Engineering*.
- [2] Pei, W., Zhang, H., Wang, Y., Guo, X., Xing, X., Huang, Y., & Chen, H. (2016). Skin-potential variation insensitive dry electrodes for ECG recording. *IEEE Transactions on Biomedical Engineering*.
- [3] Yokus, M. A., & Jur, J. S. (2016). Fabric-based wearable dry electrodes for body surface biopotential recording. *IEEE Transactions on Biomedical Engineering*, 63(2), 423-430.
- [4] Freeman, D. K., Gatzke, R. D., Mallas, G., Chen, Y., & Brouse, C. J. (2015). Saturation of the Right-Leg Drive Amplifier in Low-Voltage ECG Monitors. *IEEE Transactions on Biomedical Engineering*, 62(1), 323-330.
- [5] Da He, D., Winokur, E. S., & Sodini, C. G. (2015). An ear-worn vital signs monitor. *IEEE Transactions on Biomedical Engineering*, 62(11), 2547-2552.
- [6] Varon, C., Caicedo, A., Testelmans, D., Buyse, B., & Van Huffel, S. (2015). A novel algorithm for the automatic detection of sleep apnea from single-lead ECG. *IEEE Transactions on Biomedical Engineering*, 62(9), 2269-2278.
- [7] Reyes, B. A., Posada-Quintero, H. F., Bales, J. R., Clement, A. L., Pins, G. D., Swiston, A., & Chon, K. H. (2014). Novel electrodes for underwater ECG monitoring. *IEEE Transactions on Biomedical Engineering*, 61(6), 1863-1876.
- [8] Lim, K. M., Jeon, J. W., Gyeong, M. S., Hong, S. B., Ko, B. H., Bae, S. K., & Shim, E. B. (2013). Patient-specific identification of optimal ubiquitous electrocardiogram (U-ECG) placement using a three-dimensional model of cardiac electrophysiology. *IEEE Transactions on Biomedical Engineering*, 60(1), 245-249.
- [9] Lin, B. S., Chou, W., Wang, H. Y., Huang, Y. J., & Pan, J. S. (2013). Development of novel non-contact electrodes for mobile electrocardiogram monitoring system. *IEEE journal of translational engineering in health and medicine*, 1, 1-8.

- [10] Lee, J., Reyes, B. A., McManus, D. D., Maitas, O., & Chon, K. H. (2013). Atrial fibrillation detection using an iPhone 4S. *IEEE Transactions on Biomedical Engineering*, 60(1), 203–206.
- [11] Wang, Y., Agrafioti, F., Hatzinakos, D., & Plataniotis, K. N. (2007). Analysis of human electrocardiogram for biometric recognition. *EURASIP journal on Advances in Signal Processing*, 2008(1), 148658.
- [12] Pullan AJ, Cheng LK, Nash MP, Bradley CP, Paterson DJ. Noninvasive electrical imaging of the heart: theory and model development. *Ann. Biomed. Eng. Oct.*; 2001 29(10):817–836. [PubMed:11764313]
- [13] Huiskamp G, Greensite F. A new method for myocardial activation imaging. *IEEE Trans. Biomed. Eng. Jun.*; 1997 44(6):433–446. [PubMed: 9151476]
- [14] Tilg B, Fischer G, Modre R, Hanser F, Messnarz B, Schocke M, Kremser C, Berger T, Hintringer F, Roithinger FX. Model-based imaging of cardiac electrical excitation in humans. *IEEE Trans. Med. Imaging. Sep.*; 2002 21(9):1031–1039. [PubMed: 12564871] Han et al. Page 10 *IEEE Trans Med Imaging*. Author manuscript; available in PMC 2009 November 1. NIH-PA Author Manuscript NIH-PA Author Manuscript NIH-PA Author Manuscript
- [15] Greensite, F. Heart surface electrocardiographic inverse solutions. In: He, B., editor. *Modeling and Imaging of Bioelectric Activity—Principles and Applications*. Kluwer Academic/Plenum; New York: 2004. p. 119-160.
- [16] Gulrajani RM, Roberge FA, Savard P. Moving dipole inverse ECG and EEG solutions. *IEEE Trans. Biomed. Eng. Dec.*; 1984 31(12):903–910. [PubMed: 6396217]
- [17] Greensite F, Huiskamp G. An improved method for estimating epicardial potentials from the body surface. *IEEE Trans. Biomed. Eng. Jan.*; 1998 45(1):98–104. [PubMed: 9444844]
- [18] He B, Wu D. Imaging and Visualization of 3-D Cardiac Electric Activity. *IEEE Trans. Inf. Technol. Biomed. Sep.*; 2001 5(3):181–186. [PubMed: 11550839]
- [19] He B, Li G, Zhang X. Noninvasive three-dimensional activation time imaging of ventricular excitation by means of a heart-excitation-model. *Phys. Med. Biol. Nov.*; 2002 47(22):4063–078. [PubMed: 12476982]
- [20] Zhang X, Ramachandra I, Liu Z, Muneer B, Pogwizd SM, He B. Noninvasive three-dimensional electrocardiographic imaging of ventricular activation sequence. *Am. J. Physiol.-Heart Circul. Physiol. Dec.*; 2005 289(6):H2724–H2732.
- [21] Skipa O, Nalbach M, Sachse F, Werner C, Dössel O. Transmembrane potential reconstruction in anisotropic heart model. *Int. J. Bioelectromagnetism*. 2002; 4(2):17–18.

- [22] Liu Z, Liu C, He B. Noninvasive reconstruction of three-dimensional ventricular activation sequence from the inverse solution of distributed equivalent current density. *IEEE Trans. Med. Imaging*. Oct.; 2006 25(10):1307–1318. [PubMed: 17024834]
- [23] Celler, B. G., Lovell, N. H., & Basilakis, J. (2003). Using information technology to improve the management of chronic disease. *Medical Journal of Australia*, 179(5), 242-246.
- [24] Gellis, Z. D., Kenaley, B., McGinty, J., Bardelli, E., Davitt, J., & Ten Have, T. (2012). Outcomes of a telehealth intervention for homebound older adults with heart or chronic respiratory failure: a randomized controlled trial. *The Gerontologist*, 52(4), 541-552.
- [25] Kvedar, J., Coye, M. J., & Everett, W. (2014). Connected health: a review of technologies and strategies to improve patient care with telemedicine and telehealth. *Health Affairs*, 33(2), 194-199.
- [26] R. C. Barr, M. Ramsey, III, and M. S. Spach, "Relating epicardial to body surface potential distributions by means of transfer coefficients based on geometry measurements," *IEEE Trans. Biomed. Eng.*, vol. BME-24, pp. 1–11, Jan. 1977
- [27] R. D. Throne and L. G. Olson, "A generalized eigen system approach to the inverse problem of electrocardiography," *IEEE Trans. Biomed. Eng.*, vol. 41, pp. 592–600, June 1994
- [28] Bishop, M. J., & Plank, G. (2011). Bidomain ECG simulations using an augmented monodomain model for the cardiac source. *IEEE transactions on biomedical engineering*, 58(8), 2297-2307.
- [29] Kwatra, S. C., & Jain, V. K. (1986). A new technique for monitoring heart signals-part I: instrumentation design. *IEEE transactions on biomedical engineering*, (1), 35-41 and "A new technique for monitoring heart signals; Part II Orthogonal lead extraction," pp. 1-10, *IEEE Trans. on Biomedical Engineering*, Vol. BME-33, January 1986.
- [30] Frank, E. (1954). General theory of heart-vector projection. *Circulation Research*, 2(3), 258-270.
- [31] Helmholtz, HV (1853). On some laws of the distribution of electric currents in physical conductors with application to the animal-electric experiments. *Annals of Physics*, 165 (6), 211-233.
- [32] Schwan, H. P., & Kay, C. F. (1956). Specific resistance of body tissues. *Circulation Research*, 4(6), 664-670.
- [33] Schwan, Herman P., and Calvin F. Kay. "Capacitive properties of body tissues." *Circulation Research* 5.4 (1957): 439-443.

- [34] Geselowitz, D. B. (1973). Electric and magnetic field of the heart. *Annual review of biophysics and bioengineering*, 2(1), 37-64.
- [35] Plonsey, R., & Barr, R. C. (2007). *Bioelectricity: a quantitative approach*. Springer Science & Business Media.
- [36] Geselowitz, D. B. (1967). On bioelectric potentials in an inhomogeneous volume conductor. *Biophysical journal*, 7(1), 1.
- [37] Geselowitz, D. B. (1960). Multipole representation for an equivalent cardiac generator. *Proceedings of the IRE*, 48(1), 75-79.
- [38] Gabor, D., and C. V. Nelson. "Determination of the resultant dipole of the heart from measurements on the body surface." *Journal of applied physics* 25.4 (1954): 413-416.
- [39] Goldberger AL, Amaral LAN, Glass L, Hausdorff JM, Ivanov PCh, Mark RG, Mietus JE, Moody GB, Peng CK, Stanley HE. PhysioBank, PhysioToolkit, and PhysioNet: Components of a New Research Resource for Complex Physiologic Signals. *Circulation* 101(23):e215-e220 [Circulation Electronic Pages; <http://circ.ahajournals.org/content/101/23/e215.full>]; 2000 (June 13). PMID: 10851218; doi: 10.1161/01.CIR.101.23.e215
- [40] V. K. Jain, "ECG Feature Extraction and Its Application to Automated Prognosis," *Int. J. of Computer and Information Science*, Vol. 2, pp. 231-247, September 1973.
- [41] S. C. Kwatra and V. K. Jain, "Electrocardiogram via liquid media," *Proc. AAMI 11th Ann. Meeting, J. AAMI*, Vol. 10, p. 60, Jan.-Feb. 1976.
- [42] S. C. Kwatra and V. K. Jain, "Electrocardiogram from a Bathtub," *Proc. San Diego Biomedical Symposium*, pp. 433-441, February 1974.
- [43] K. W. Watkinson, S. C. Kwatra, and V. K. Jain, "Electrocardiographic Studies on an Idealized Torso Model," *IEEE Southeastcon*, pp. P.5-1 to P.5-5, May 1973.
- [44] V. K. Jain, "A Preliminary Basis for Automated Prognosis of Heart Disease," *Proc. San Diego Biomedical Symp. -- Innovations in Biomedicine*, pp. 63-71, February 1972.
- [45] V. K. Jain, "Prognosis from Time Loci of ECG Parameters," *Proc. Hawaii Intntl. Conf. Sys. Sc.*, Jan. 1972.
- [46] S. C. Kwatra, "Electrocardiogram via liquid media: Instrumentation and Signal Processing," Ph.D. Dissertation, University of South Florida, 1975.
- [47] K. W. Watkinson, "A study of ECG potentials on a laboratory torso model: prediction of heart location and orientation. Florida State University, 1971.

- [48] Nelson, C. V., Hodgkin, B. C., & Gastonguay, P. R. (1975). Dipole moment of the hearts of various species. *Annals of biomedical engineering*, 3(3), 308.
- [49] Nomura, M., Nakaya, Y., Miyoshi, Y., Wakatsuki, T., Saito, K., Bando, S., & Nakayasu, K. (1992). Single moving dipole obtained from magnetic field of the heart in patients with left ventricular hypertrophy. *Clinical cardiology*, 15(10), 752-758.
- [50] Terry, F. H., Brody, D. A., Eddlemon, C. O., Cox, J. W., Keller, F. W., & Phillips, H. A. (1971). Dipole, quadripole, and octapole measurements in isolated beating heart preparations. *IEEE Transactions on Biomedical Engineering*, (2), 139-148.
- [51] Fischmann, E. J., Barber, M. R., & Lehner, H. H. (1970). Effect of Torso Resistivity Variation on the Electrocardiograms of Children, Using a Grid Lead System. *Circulation*, 42(1), 171-179.
- [52] Haberkorn, W., Steinhoff, U., Burghoff, M., Kosch, O., Morguet, A., & Koch, H. (2006). Pseudo current density maps of electrophysiological heart, nerve or brain function and their physical basis. *Biomagnetic research and technology*, 4(1), 5.
- [53] Ellison, R. C., Fischmann, E. J., Miettinen, O. S., & Hugenholtz, P. G. (1969). Use of the dipole moment in the assessment of left ventricular hypertrophy. *Circulation*, 40(5), 719-730.
- [54] Burch, G. E., & Winsor, T. (1960). *A Primer of Electrocardiography*. Academic Medicine, 35(9), 889.
- [55] Pilkington, T. C., & Plonsey, R. (Eds.). (1982). *Engineering contributions to biophysical electrocardiography*. IEEE.
- [56] COMSOL, A. (2011). *COMSOL Multiphysics ver. 4.2 a*. [www.comsol.com](http://www.comsol.com). COMSOL AB, Stockholm, Sweden
- [57] Hyvärinen, A., & Oja, E. (2000). Independent component analysis: algorithms and applications. *Neural networks*, 13(4), 411-430.
- [58] Jain, V. K. (2006, May). Single cycle nonlinear VLSI cell for the ICA algorithm. In *Acoustics, Speech and Signal Processing, 2006. ICASSP 2006 Proceedings. 2006 IEEE International Conference on* (Vol. 3, pp. III-III). IEEE.
- [59] Jain, V. K., Bhanja, S., Chapman, G. H., Doddannagari, L., & Nguyen, N. (2005, March). A parallel architecture for the ICA algorithm: DSP plane of a 3-D heterogeneous sensor. In *Acoustics, Speech, and Signal Processing, 2005. Proceedings.(ICASSP'05). IEEE International Conference on* (Vol. 5, pp. v-77). IEEE.

- [60] Camargo-Olivares, J. L., Martín-Clemente, R., Hornillo-Mellado, S., Elena, M. M., & Román, I. (2011). The maternal abdominal ECG as input to MICA in the fetal ECG extraction problem. *IEEE Signal Processing Letters*, 18(3), 161-164.



## APPENDIX A: BACKGROUND AND LITERATURE REVIEW

### A.1. Heart and ECG

The heart is located in between the lungs in the chest. Its size is comparable to the size of a closed fist and weighs about 250 to 300 grams. The walls of the heart are composed of cardiac muscles called myocardium. It consists of four compartments: the left, and the right ventricles and auricles. The walls of the left ventricles and the septum are much thicker as compared to the right ventricles. Logically this is applicable as the left ventricles pump blood with higher pressure for systemic circulation, as compared to the pulmonary circulation which is done through the right ventricles. The heart has four valves. The mitral valve and tricuspid valve controls the flow of blood from the auricles to the ventricles, and the pulmonary valve and aortic valve controls the flow of blood out of the ventricles. A simple flow of the blood for systemic circulation and return is explained in the form of a block diagram in Fig. A.1

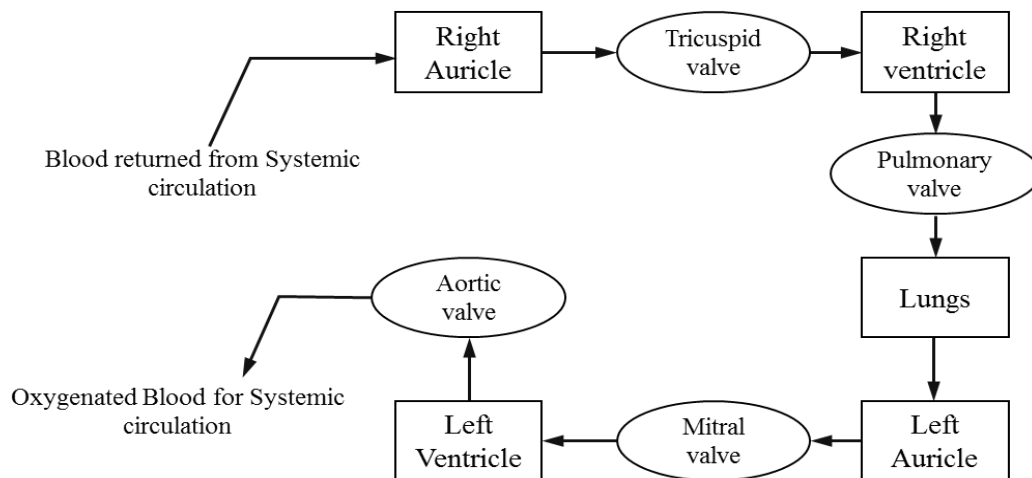


Figure A.1: Block diagram of systemic circulation

### A.1.1. Electrical Activity in the Heart

The cardiac electrical activity occurs just as like nerve cells due to the exchange of sodium ions across the membrane. The action potential is of the magnitude of 100 mV similar to the nerve cell the duration of the action impulse is around 300 ms. The Sinoatrial (SA) node is a crescent-shaped structure and is located in the right atrium. The SA node measures around 5 mm and 15 mm in height and length respectively. The cells of the SA nodes are called the pacemaker cells. These cells generate action potentials acting as a stimulus for the process of depolarization and repolarization of the heart. The other specialized node located in between the auricles and the ventricles is called as Atrioventricular (AV) node, and it is composed of a conduction system known as the bundle of his. The impulse generated at the SA node is transmitted through the bundle of his into the Purkinje fibers to the walls of the ventricles which mirrors the impulse by the SA node through contraction and relaxation of the heart for pumping the blood for systemic circulation. The conduction system of the heart is shown in Fig. A.2.

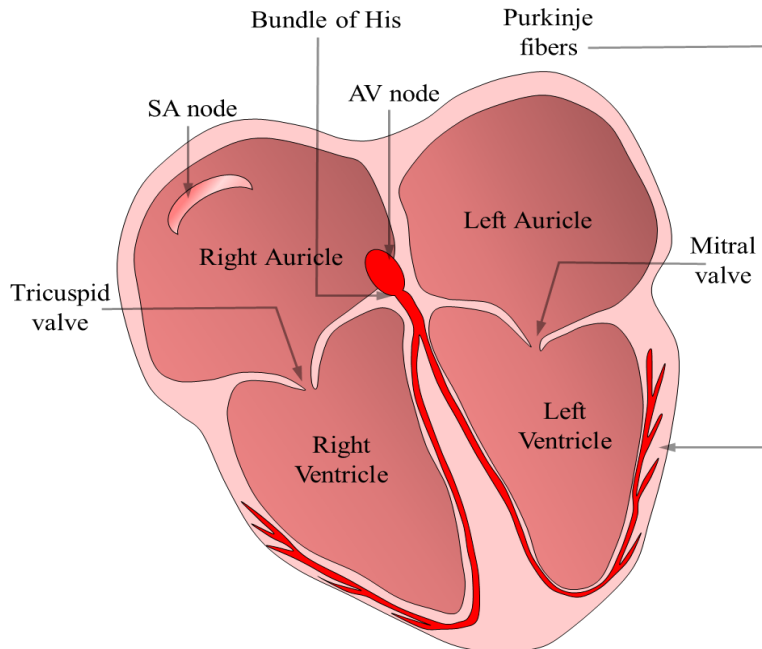


Figure A.2: Representation of the conduction system of the heart

Table A.1: Details of intrinsic frequencies of different heart locations

Location in Heart	Range of Intrinsic Frequency beats per minute
SA node	70-80
AV node	40-45
Bundle of His	25-40
Purkinje Fibers	25-40
Ventricular Fibers	25-30

The cardiac cells have the following properties

- 1) Rhythmicity: This property allows the cardiac cells to make the heart beat without any external stimulus. The nodal fibers and the conducting system in the heart are self-excitabile
- 2) Conductivity: The ability of the heart muscles to conduct the electrical impulses.
- 3) Excitability: The cardiac muscles will respond to stimuli.
- 4) Contraction: This is the result of the conduction of electrical impulses by the heart muscles.

In brief, one can say that the heart muscles while in rest will be polarized. With stimuli, the potential imbalance will cause a discharge leading to a depolarized cell. This results in contraction of the heart itself after which there will be a repolarization of the cell at a slower rate than the depolarization.

### **A.1.2. Path for Electrical Conduction in the Heart**

The flow of the impulse along the heart is explained in this section. The Fig. A.3 gives a general idea of the hearts conduction path. The electrical impulses travel from the SA node to the AV node. From the AV node (conduction velocity of 0.05 m/s) to the bundle of his (conduction velocity of 1.5 m/s). From the bundle of his to the Purkinje fibers (conduction velocity of 3.5 m/s).

The impulses on the Purkinje fibers directly activate the ventricles resulting in the contraction and thus results in the pumping of blood.

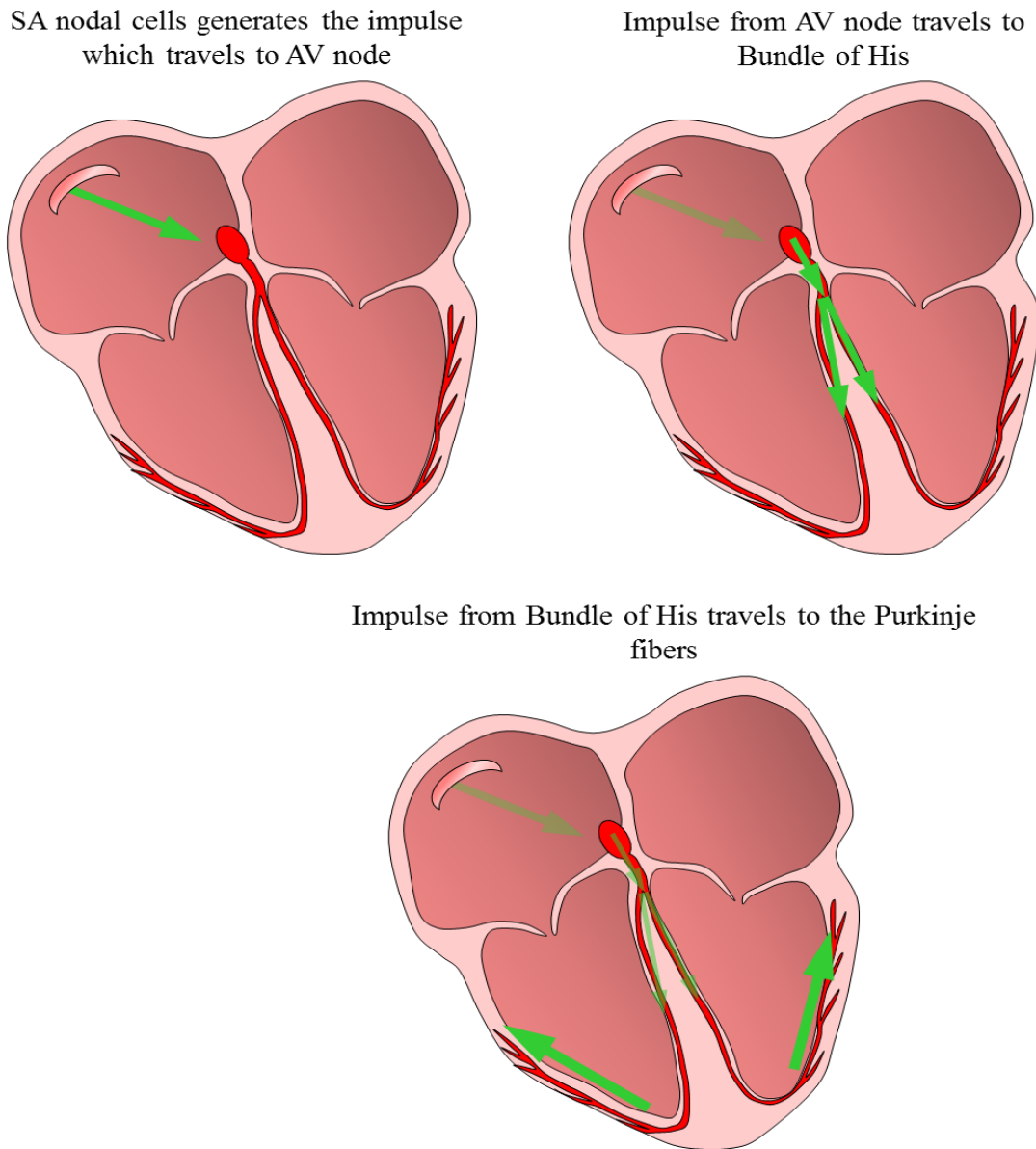


Figure A.3: Representation of the flow of impulse in the heart.

### A.1.3. A Note on Sinoatrial (SA) Node

The SA node has specialized cells called as pacemakers which generate electrical impulse acting as the required stimulus. The cells are of micrometer dimension. The SA node has an

intrinsic frequency of 75 beats per minute. Electrical double polarity layer exists in the SA node which generates the impulses. This can be approximated to a current dipole to represent the SA node mathematically. Since the electrical activity of the heart can be attributed to a current dipole, one can say that a heart vector exists which represents a time moving function of the electrical activity of the heart. More on the bioelectric sources has been covered in the subsection 2.2.

#### **A.1.4. A Note on Vector Representation of the Heart**

The heart vector is the relationship between the hearts current dipole moment and the potential that it produces at any point in or on the boundary of a medium. Significant research on this topic has been performed by Frank [2] but with assumptions required to explain the concept of the heart vector projection. The assumptions are (1) the human body is heterogeneous linear resistive electrical conducting medium, (2) the distribution of currents associated with electrical activation of heart muscles may be represented at each instant of time during the cardiac cycle by a single equivalent current dipole whose orientation and moment are variable and functions of the actual current distribution, and (3) the equivalent heart dipole remains fixed in position during the cardiac cycle.

A dipole vector can be used to represent the heart vector as

$$\vec{p} = p_x \vec{u}_x + p_y \vec{u}_y + p_z \vec{u}_z \quad (\text{A.1})$$

where  $p_x$ ,  $p_y$ ,  $p_z$  are the scalar components of the dipole moment vector and  $u_x$ ,  $u_y$ , and  $u_z$  are the unit vectors in the rectangular coordinate system. The potential at an arbitrary electrode lead  $i$  is given by,

$$V_i(t) = \langle \vec{a}_i \cdot \vec{p} \rangle = a_{ix} p_x(t) + a_{iy} p_y(t) + a_{iz} p_z(t) \quad (\text{A.2})$$

where,  $\vec{a}_i = a_{ix} \vec{u}_x + a_{iy} \vec{u}_y + a_{iz} \vec{u}_z$  is known as the lead vector which is dependent on the shape, size, characteristics of the medium, the position of the dipole and the location of the arbitrary point

of sampling. (2.2) is possible as a direct consequence of the assumed linearity of the medium. The components of the lead vector  $a$  are real as the medium is assumed to be resistive. The elements of the lead vector become linear constants which relate the electrode potential to the subject. The expression for bipolar leads can be given by the difference in two body potential lead points and can be expressed as,

$$V_{12}(t) = V_1(t) - V_2(t) = \vec{a}_1 \cdot p - \vec{a}_2 \cdot p \quad (\text{A.3a})$$

$$V_{12}(t) = (a_{x1} - a_{x2})p_x(t) + (a_{y1} - a_{y2})p_y(t) + (a_{z1} - a_{z2})p_z(t) \quad (\text{A.3b})$$

The concept of leads has been developed from the vector projection of the heart dipole.

### A.1.5. ECG Terminology

The ECG is recorded on paper with the scales of 1mm in horizontal and vertical axes representing 0.04 seconds and 0.1 mV respectively. The parts of the wave between deflections are called segments and the time between the beginning and end of a particular wave is called an interval. Electro Cardio Graph (ECG) is the cumulative sum of the different action impulse observed across different electrically active cardiac tissues. The standard definition for ECG can be as follows “ECG is the recording of the electrical potential generated due to the electrical activity of the heart upon the body surface.”

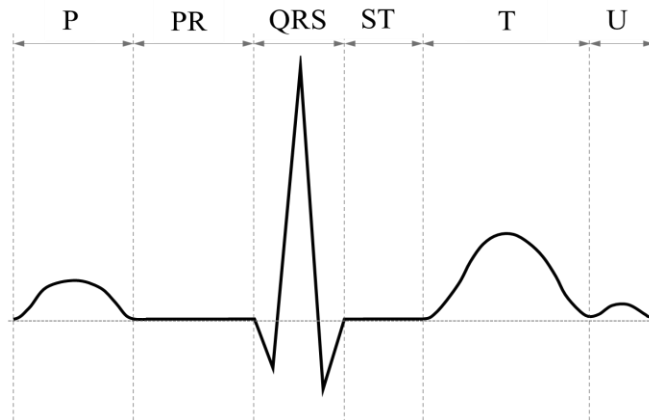


Figure A.4: ECG waveform having details of various wave periods

The potentials are caused by an electric field produced by regular contraction and relaxation of the heart. Potentials generated on the body surface can be measured using a set of electrodes positioned at specific locations on the body, a combination of these electrodes placed in a suitable way which can measure the potential variations in time is called a Lead. A standard ECG is as shown in the figure below. The core terminologies associated with a standard ECG waveform will be explained further.

Typically ECG of a cardiac cycle represented in Fig. 2.4 consists of a series of waves arbitrarily designed by Einthoven as the P-wave, the QRS complex, the T-wave and the U-wave. The P-wave is the result of auricular depolarization which can range between 5 to 85 ms. The P-R intervals are measured from the end of the P-wave to the beginning of the QRS complex; this wave represents the delay of the impulse from the SA node to the AV node. The QRS complex is the result of ventricular depolarization and can range between 110 to 120 ms; this consists of an initial downward deflection represented by the Q-wave, further upward deflection represented by the R-wave, and the downward deflection represented by the S-wave. The T-wave is the result of ventricular repolarization and can range between 400 to 450 ms. The U-wave is considered as an after potential and Experts in the field of ECG talk about the RR-interval, this is the time spanning between two peaks of an ECG waveform which is approximately 1 second. If we consider the subject as a conducting medium electrical impulses originating in the heart will cause body surface potential distribution on the upper torso of the subject. The magnitude and direction of propagation of this electrical impulse can be measured on the bioelectric source which has generated it; this topic has been covered in greater detail in Chapter 3 on “bioelectric sources.” Limb leads are used to measure the ECG, and a minimum set of 3 leads are required to measure the potentials generated

across the body. The limb leads are discussed briefly here to give the readers an idea about the minimal way through which ECG can be measured.

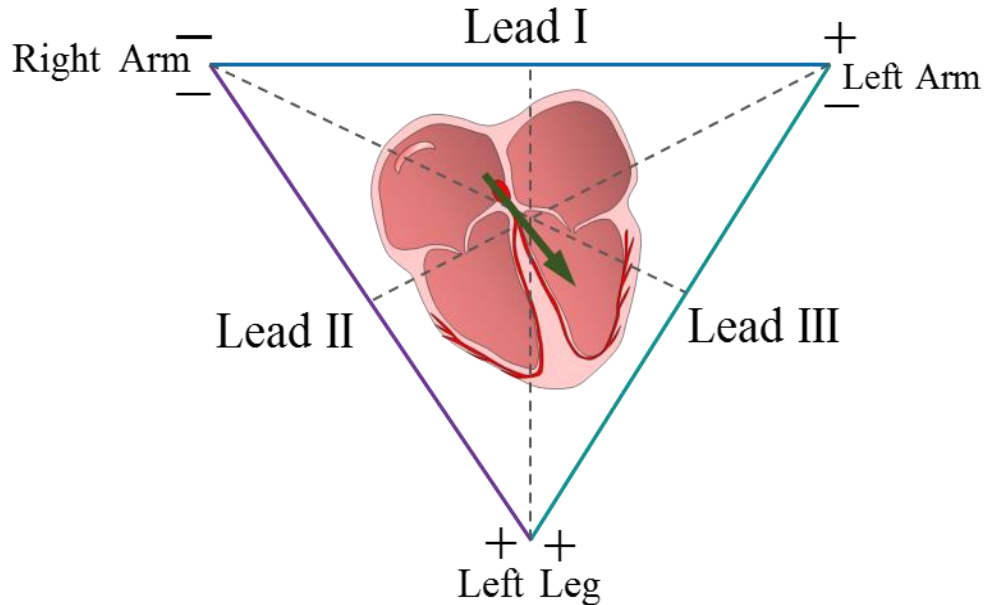


Figure A.5: Standard leads or limb leads.

Lead I corresponds to the electrodes that are attached to the right and the left arms of an individual, just above the wrists. The potential difference between these two points is recorded as Lead I of the ECG. Lead II corresponds to the electrodes that are attached to the right arm above the wrist and to the left leg just above the ankle to record the potential difference between these two points to contribute for Lead II of the ECG. Lead III corresponds to the electrodes that are attached to the left arm and the left leg, and the corresponding potential difference is measured as Lead III of the ECG. These three leads form the points of the Einthoven's Triangle. This is an equilateral triangle with the heart remaining at its center, and the summation of the voltage produced across the three leads will be zero. This is the most minimalistic set of electrode points which are used for the measurement of ECG Fig. A.5.



### A.1.6. Ventricular Depolarization for Generation of QRS Complex

The average of all the instantaneous mean heart dipole vectors occurring during the sequence of the ventricular depolarization is termed as the mean electrical axis. The QRS complex is produced during the depolarization of the ventricles. In Fig. A.6 a sequence of representation has been shown for the ventricular depolarization and the flow of electrical impulse. For convenience, just the septum and the ventricular walls will be explained. An electrical impulse is conducted through the branches of the bundle; this results in the depolarization of the septum, and the vector notation can be as in the first Q deflection shown in Fig. A.6.

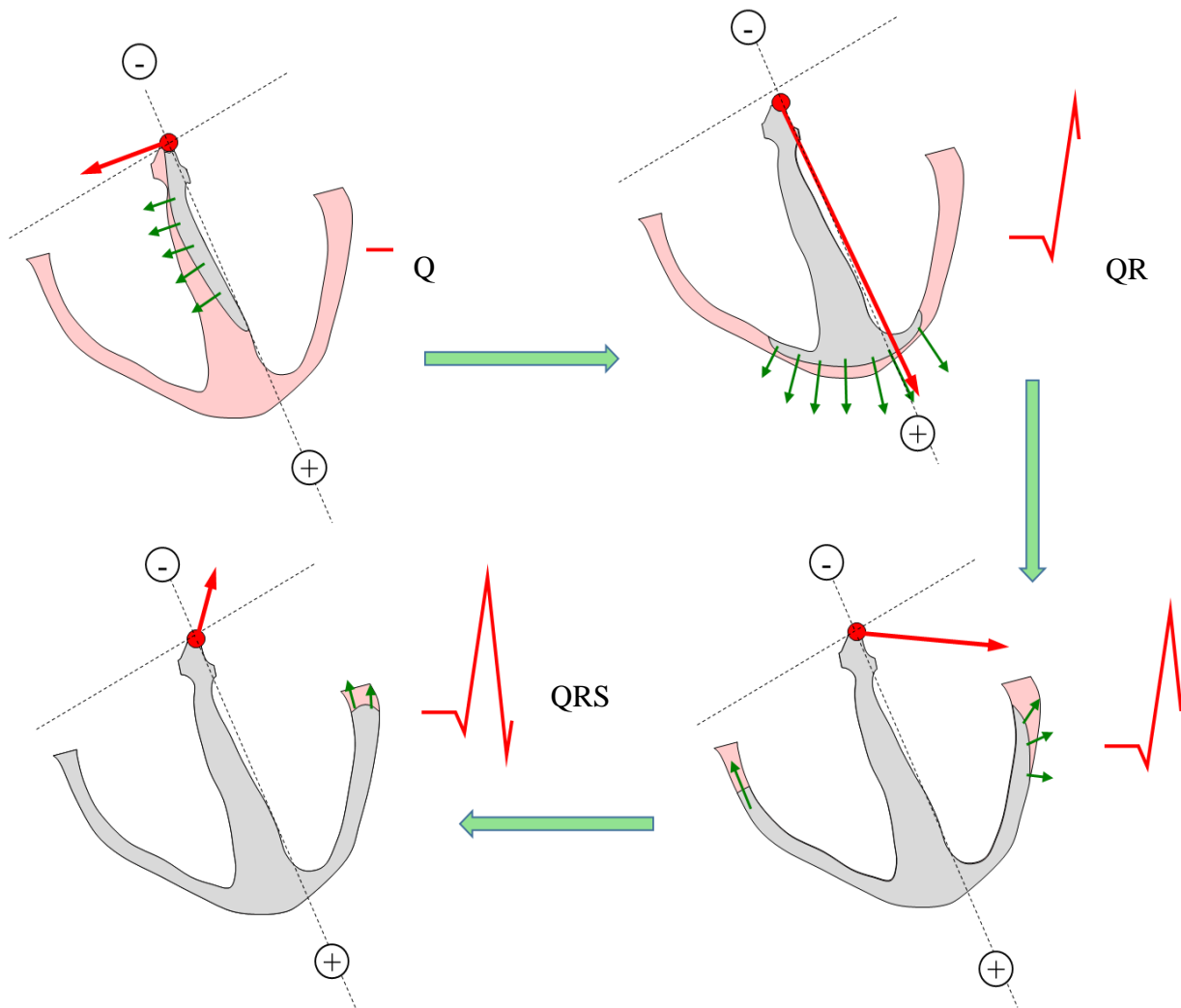


Figure A.6: QRS complex during ventricular depolarization

The heart vector is building up in a direction away from the positive electrode and thus results in a negative (Q-wave) deflection. After about 20 ms the mean vector points towards the apex and is oriented toward the positive electrode. This produces a very tall R wave. After yet another ~10 ms the mean vector points towards the left arm. This is recorded as a positive deflection. The last stage of the depolarization spread results in the S wave which is a slight negative deflection. A closing comment in this subsection would be that each limb lead sees a different type of mean heart vector based on the axial reference systems.

## A.2. Current Dipole Moments in Literature

Table A.2: Dipole moments (P) from literature

	Paper Title and first author's name	Dipole moment P (mA-cm)
1	Principles of Electrophysiology R. G. Mark	1e-3
2	Dipole Moment of the heart of various species C. V. Nelson	2320
3	Single moving dipole obtained from magnetic field of the heart in patients with left ventricular hypertrophy, M. Nomura	16550
4	Dipole, Quadripole, and Octapole measurements in isolated beating heart preparations, F. H. Terry	10
5	Effect of Torso Resistivity Variation on ECG of children using Grid lead system, E. J. Fischmann	1210
6	Pseudo current density maps of electrophysiological heart, nerve or brain function and their physical basis, W. Haberkorn	100
7	Use of the dipole moment in the assessment of left ventricular hypertrophy, R. C. Ellison	300 < P < 4300

## APPENDIX B: DIPOLE EXPERIMENTS IN COMSOL

### B.1. Model for Verifying Theoretical Concept in COMSOL

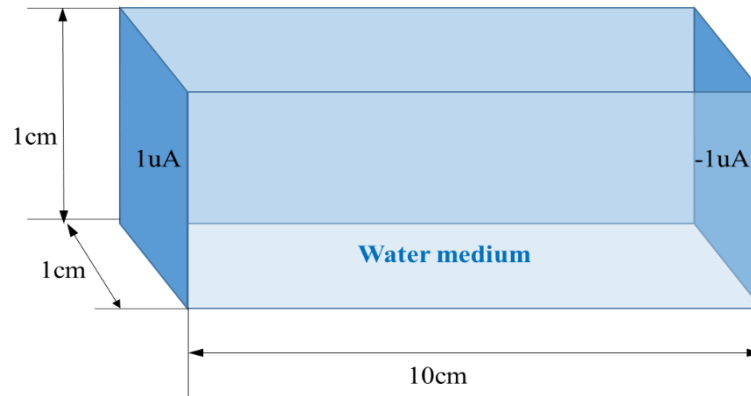


Figure B.1: Simple rectangular medium for validation of results from COMSOL

This research considers the conductivity of tap water to be 0.05 S/m and simple models were analyzed in COMSOL to confirm the theory. A cube of 10 cm x 1 cm x 1 cm was filled with water of conductivity 0.05 S/m, and a current of 0.1  $\mu$ A is passed through this medium. The calculations are as follows

The parameters given in the problem are

$$\sigma = 500 \mu\text{S/cm}; I = 0.1 * 10^{-6} \text{ A};$$

$$A = 1 \text{ cm}^2; L = 10 \text{ cm};$$

$$\text{wkt, } G = \sigma \frac{A}{L} = 500 * 10^{-6} * \left( \frac{1}{10} \right) = G = 0.5 * 10^{-4}$$

$$\text{Therefore, } R_{\text{medium}} = \frac{1}{G} = 2 * 10^4 \Omega$$

wkt,

$$V = I * R$$

$$V = 10^{-7} * 2 * 10^4$$

$$V = 2\text{mV}$$

The rectangular medium behaves as a resistor, and a total potential drop is 2 mV. The result from COMSOL is given in the Fig. B.2.

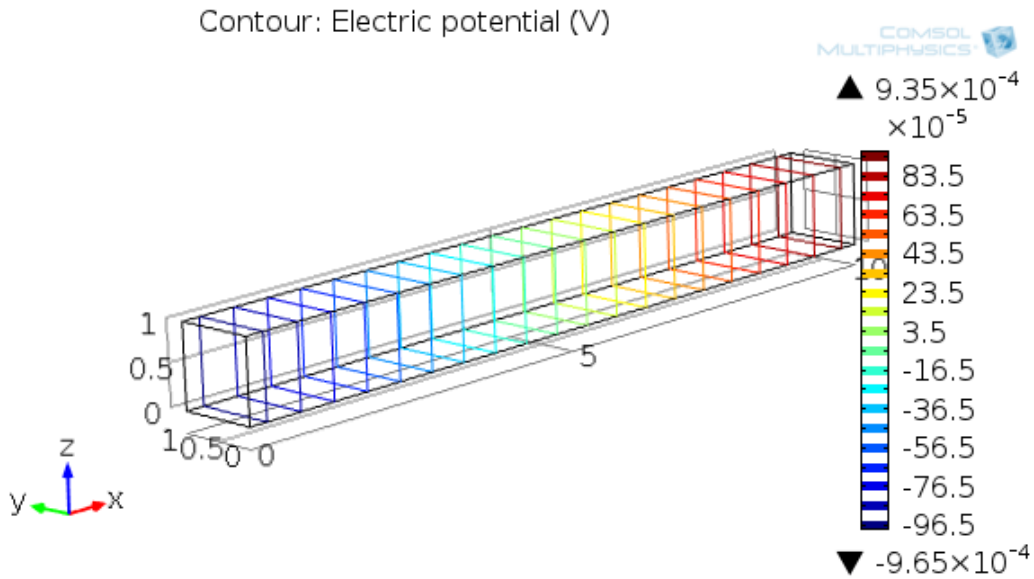


Figure B.2: COMSOL analysis of 10 x 1 x 1 cm rectangular medium

The voltage drop observed across the terminals of the rectangular medium was found to be ~2 mV. This confirms the result obtained by COMSOL model with the theoretical calculation.

## B.2. Different Types of Dipole Configuration

Dipoles can be created in many ways; this research creates dipoles in different orientations and COMSOL to analyze the results.

### B.2.1. Horizontal Dipole Model

It is assumed that the model can be built using a rectangular plastic container, with copper wires mounted horizontally, separated by a distance and which are exposed only at the ends as

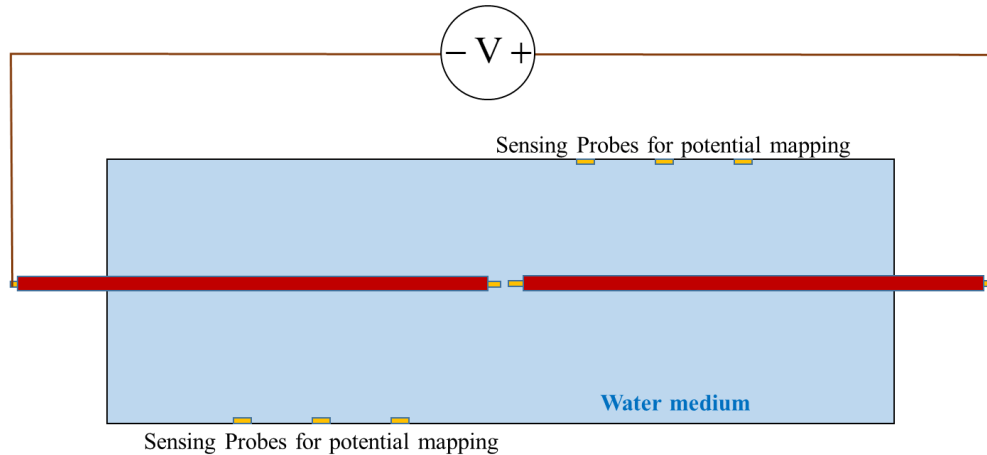


Figure B.3: Horizontal dipole configuration

shown in Fig. B.3. When a Voltage of equal magnitude but opposite polarities are applied across the ends of the two wires, a horizontal dipole is created. This dipole model can be analyzed using COMSOL, and the result of the analysis is discussed in this subsection.

A model similar to fig B.3. was constructed in COMSOL with the following dimensions 15 x 7 x 5 cm (L x B x H), and the boundary conditions were appropriately set to reflect the requirement of an insulated copper wire exposed (equal amounts) at the end. The separation between the two copper wires is 2 mm. The conductivity of the medium in which the dipole is placed is 0.05 S/m. The potential distribution which we can expect to be seen around a dipole was obtained from the analysis, and it can be as seen in Fig. B.4. Probes can be attached in COMSOL, and the distribution can be mapped. The results can be analyzed using MATLAB to find the orientation of the dipole present in the tank by measuring the potential distribution along the sidewalls of the tank. Therefore we can say that we have created a horizontal dipole which is oriented in the X-axis.

The horizontal dipole must be built with the following precautions,

- 1) The exposure of the copper on each wire should be the same, as an unequal exposure will not create a dipole (as dipole should have equal but opposite polarity source and sink)

2) Since copper poses a problem of electrolysis in water, the results of the potential distribution must be recorded quickly, and the water must be replenished with each experiment.

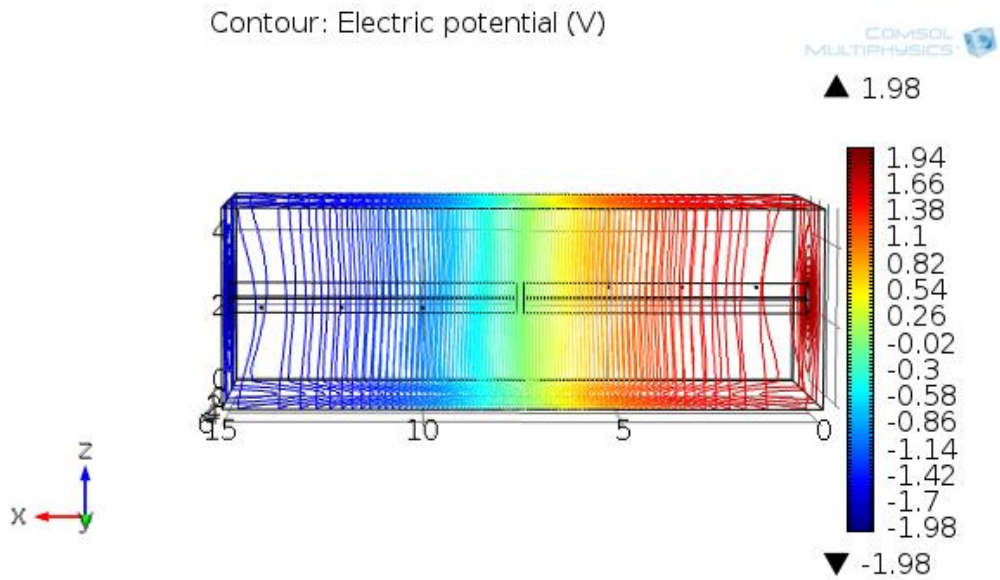


Figure B.4: Potential plot of horizontal dipole simulated in COMSOL

### B.2.2. Vertical Dipole Model

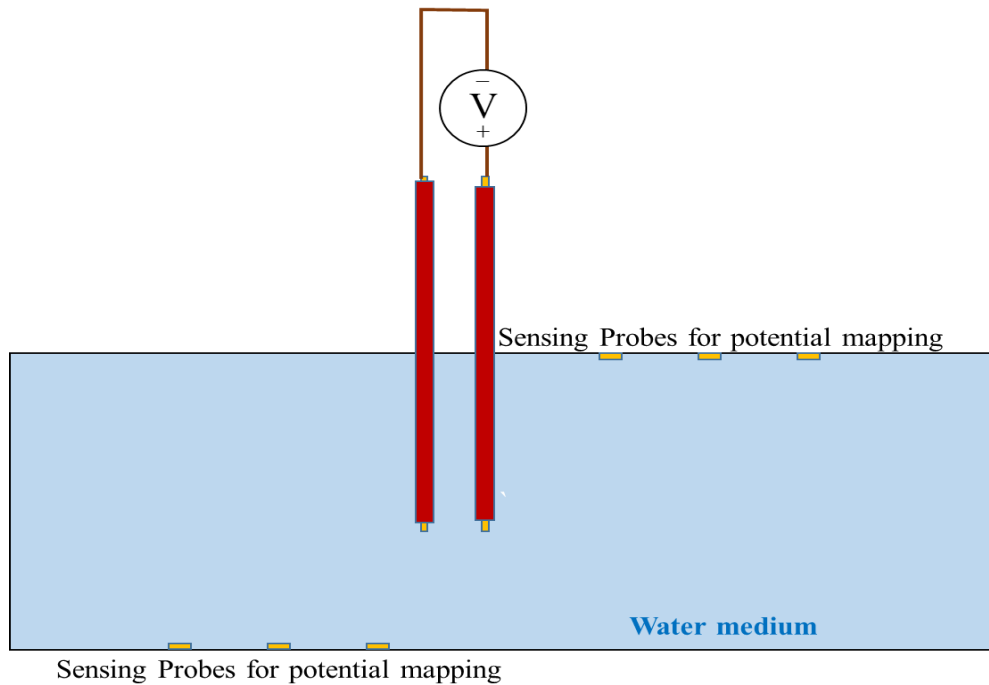


Figure B.5: Vertical dipole configuration

The vertical dipole is formed by placing the two copper wires (insulated throughout but open at the ends) vertically on the medium of dimensions 15 x 7 x 5 cm (L x B x H) separated by a distance of 2 mm from each other. The conductivity of the medium in which the dipole is placed is 0.05 S/m. The potential distribution plot for this configuration as shown in Fig. B.6.

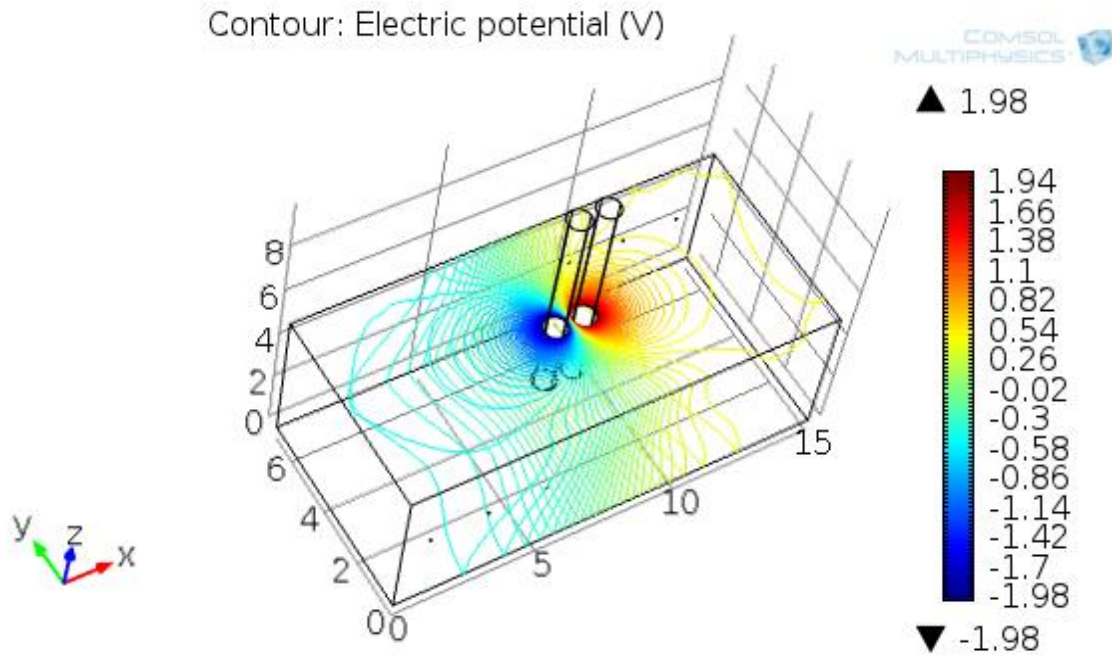


Figure B.6: Potential distribution due to the activity of a vertically oriented dipole

### B.2.3. Effect of the Medium Size on the Potential Distribution Pattern

The medium under consideration is having the dimensions of 15 x 7 x 5 cm as its length, breadth, and height respectively. The effect of the dimensions of the medium on the activity of the dipole can be analyzed using Fig. B.7. through Fig. B.10. It can be inferred from the images that the potential distribution for the horizontal configuration of the dipole is more prominent as compared to the vertical configuration of the dipole. The parameters of analysis used in COMSOL for calculating the potential distribution patterns for both the case is almost the same. However one has to note the following effects of the medium

- 1) The dipoles activity will be profoundly noticed if it is oriented along the largest dimension of the medium. The contrary statement is true as well, that is, if the orientation of the dipole is any other axis apart from the longest dimensions of the medium the effect of that particular dipole activity will be less in the medium.

A concluding note, instead of using copper wires, we can create dipoles using copper plates as well. However, the copper plates used for the two monopoles should be exactly of the same dimensions and same electrical configuration, if not the dipole effect will not be created when individual copper plates are energized. This will be further explained in the following subsection.

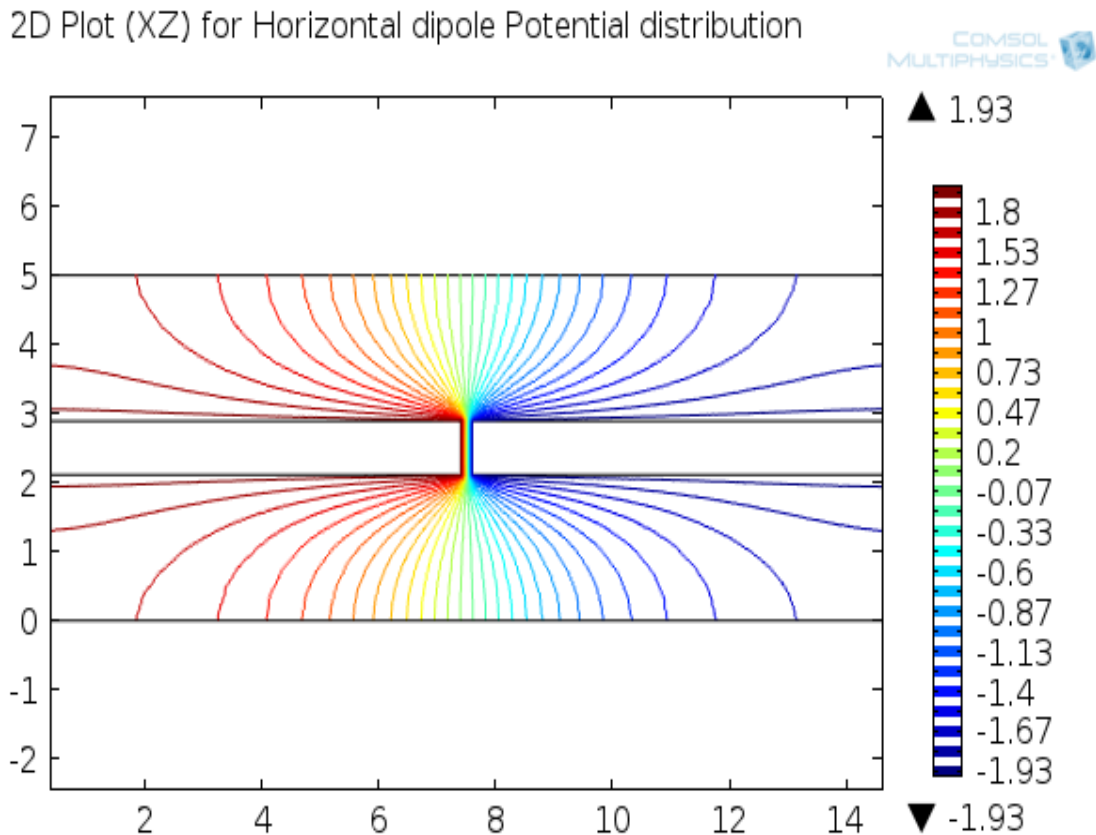


Figure B.7: The potential distribution pattern (XZ) noticed for a dipole oriented in X-direction (horizontally) along the length of the medium (where  $L > B > H$ )



2D Plot (XY) for Horizontal dipole Potential distribution

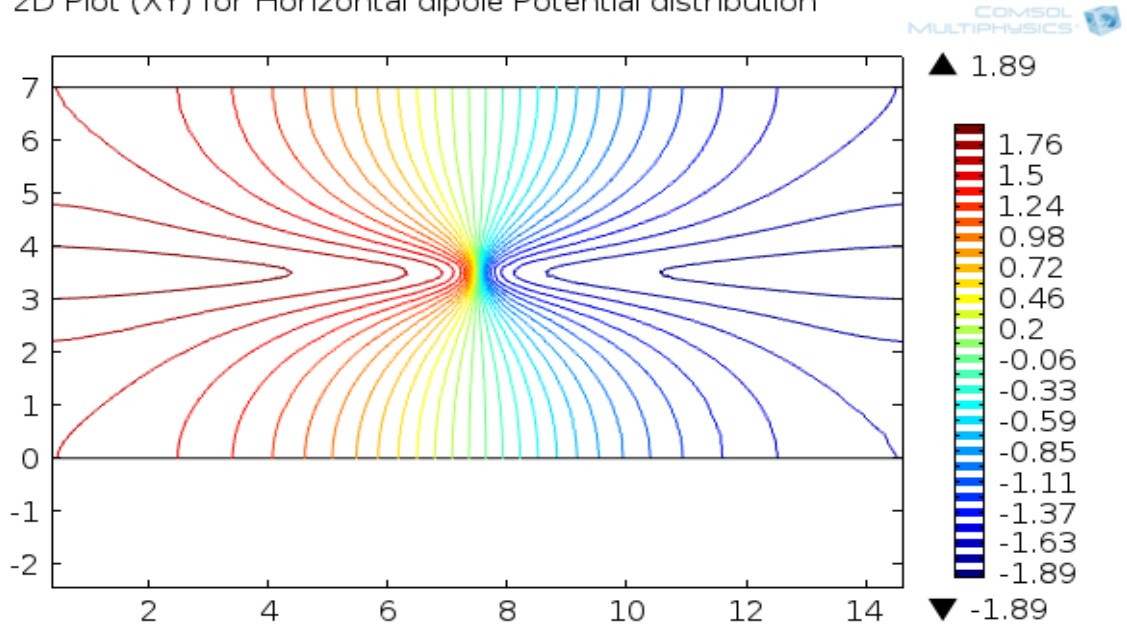


Figure B.8: The potential distribution pattern (XY) noticed for a dipole oriented in X-direction (horizontally) along the length of the medium (where  $L > B > H$ )

2D Plot(XY) for Vertical dipole Potential distribution

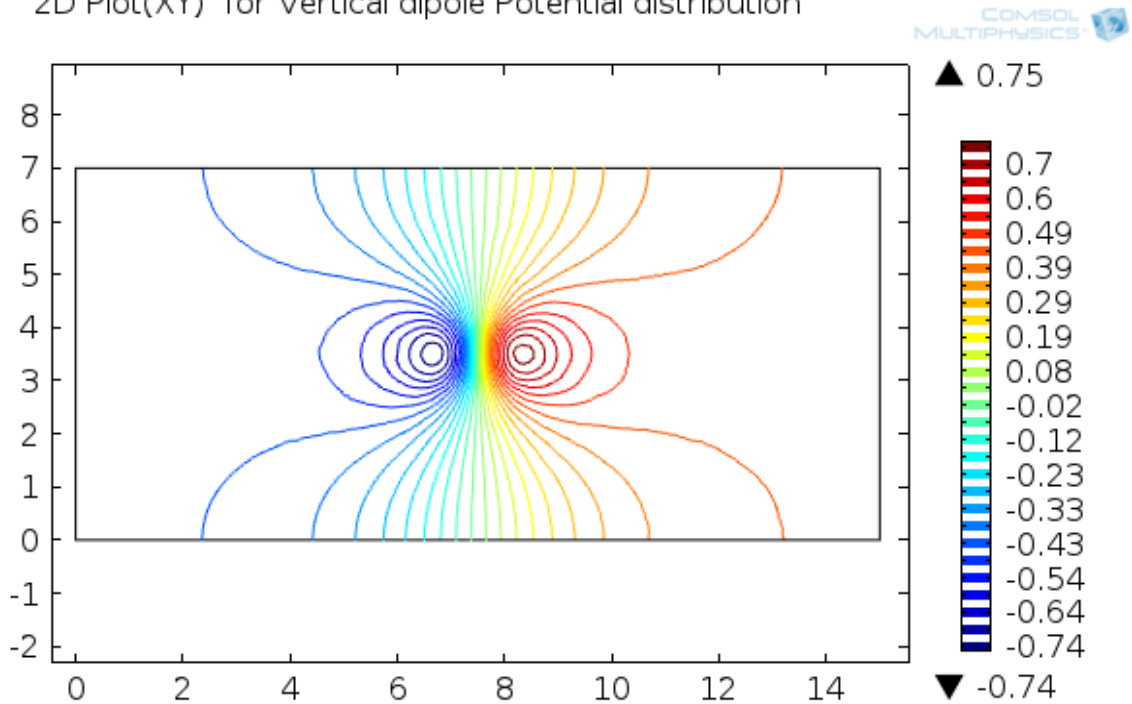


Figure B.9: The potential distribution pattern (XY) noticed for a dipole oriented in Z-direction (vertically) along the height of the medium (where  $H < B < L$ )

2D Plot(XZ) for Vertical dipole Potential distribution

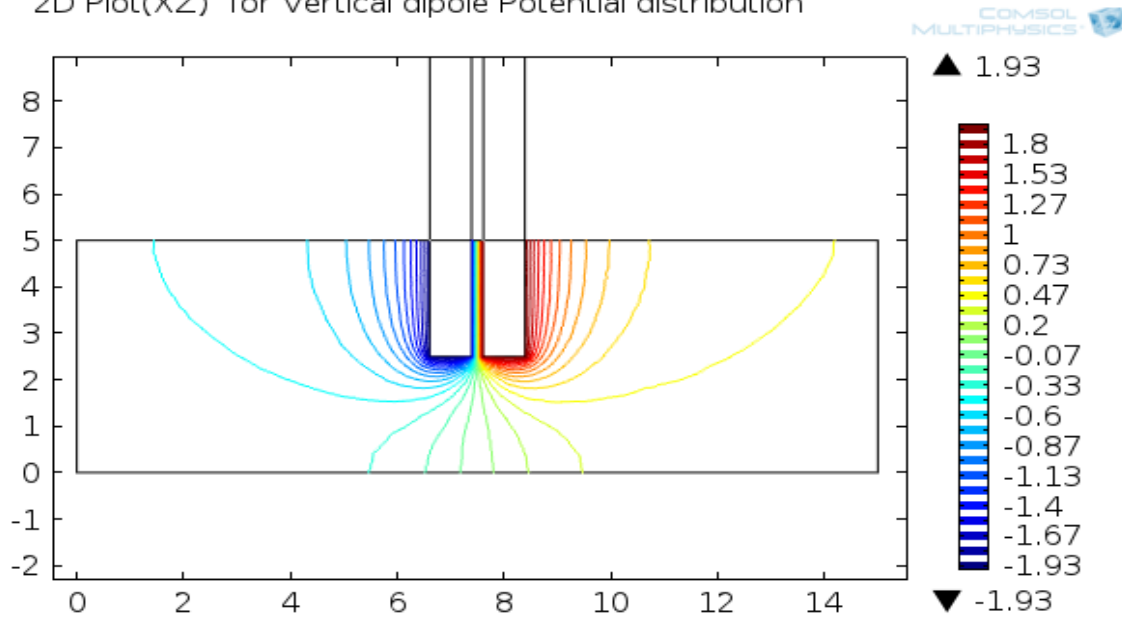


Figure B.10: The potential distribution pattern (XZ) noticed for a dipole oriented in Z-direction (vertically) along the height of the medium (where  $H < B < L$ )

### B.3. Dipole Model Using Small Copper Plates

A dipole can be built using a copper plate of small dimensions as shown in Fig. B.11. A copper plate of  $1 \times 1 \times 0.06$  cm is used. These plates are separated by a distance of 2 mm and placed almost in the center of the medium. The conductivity of the medium in which the dipole is placed is  $0.05$  S/m, and the dimensions of the medium are  $15 \times 7 \times 5$  cm. The potential distribution can be mapped using the sensing probes attached to the inner wall of the medium as shown, E1 to E6. The two copper monopoles are represented by M1 and M2. The potential distribution of this configuration is shown in Fig. B.12 The effect of E1 and E6 with the monopole size variation will be given in table.B.1. It is clearly seen that the effect of the monopole variation is clearly distorting the potential distribution in the medium with changes in the size of the monopole using the potential sensed across end probes.

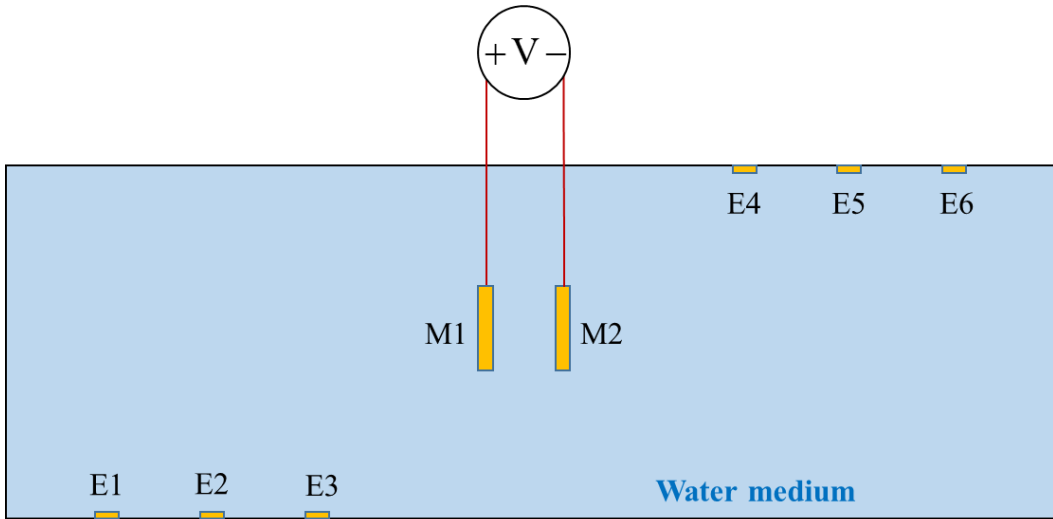


Figure B.11: Dipole created using tiny copper plates

The 2D potential map of the case with equal sized monopoles is given in Fig. B.12 medium. With this, the following conclusions can be made, that the potential distribution in any medium of irregular shape containing a dipole will depend on the orientation and field strength of the monopoles.

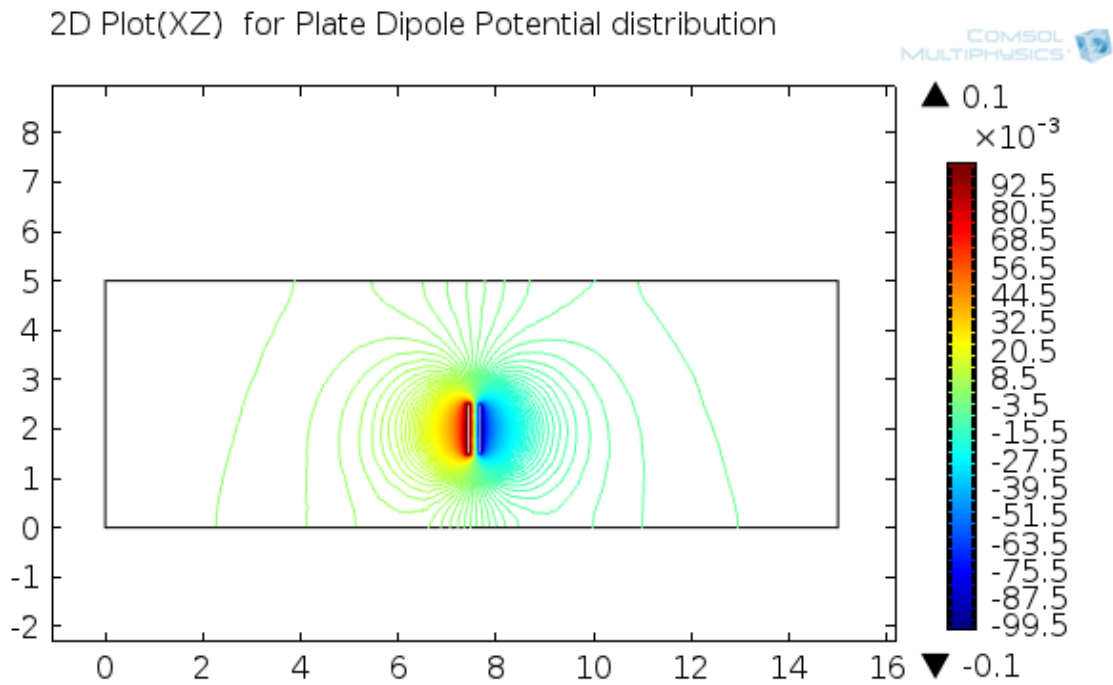


Figure B.12: 2D potential map of dipole created using copper plates

Table B.1: Effect of monopole size on the potential distribution around the medium

Monopole Size in cm		Applied potential	Potential recorded by	
M1	M2		E1	E6
1 x 1 x 0.06	1 x 1 x 0.06	$\pm 100$ mV	2.6 mV	-3.1 mV
1 x 1 x 0.06	1.1 x 1.1 x 0.06	$\pm 100$ mV	$\sim 0$	-6.3 mV
1 x 1 x 0.06	1.2 x 1.2 x 0.06	$\pm 100$ mV	-1.8 mV	-6 mV
1 x 1 x 0.06	1 x 1.2 x 0.06	$\pm 100$ mV	$\sim 0$	-6 mV
1 x 1 x 0.06	1.3 x 1.3 x 0.06	$\pm 100$ mV	-1.6 mV	-3.5 mV

#### B.4. Potential Distributions for Bathtub Ellipsoid Models

Potential distribution caused by the activity of 3D-CD in the bathtub is as shown in Fig. B.13. and Fig. B.14.

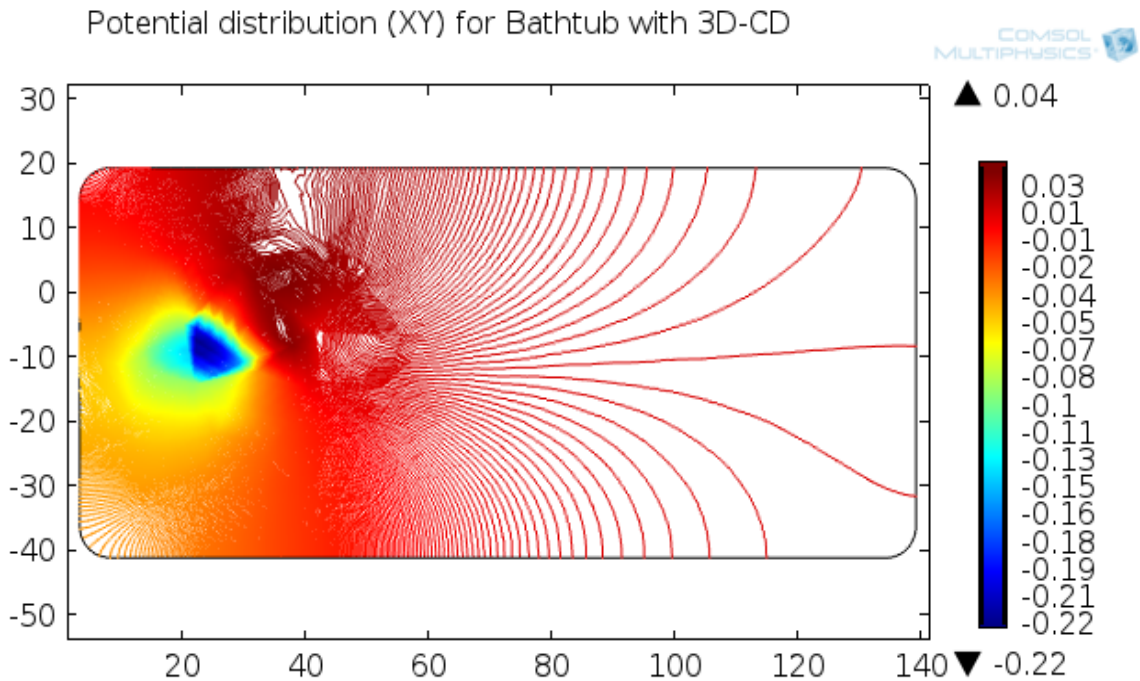


Figure B.13: Potential distributions caused by the activity of 3D-CD in a bathtub containing tap water; XY view

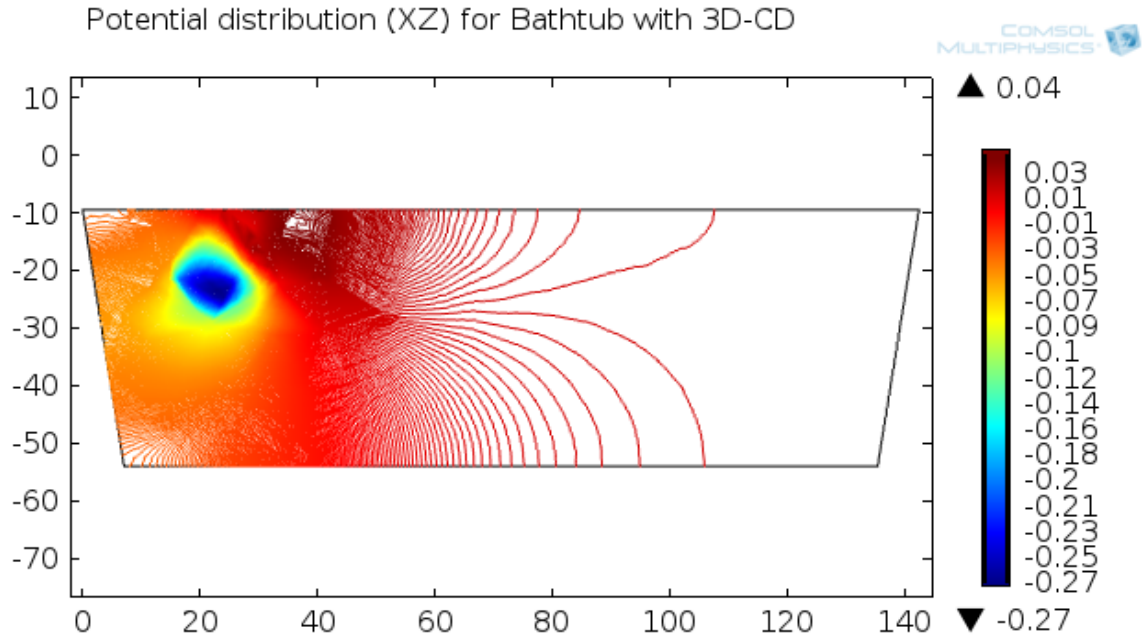


Figure B.14: Potential distributions caused by the activity of 3D-CD in a bathtub containing tap water; XZ view

Potential distribution of 3D-CD in the bathtub with single ellipsoidal phantom is shown in Fig. B.15. and Fig. B.16.

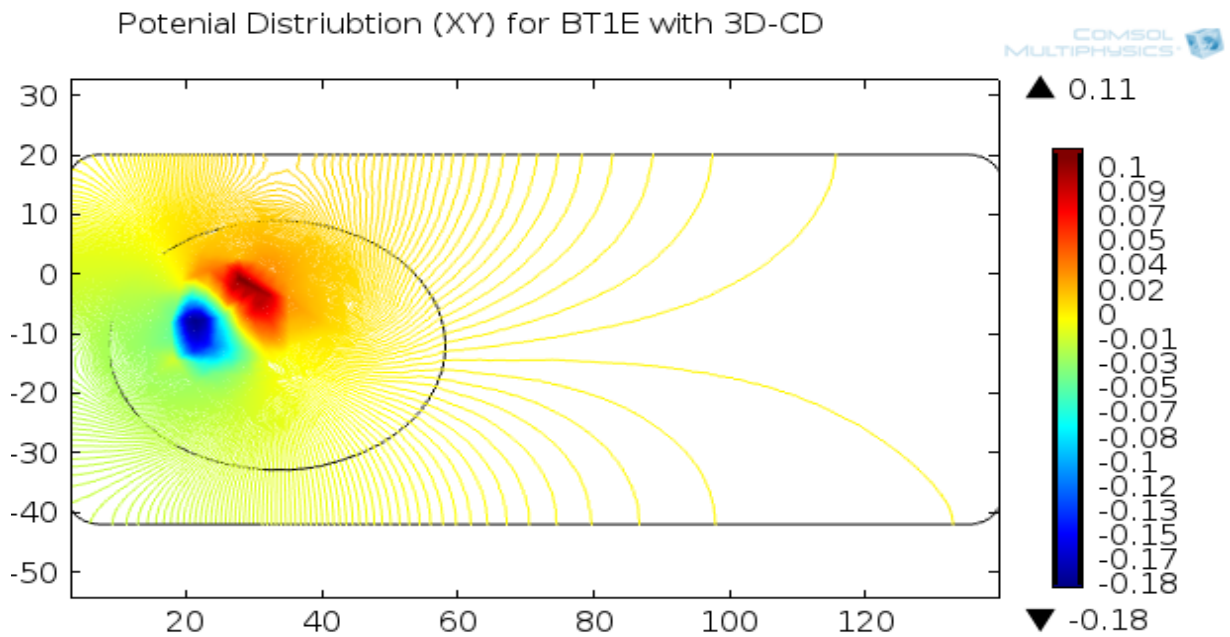


Figure B.15: Potential distribution caused by the activity of 3D-CD inside single ellipsoidal phantom placed in a bathtub containing water; XY view

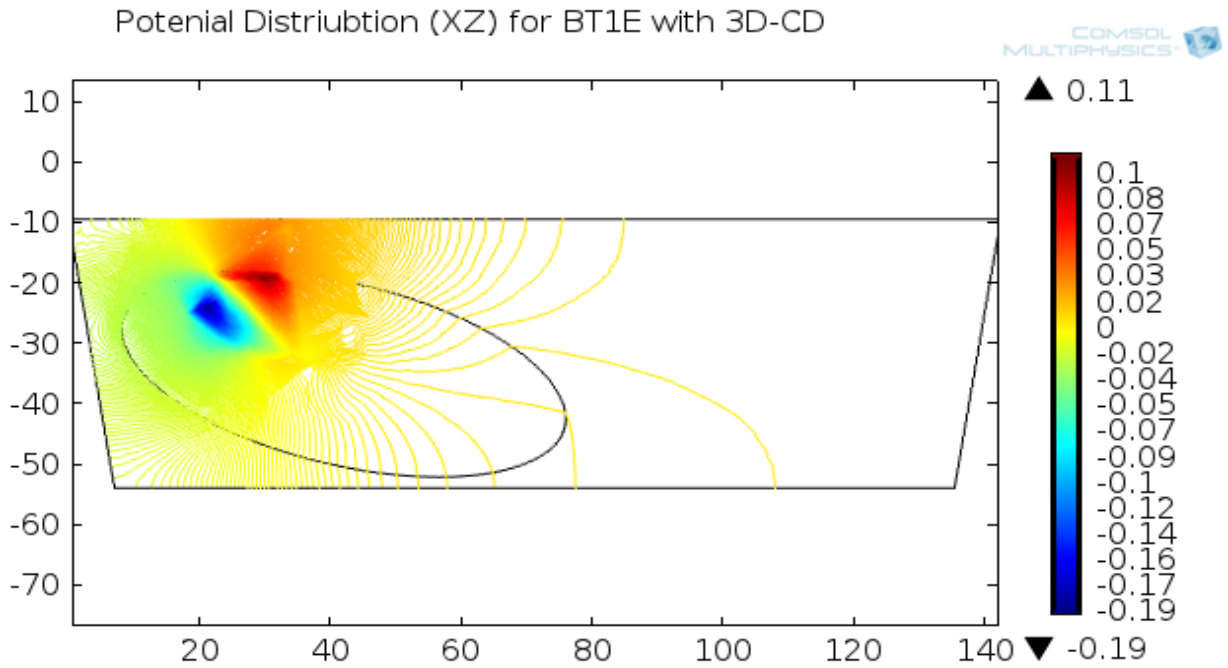


Figure B.16: Potential distribution caused by the activity of 3D-CD inside single ellipsoidal phantom placed in a bathtub containing water; XZ view

Potential distribution caused by two 3D-CD inside double ellipsoidal phantoms laying in a bathtub filled with tap water is shown in Fig. B.17. and Fig. B.18.

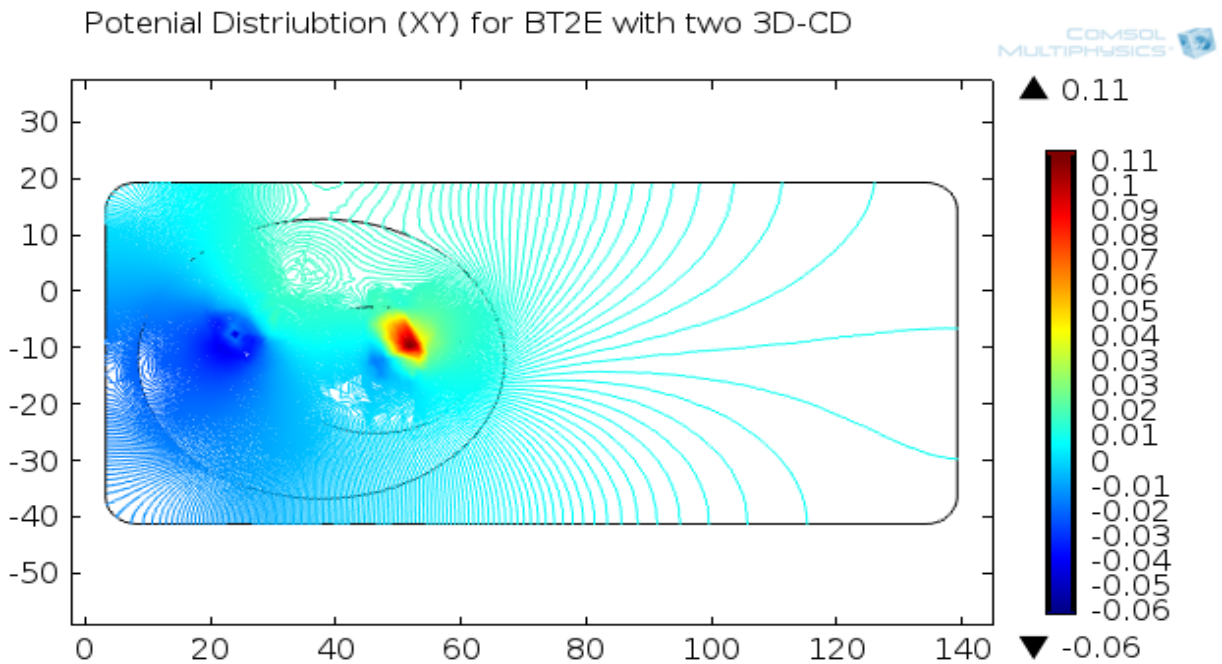


Figure B.17: Potential distribution caused by two 3D-CDs inside a double ellipsoidal phantom laying in the bathtub filled with tap water; XY view

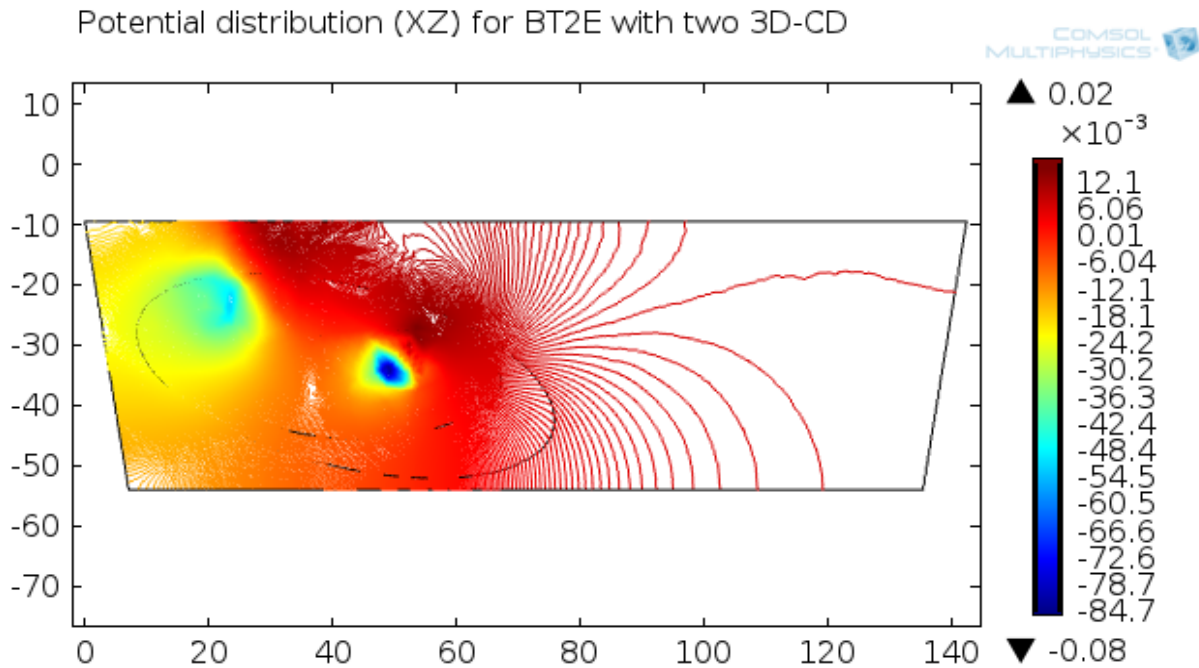


Figure B.18: Potential distribution caused by two 3D-CDs inside a double ellipsoidal phantom laying in the bathtub filled with tap water; XZ view

## B.5. Effect of the Torso Geometry on the Potential Distribution in a Medium

The effect of the torso geometry inside a medium of specific conductivity with the dipole location and the medium dimensions are to be considered during any analysis. Therefore, a summary of COMSOL analysis of the different conditions are shown and the results are tabulated.

### B.5.1. Cuboidal Medium with Eccentric Dipoles in Varying Torso Shapes

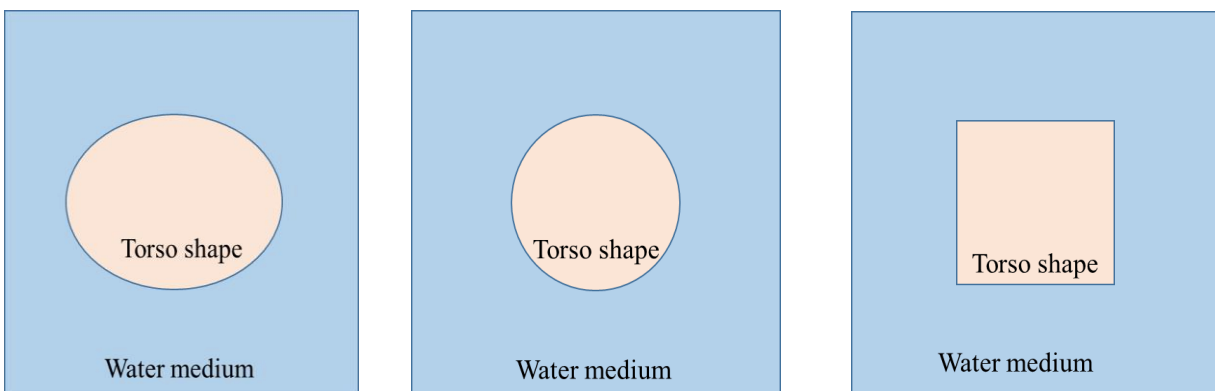


Figure B.19: Cuboidal medium containing different torso shapes

For simplicity, only 2D top view of the medium with different torso shapes are shown in Fig. B.19. There are two different subcases which pertain to the location of the dipole inside the medium, and they are tabulated as in table B.2 and table. B.3.

Table B.2: Effect of dipole located at the center inside different torso shapes in a cuboidal medium

Type of Boundary	E1	E2	NRMSE E1	NRMSE E2
Spheroid	-1.53892	1.759	10.3%	7.9%
Cuboid	-1.5889	1.85291	7.3%	13.7%
Cylindrical	-1.77951	1.84167	3.8%	13%
Ellipsoid	-1.71457	1.62946	(Reference)	

Table B.3: Effect of dipole located at an eccentric point inside different torso shapes in a cuboidal medium

Type of Boundary	E1	E2	NRMSE E1	NRMSE E2
Spheroid	-1.64775	1.45992	1.9%	0.6%
Cuboid	-1.49155	1.73975	11.2%	18.5%
Cylindrical	-1.66846	1.72877	0.7%	17.7%
Ellipsoid	-1.67994	1.46832	(Reference)	

The tabulated results consider that the ellipsoid is the best approximation for a human torso and is compared with different shapes and its effect on the two sensing probes located on opposite walls of the medium are analyzed. The tabulated result shows that with a maximum error of 19% one can deviate from the approximation of ellipsoidal representation of the human torso.

### **B.5.2. Rectangular Medium with Dipoles in Varying Torso Shapes**

For simplicity, only 2D top view of the medium with different torso shapes are shown in Fig. B.20.



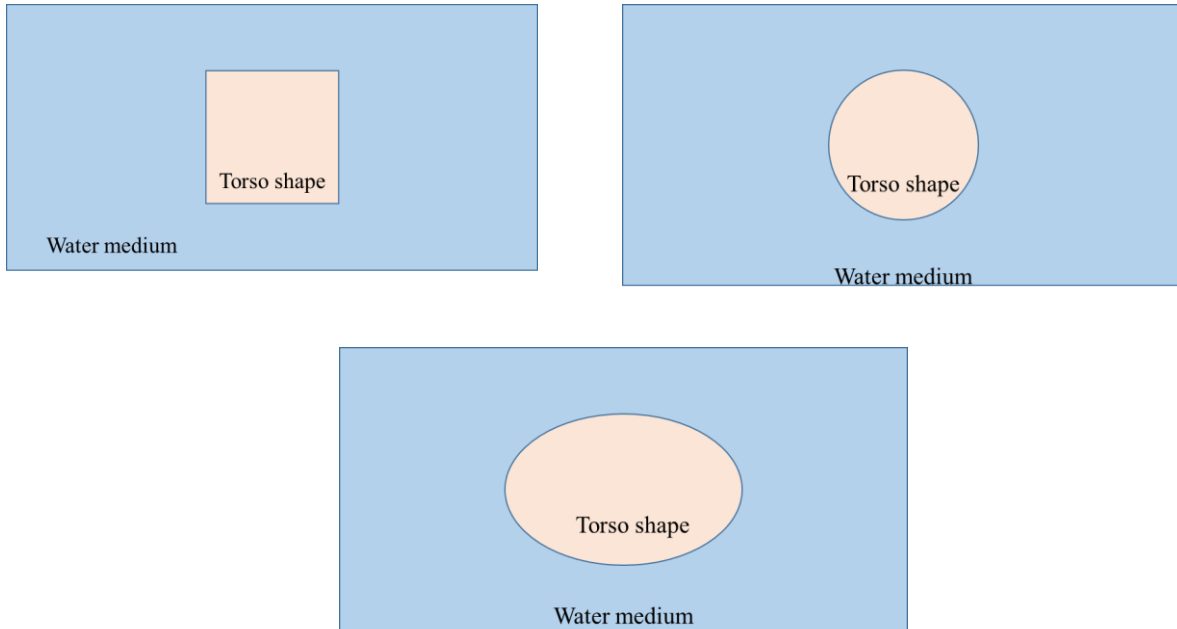


Figure B.20: Rectangular medium with dipole at different locations inside different torso shapes

Table B.4: Effect of dipole located at the center inside different torso shapes in a rectangular medium

Type of Boundary	E1	E2	NRMSE E1	NRMSE E2
Spheroid	-1.283	1.03647	9.4%	10.2%
Cuboid	-1.22048	1.16769	4.1%	1.2%
Cylindrical	-1.36217	1.07527	16.2%	6.8%
Ellipsoid	-1.17261	1.15372	(Reference)	

There are two different subcases which pertain to the location of the dipole inside the medium, and they are tabulated in table B.4 and table. B.5.

The tabulated results consider that the ellipsoid is the best approximation for a human torso and is compared with different shapes and its effect on the two sensing probes located on opposite

walls of the medium are analyzed. The tabulated result shows that with a maximum error of 20% one can deviate from the approximation of ellipsoidal representation of the human torso.

Table B.5: Effect of dipole located at an eccentric point inside different torso shapes in a rectangular medium

Type of Boundary	E1	E2	NRMSE E1	NRMSE E2
Spheroid	-0.85371	1.42966	20%	15.3%
Cuboid	-0.95903	1.24112	10.1%	0.13%
Cylindrical	-0.9948	1.47054	6.7%	18.7%
Ellipsoid	-1.0667	1.23939	(Reference)	

### B.6. COMSOL Procedural Steps in the Context of this Research

The steps described below pertain to COMSOL 4.2a software licensed for AC/DC module.

General Steps which can be followed for any project are detailed below

- Selection of the dimension in which the problem requires to be solved

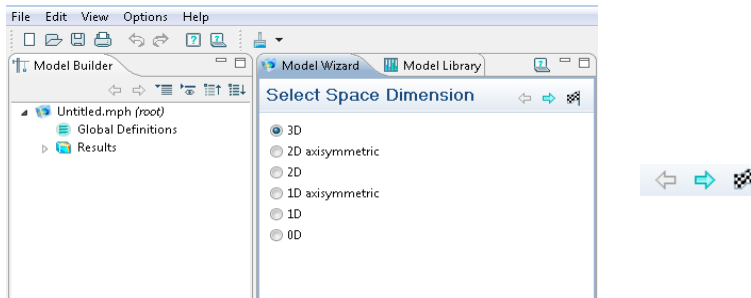


Figure B.21: Selection of dimension of workspace

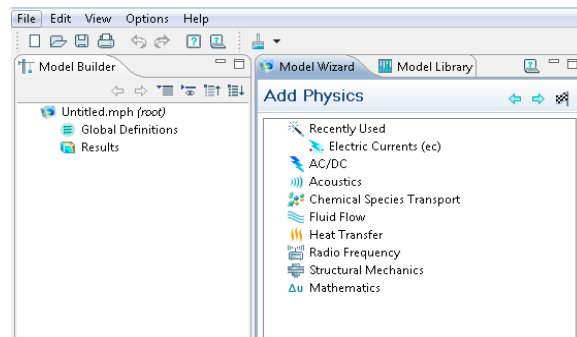


Figure B.22: Selection of the appropriate physics

- Selecting the appropriate physics applicable to the problem at hand. In this research, AC/DC module and Electric current submodule is used,
- Selecting the right type of study for solving the problem

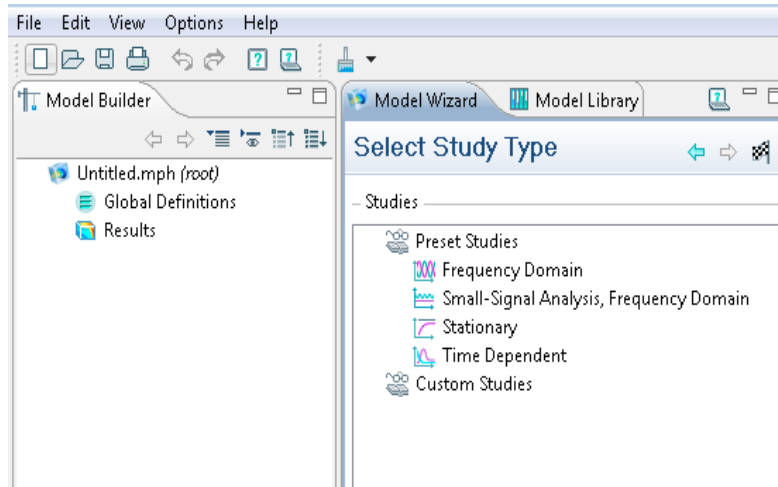


Figure B.23: Selection of study type

In this research, the stationary or time dependent analysis has to be chosen to obtain the required results. These 3 steps are a common procedure before starting any new projects.

### B.6.1. Research Problem

To observe the time varying potentials along the inner surface of a liquid medium by adding two ellipsoidal phantoms containing a vector dipoles (3D-current-dipoles). To create all the models in COMSOL, for this illustration a trapezoidal shaped medium will be considered to resemble the dimensions of a bathtub and two ellipsoidal phantoms whose dimensions reflect an adult torso and a fetus with two vector dipoles at eccentric positions are used. To start a new simulation select the new simulation icon located at the top left corner as shown in Fig. B.24.



Figure B.24: Icon for starting a new simulation

When the Model Wizard opens, the space dimensions has to be selected as 3D followed by the blue forward arrow.



Figure B.25: Workspace selection

In Add Physics window, the AC/DC module has to be expanded, and the Electric Currents submodule has to be selected followed by the blue forward arrow.

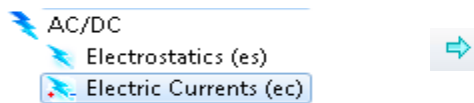


Figure B.26: Selection of physics for solving the problem

In select study type window, click to select the Time-dependent type of study and click on finish.

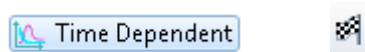


Figure B.27: Selection of study type

In the geometry window 'cm' should be selected as the unit for the model. The ellipsoid is built by navigating to model builder→ geometry→ more primitives and select the option of ellipsoid. In the ellipsoid settings specify the length of the semi-axes to be half the original torso

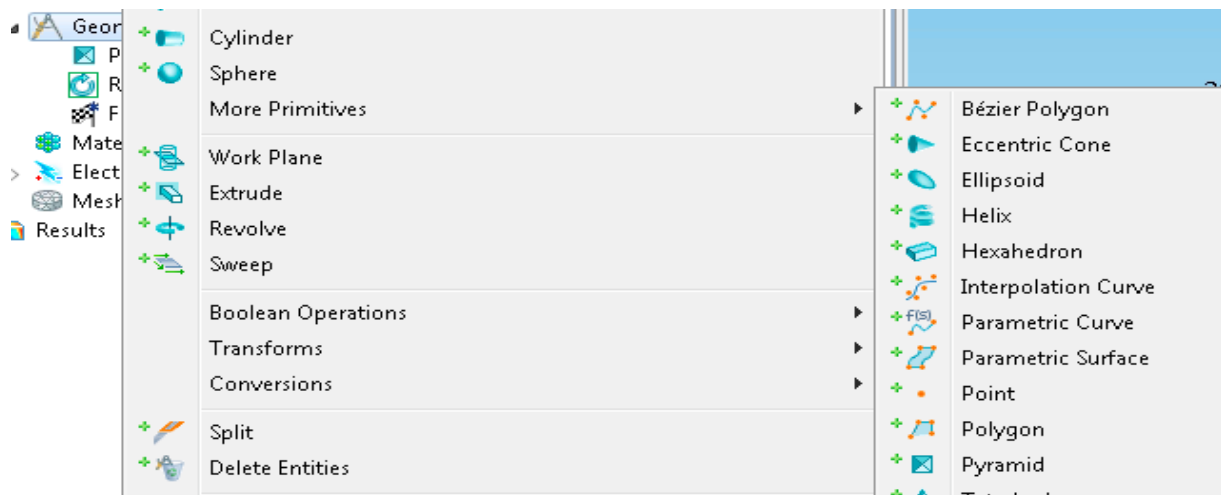


Figure B.28: Option for selection of an ellipsoid

dimensions. Therefore, add  $a = 40$  cm,  $b = 25$  cm,  $c = 15$  cm with  $z$  coordinate of  $-20$  cm and select the option to build all geometry an ellipsoid will be built as shown in Fig. B.29.

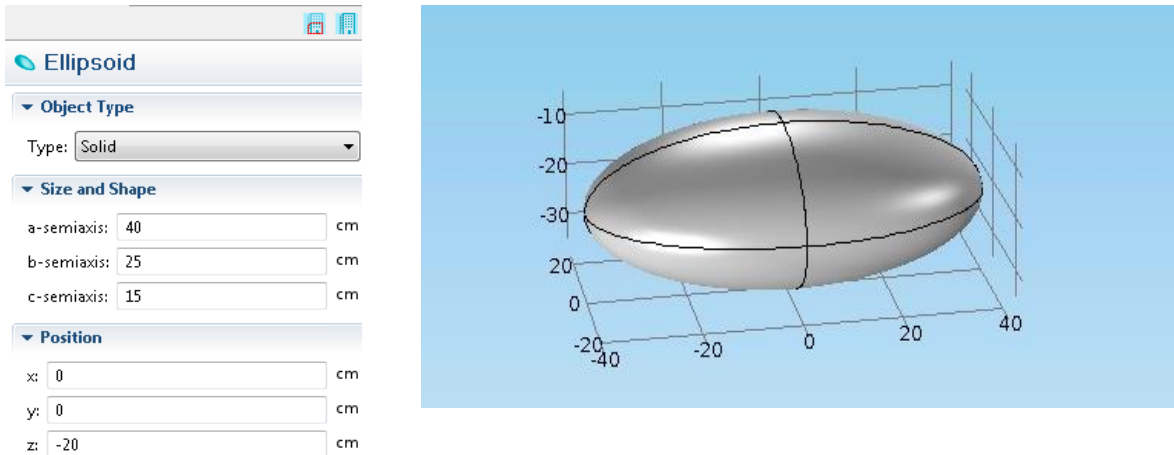


Figure B.29: Ellipsoid dimensions on the left and the model built is shown on the right

The next step will be to define the boundary for the ellipsoid by navigating to definitions → selections → Explicit and selecting the ellipsoid as the input to the ‘explicit1’ domain condition.

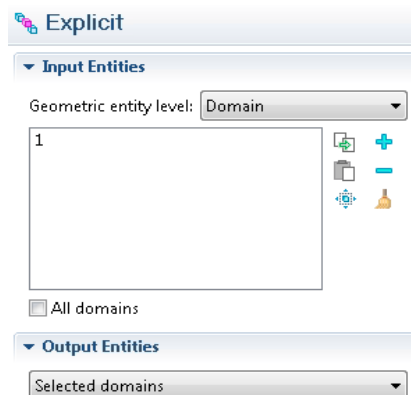


Figure B.30: Details on explicitly selecting the ellipsoid

Navigate to geometry1 → transforms → rotate option to give a tilt to the ellipsoid (representing a torso in the water medium). The input object should be selected as the ellipsoid, and a 15-degree tilt in  $y$  and  $z$ -direction has to be provided as shown in the Fig. B.30.

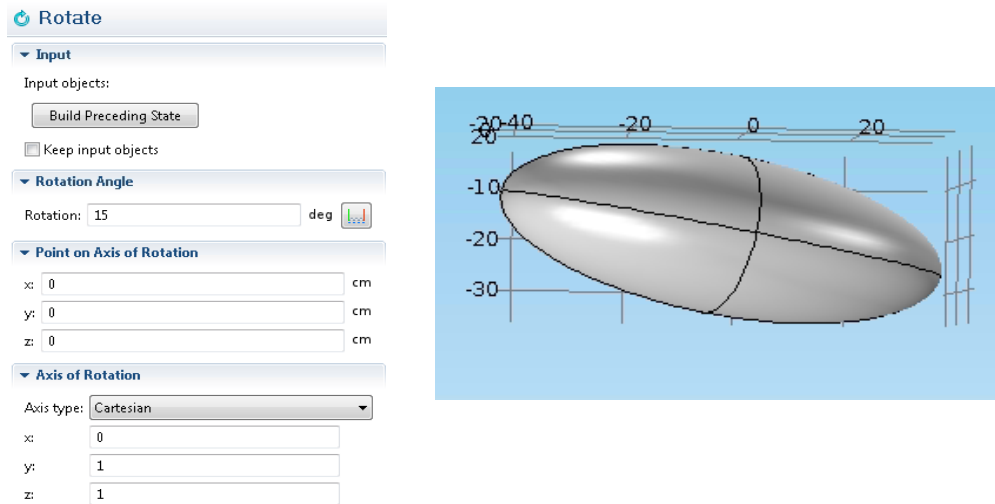


Figure B.31: Rotation setting and the built model

To build the smaller ellipsoid all the steps mentioned previously for building an ellipsoid has to be followed but the semi-axis dimensions for the new ellipsoid have to be entered as we add  $a = 25$  cm,  $b = 15$  cm,  $c = 8$  cm with x coordinate at 8 cm and z coordinate at -20 cm. The next step will be to navigate to geometry1 → transforms → rotate option to give a tilt to the ellipsoid

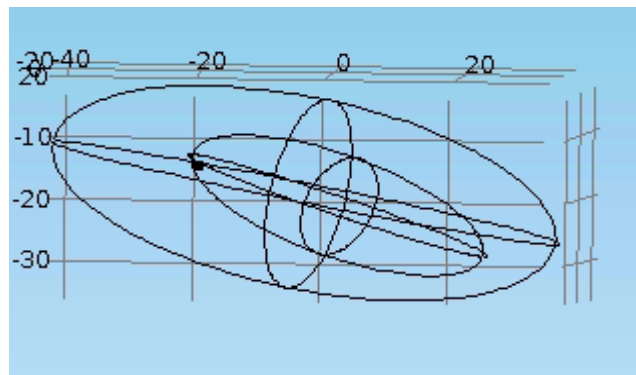


Figure B.32: Representation of double ellipsoids

(representing a torso in the bathtub). The input object should be selected as the ellipsoid, and a 15-degree tilt in y and z-direction has to be provided as shown in the Fig. B.31. The wire frame rendering option has to be enabled to see through solid objects of the model and obtain a view as shown in the Fig. B.32.

The next step will be to define the boundary for the ellipsoid by navigating to definitions → selections → Explicit and selecting the smaller ellipsoid as the input to the new ‘explicit 2’ condition. The next step would be to create two points inside the two ellipsoidal shape which will be used at a later stage to define the two point dipole to create 3D-CDs. To create a point, we

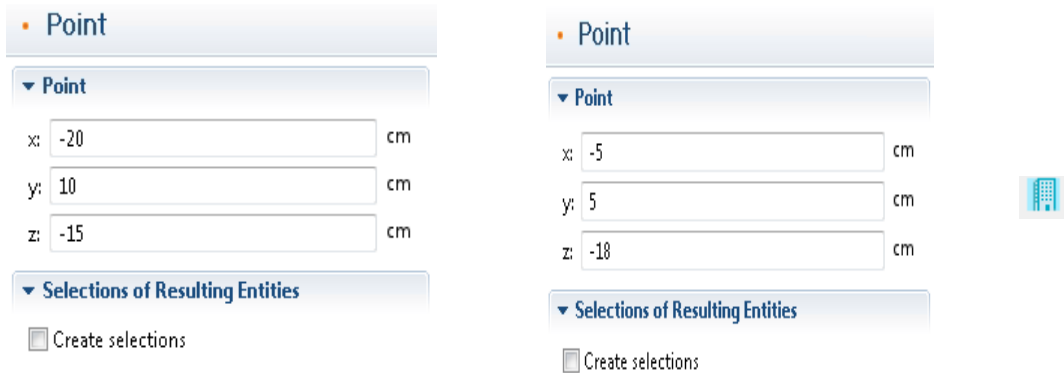


Figure B.33: Inputs for the eccentric points in the medium

navigate to geometry → more primitives and select the option of a point. The coordinates of the first point are  $x = -20$  cm,  $y = 10$  cm, and  $z = -15$  cm and for the second point the coordinates are  $x = -5$  cm,  $y = 5$  cm and  $z = -18$  cm and use the build all option to create the geometry as shown in Fig. B.34.

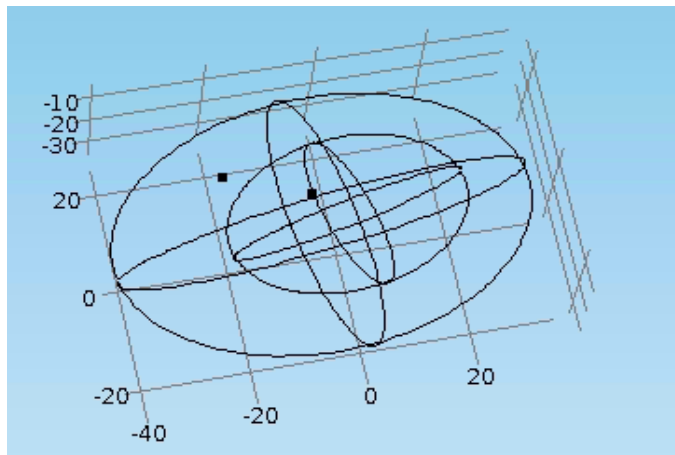


Figure B.34: Representation of double ellipsoidal phantom with eccentrically located points

To view the location of the point inside the ellipsoidal geometry, we use the wireframe rendering option in the graphics window.

The next step is to build a trapezoidal medium of dimensions 142 x 65 x 45 cm (width x breadth x height) which is done by navigating to geometry → more primitives → pyramid and providing the dimensions in the base length 1 x base length 2 x height respectively and the ratio of the corners has to be selected as 0.75.

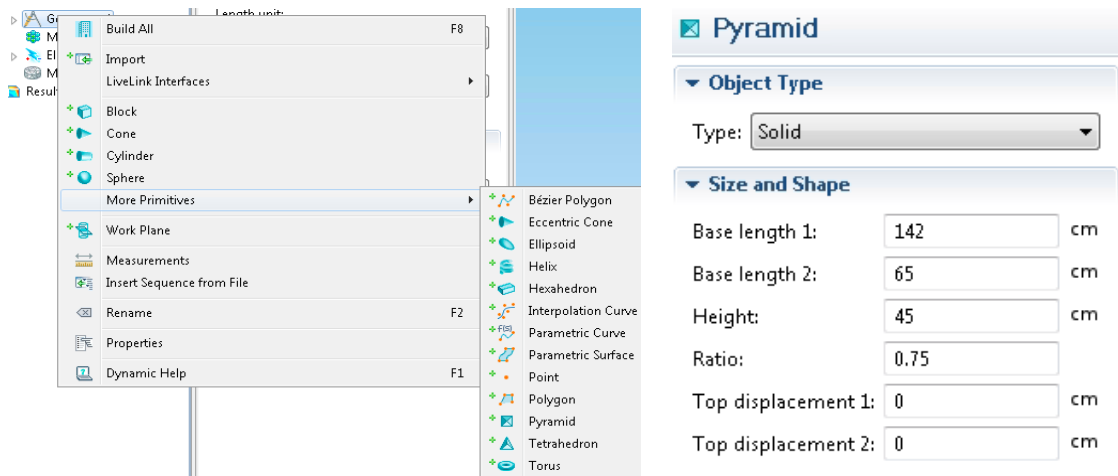


Figure B.35: Details of creating a trapezoidal medium

Once the build all option is selected an inverted trapezoidal medium is created, and we can use the rotate option by navigating to geometry → boolean → rotate. The next step is to choose



Figure B.36: Details depicting how to rotate the model built



the object and provide the rotation of 180 degrees in the y-axis. This will create the medium as shown in the Fig. B.37.

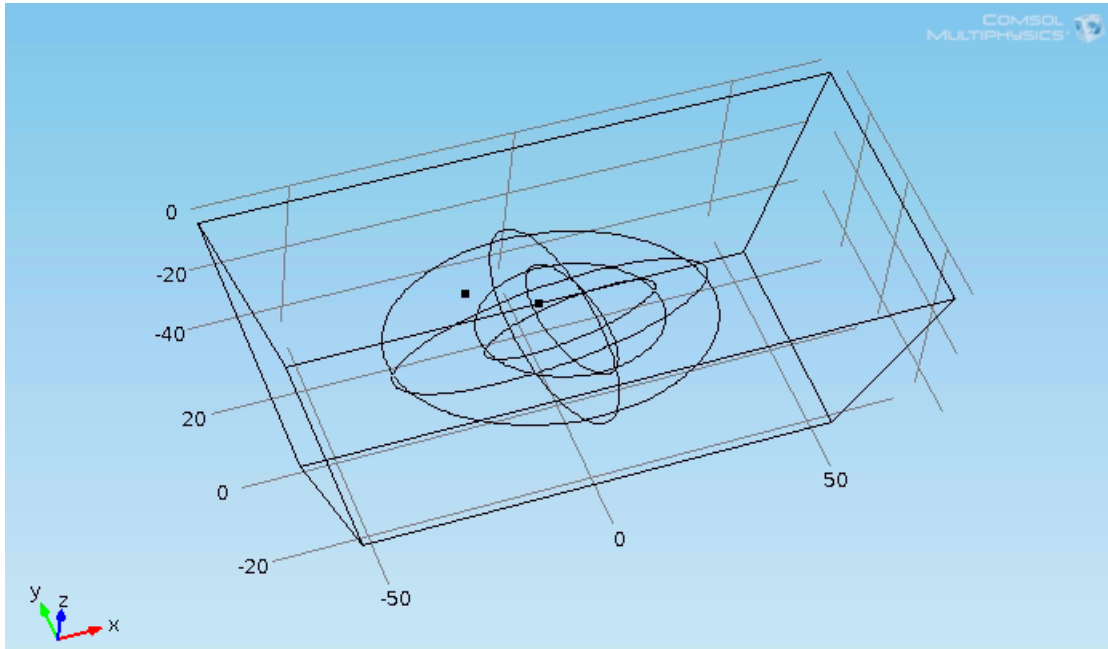


Figure B.37: Bathtub ellipsoid model

The next step will be to define the materials for the experiment. We have to navigate to materials and select add material option and set the ellipsoid with new material properties of 0.21 S/m conductivity and 0 permittivity. Similarly, add material to the smaller ellipsoid of conductivity 0.18 S/m and 0 permittivity. The next step would be to navigate to the materials option and select open material browser and choose liquid and gases and select the sub-option of water and finally choose the trapezoidal bathtub shaped structure with this material and change the permittivity to 0 and conductivity to 0.05 S/m.

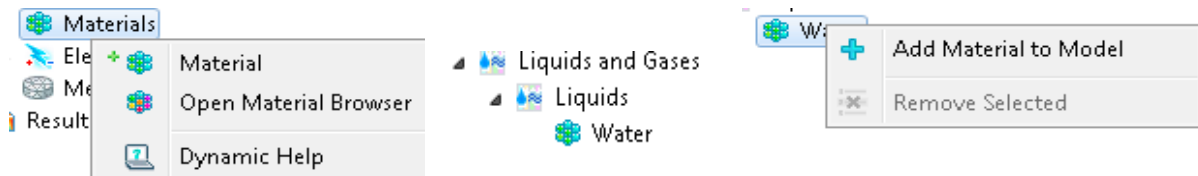


Figure B.38: Options for selection of materials

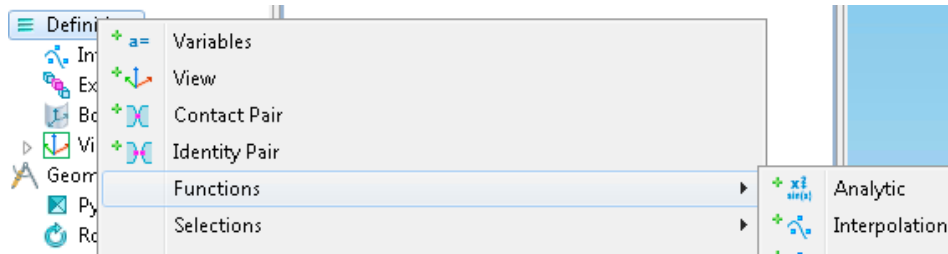


Figure B.39: Importing a basis signal from external file

The next step would be to import the basis signals by navigating to definitions → functions → interpolation and loading the respective basis signals files to the interpolation tab.

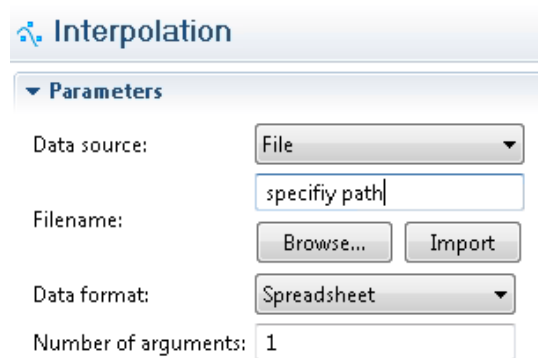


Figure B.40: Interpolation

Repeat the above-mentioned steps for importing all the basis signal files to the model. The next step will be to define the two electrical dipoles inside the ellipsoid to act as a 3D-CDs, by navigating to electric currents → points → electric point dipole.

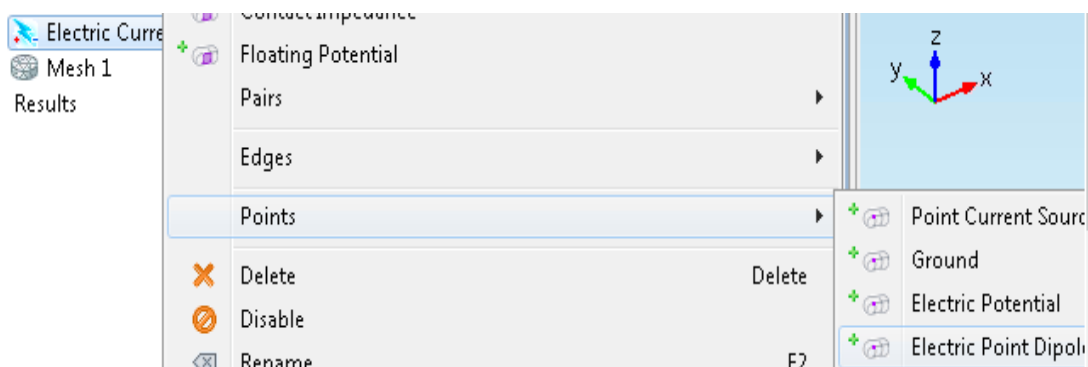


Figure B.41: Option to create a point electric dipole

The specific eccentrically located point inside the bigger ellipsoid has to be selected as the electric point dipole 1 and the eccentric point located inside the smaller ellipsoid to represent the electric dipole 2 and specify the tri-axial dipole moments in the form of time-varying functions as shown in the Fig. B.42.

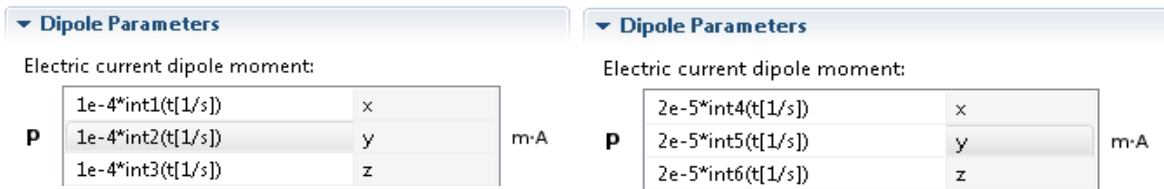


Figure B.42: Specification of the two vector dipoles located eccentrically inside each ellipsoid

The next step is to define 8 probes to monitor the time-varying potential distribution around the outer surface of the water medium. In order to define probes we have to navigate to definitions → domain point probe and select the appropriate coordinates where the probe has to be placed. 8 probes have to be placed on the surface of the bathtub as shown in Fig. 3.8 of chapter 3.

The settings in the time-dependent study sub-option has to be changed as shown in Fig. B.44. to reflect the sampling rate of the basis signals and finally the run simulation option in the

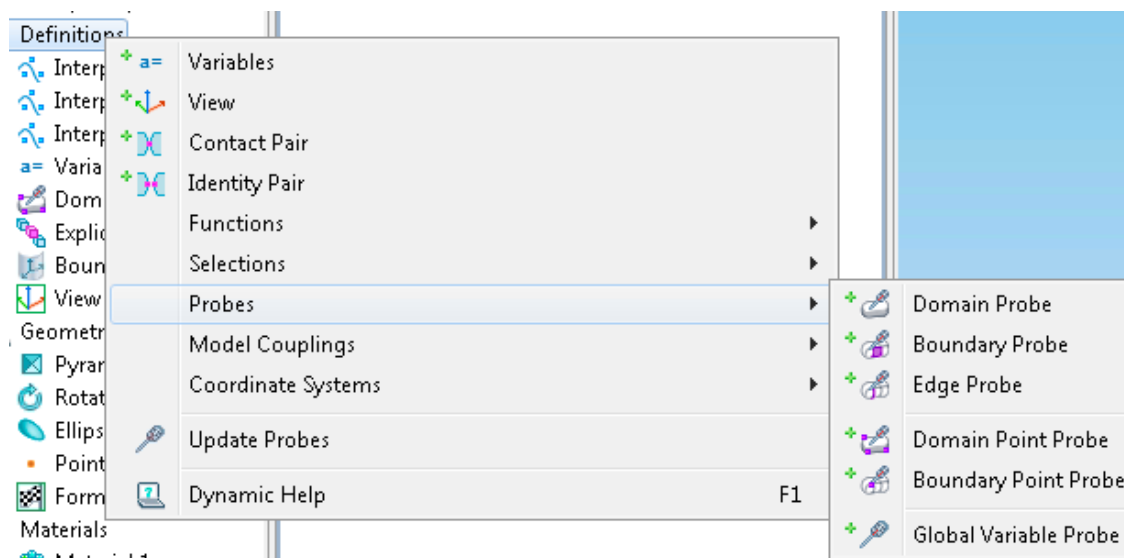


Figure B.43: Details on adding probes to the medium

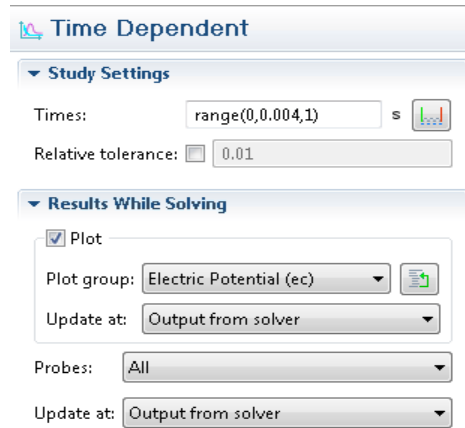


Figure B.44: Details to choose the type of study

study1 sub-option has to be selected, and potential distribution around the bathtub can be recorded for further analysis in MATLAB. For analyzing the single ellipsoid case, we have to disable the smaller ellipsoid and its respective 3D-CD to perform the single ellipsoidal analysis.

### B.7. Proposed Experimental Setup Assembly

The ellipsoidal phantoms were designed in solid works and 3D-printed using special conductive PLA of volume resistivity 128 Ohms per cm. The 3D drawing of the final proposed

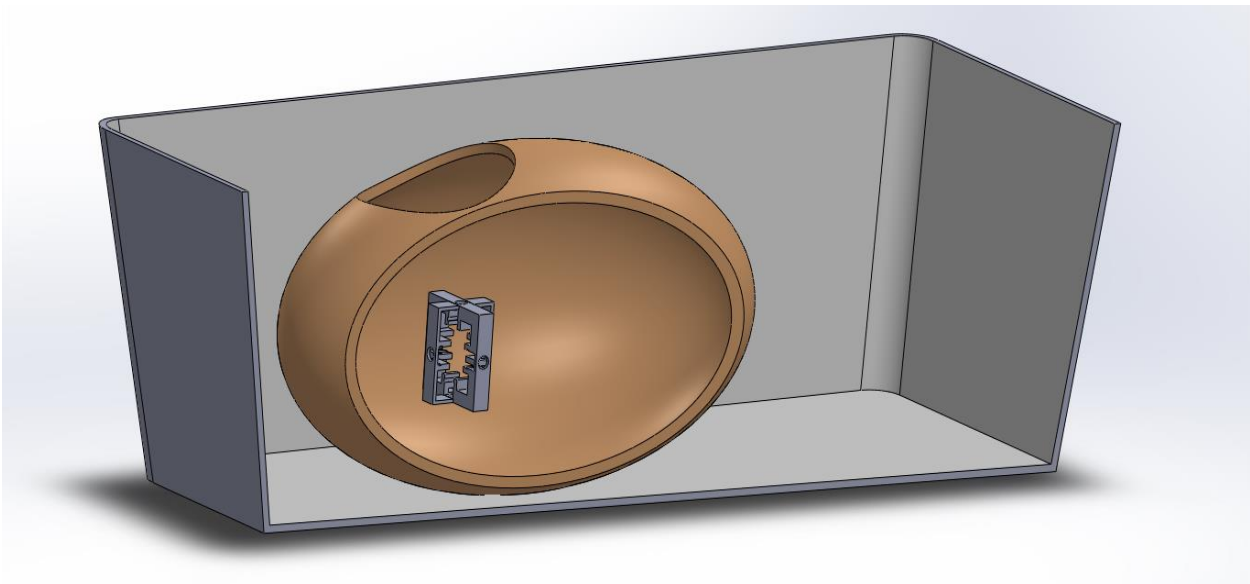


Figure B.45: Assembly of the ellipsoid and 3D-CD in the plastic container model

assembly for the ellipsoidal phantom inside a plastic container consisting of a 3D-CD is shown in Fig. B.45.

### **B.7.1. Structure for Creating 3-Dimensional Dipole (3D-D)**

SolidWorks was used to create a mounting structure for the 3D dipole. The mounting structure has an overall dimension of 2.5 x 2.5 cm. The specification of the copper plates which act as monopoles is 0.5 x 0.5 cm. The 3D model of the mounting structure is shown in Fig. B.46.

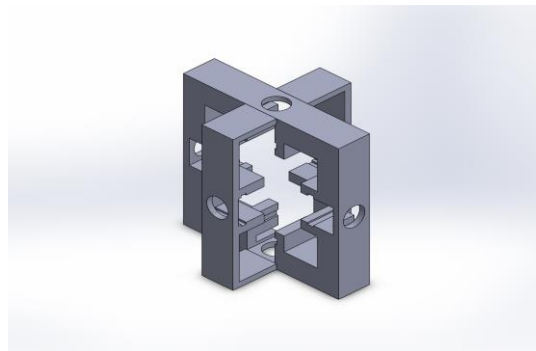


Figure B.46: Mounting structure for the 3D-D built using 6 copper plates in orthogonal directions

## **APPENDIX C: PRELIMINARY EXPERIMENTS ON 3D-MONOPOLE**

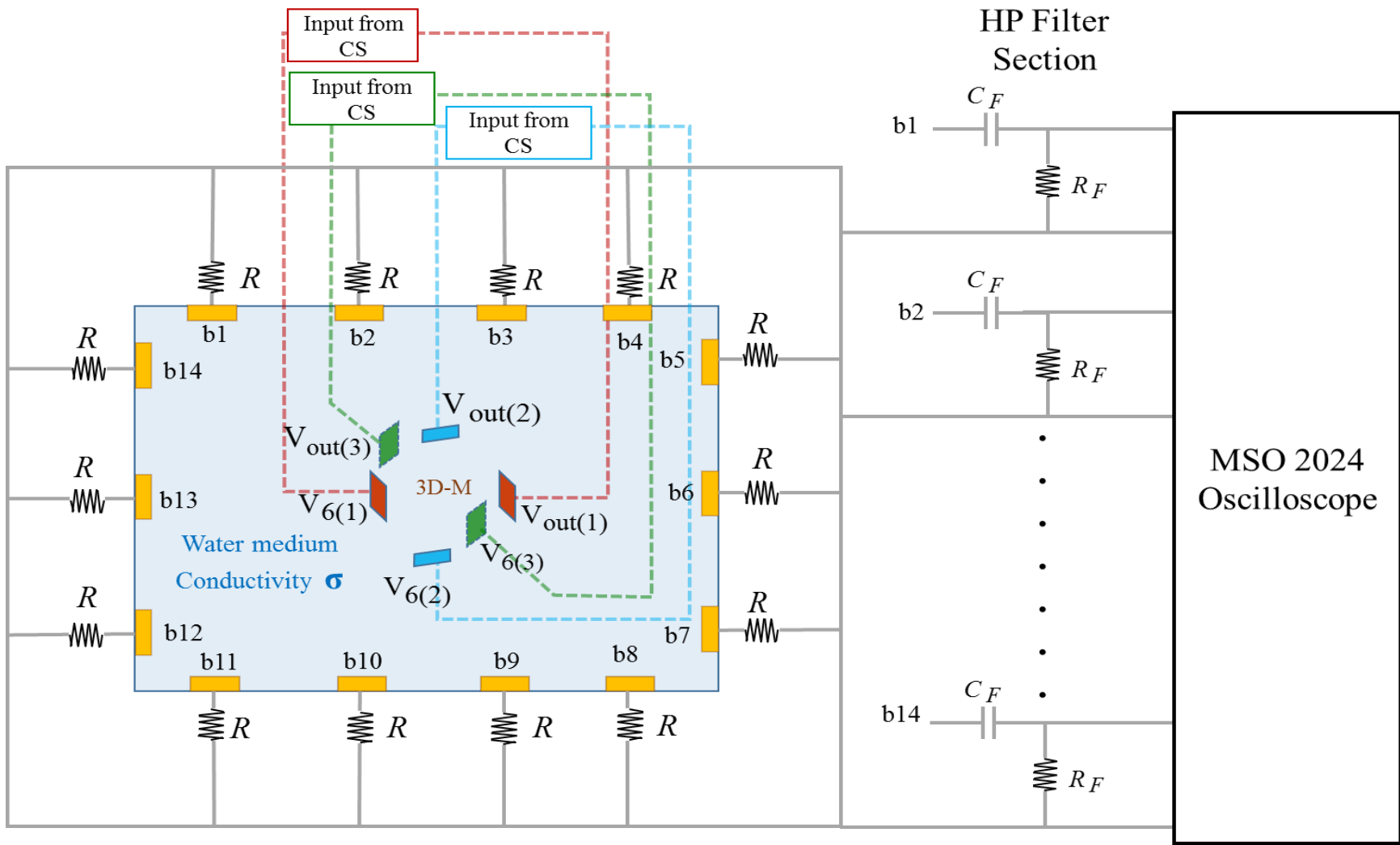
This section gives details on the experimental setup, and the result obtained due to the unequal current monopole excitations. The reason for concentrating on monopoles is that we could not realize in circuit form synthetic current dipoles.

### **C.1. System Setup**

The setup shown in Fig. C.1 is a simplistic view of the actual model where more than one row of electrodes are attached for the purpose of sensing the potential distribution around the plastic container. The free end of the sensing probes is connected via 100 k ohm resistor to form the neutral point. As observed that the time constant for the waveforms used in the system setup was in the range of 0.1, the cut-off frequency was designed at 1.59 Hz. A high pass filter was employed and the value of the resistor and the capacitor were chosen appropriately as 100  $\mu$ F and 1k ohms respectively. A tektronix MSO 2024 oscilloscope is used to measure the potential distribution across the plastic container.

#### **C.1.1. Noise and Bias Effects Reduction**

The low-frequency range of 40 to 100 Hz is of interest in the experiments related to ECG measurements, the problem which negatively impacted the experimental setup were 60 Hz interference and DC level shift. This research employs simple solutions for these problems without the use of greater complexity circuits which would further impact on the already distorted results. Therefore, bandwidth limiting noise filtering feature available in the oscilloscope was used to filter the distortions created by the 60 Hz interference.



$R = 100 \text{ k}\Omega$   
 $C_F = 100 \text{ }\mu\text{F}$   
 $R_F = 1 \text{ k}\Omega$

Figure C.1: System setup

The problem related to DC shifts was eliminated using a High pass filter of cut off frequency in the range of 1.59 Hz.

### C.2. Transferring an fECG or mECG File to BK Function Generator

The basis signals are extracted from the ECG data downloaded from physionet [39]. The basis files stored in '.csv' format are then transferred from the wavexpress software installed on a computer to the BK using RS232 file transfer option as summarized in Fig. C.2.

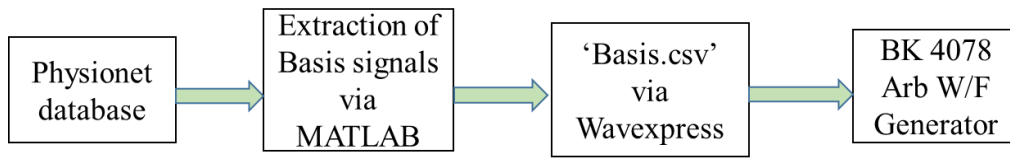


Figure C.2: Block diagram of fECG or mECG file transfer from PC to BK

### C.3. Singular Excitation of Current Monopoles to Create a Balanced Effect

Voltage controlled current sources are used to excite the monopoles in Fig. C.2. The BK supplies mIECG through the current sources to the 3D-Monopoles (3D-M) which are setup in the plastic container. The potential distributions around the plastic container are measured and recorded using an oscilloscope in Fig. C.1. The individual monopole pair in every axis is excited, one pair at a time, and the corresponding potential distribution around the container is recorded.

If  $x(t)$ ,  $y(t)$ , and  $z(t)$  are the individual monopole excitations then the potential distributions  $V_{x,i}(t)$ ,  $V_{y,i}(t)$ , and  $V_{z,i}(t)$  are recorded, where the first subscript ( $x$ ,  $y$ , or  $z$ ) corresponds to individual monopole excitation and the second subscript represents the probe index. (A.2), (A.4), and (A.6) correspond to the probe voltages after the mean has been subtracted and it is plotted in Fig. C.5 to C.7.

$$\bar{V}_x(t) = \frac{1}{M} \sum_i^M V_{x,i}(t) \quad (\text{A.1})$$

$$\tilde{V}_{x,i}(t) = V_{x,i}(t) - \bar{V}_x(t) \quad (\text{A.2})$$



$$\bar{V}_y(t) = \frac{1}{M} \sum_i^M V_{y,i}(t) \quad (\text{A.3})$$

$$\tilde{V}_{y,i}(t) = V_{y,i}(t) - \bar{V}_y(t) \quad (\text{A.4})$$

and

$$\bar{V}_z(t) = \frac{1}{M} \sum_i^M V_{z,i}(t) \quad (\text{A.5})$$

$$\tilde{V}_{z,i}(t) = V_{z,i}(t) - \bar{V}_z(t) \quad (\text{A.6})$$

where M accounts for the number of probes actually used for sensing. Even though there were 20 probes placed on the plastic container, M=4 were actually used in this research. Since the excitation is via a single monopole, in a pair, the mean has to be subtracted out of all the recorded distributions to create balanced monopole distributions around the plastic container. Thus, even though 3D monopoles are shown, the results in Fig. C.5 to C.7 are for 1-D monopole experimentation.

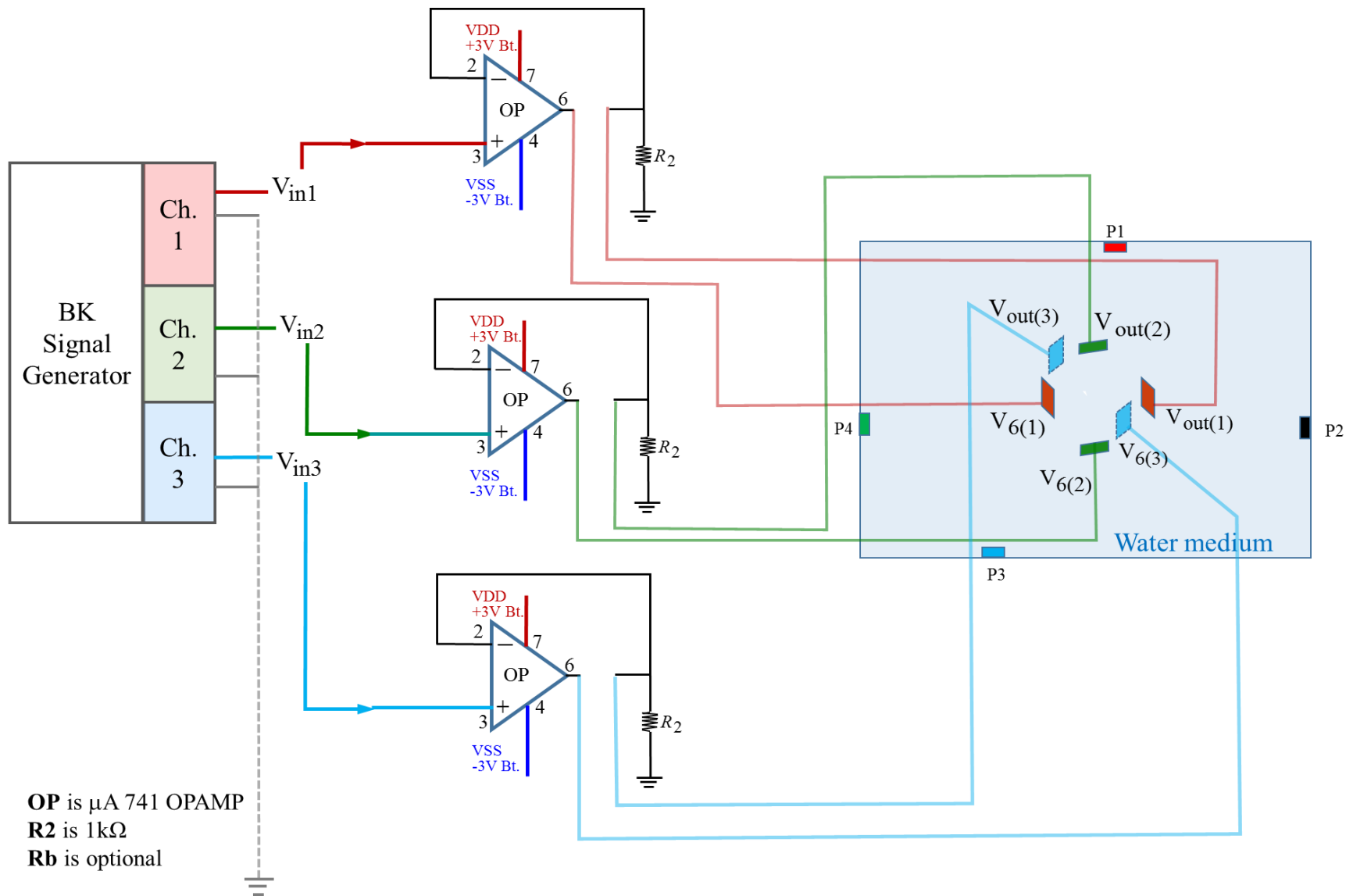


Figure C.3: Experiment of 3D-M using singular excitations

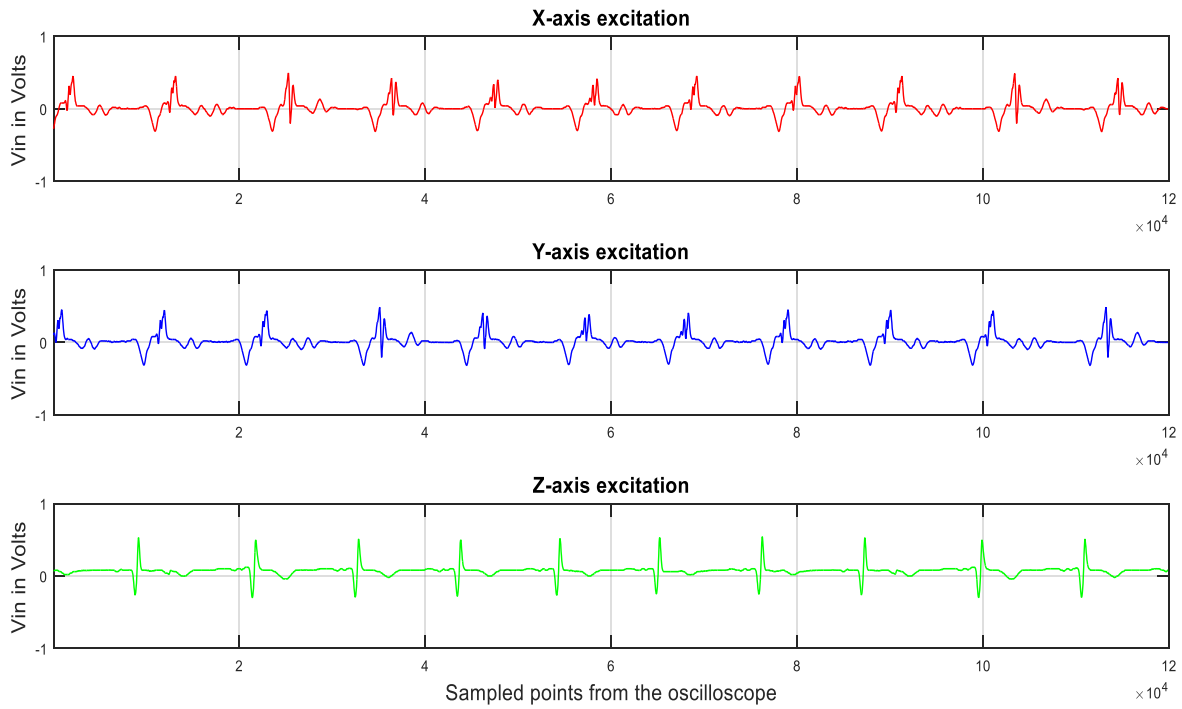


Figure C.4: Inputs to the 3-axis monopoles

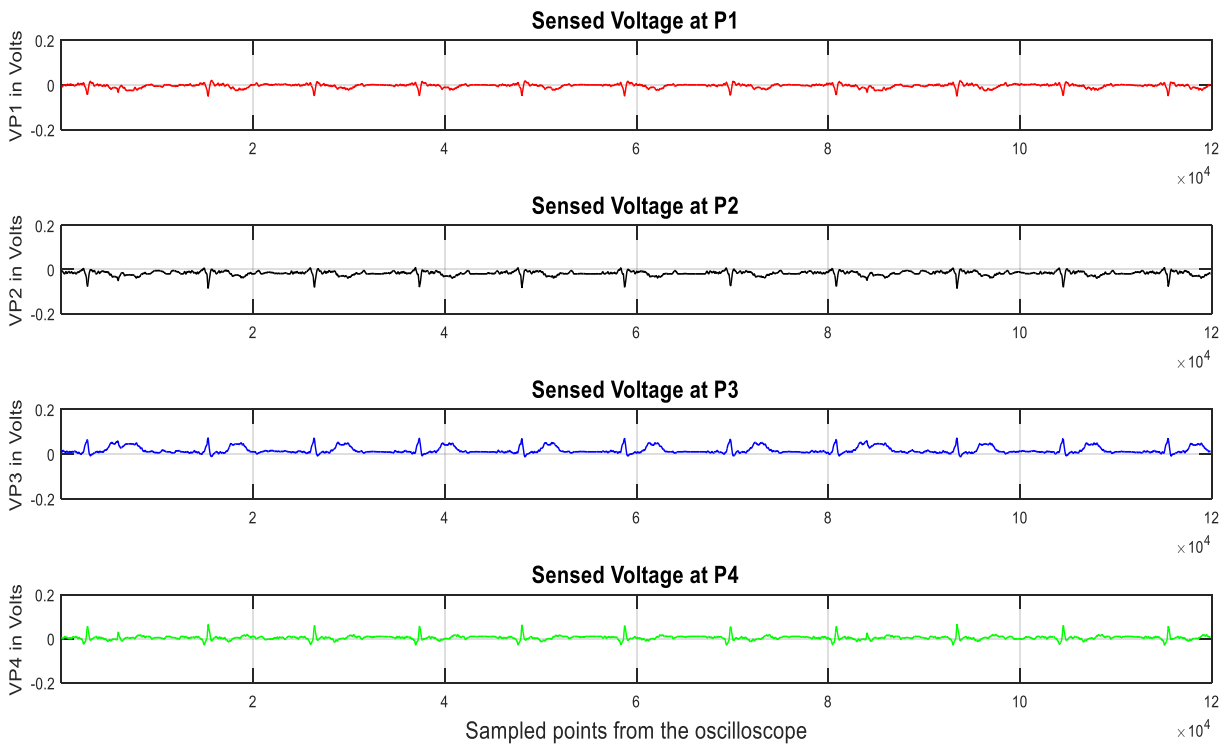


Figure C.5: Potential distribution recorded at the probes with mean subtracted when X-axis monopole is active

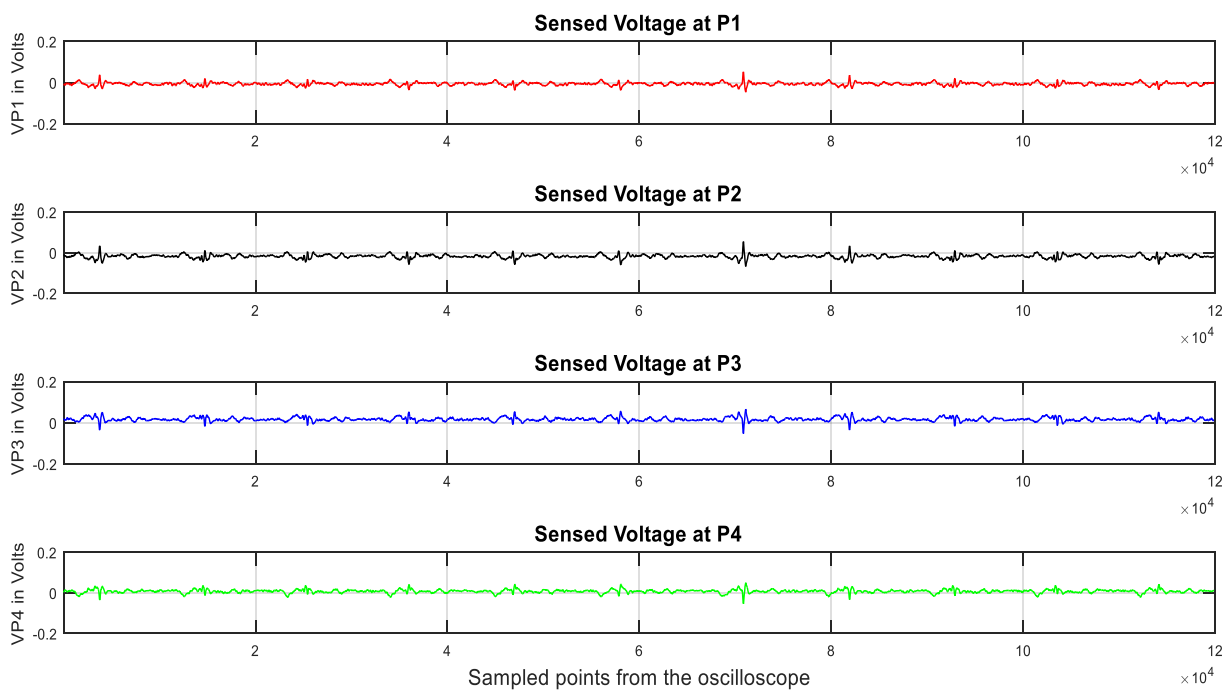


Figure C.6: Potential distribution recorded at the probes with mean subtracted when Y-axis monopole is active

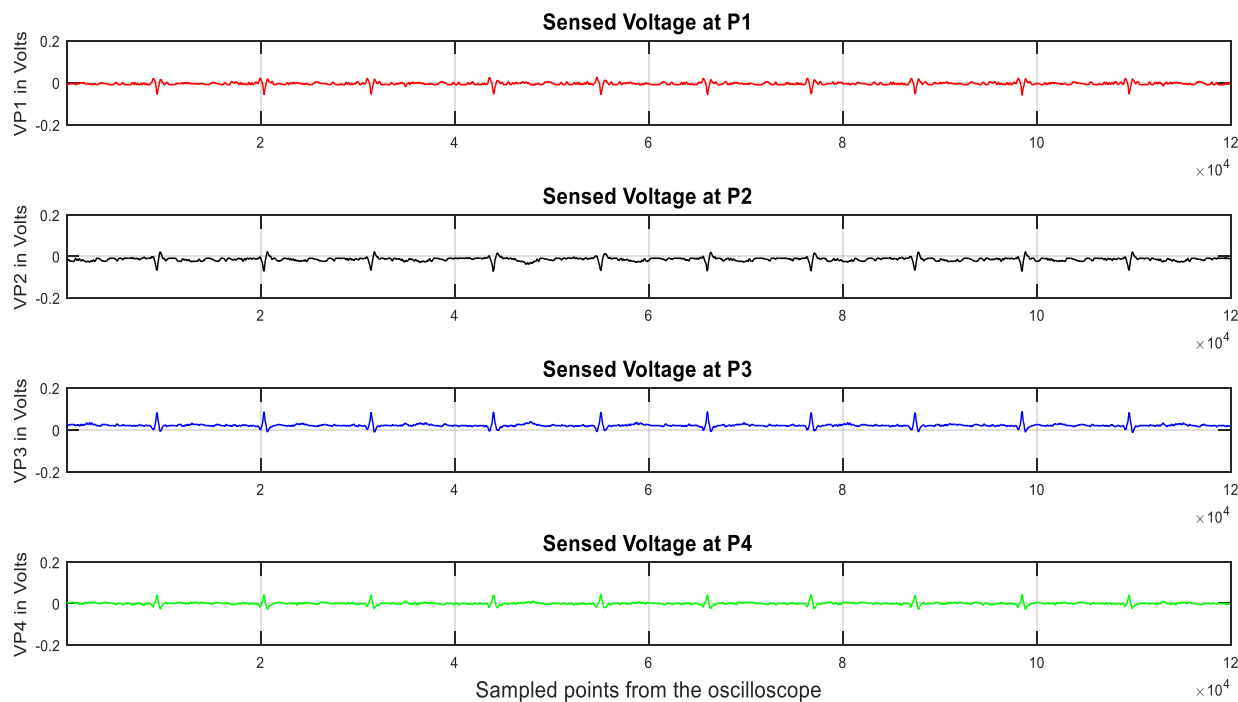


Figure C.7: Potential distribution recorded at the probes with mean subtracted when Z-axis monopole is active